Modeling of Fluids and Waves with Analytics and Numerics

by

Xiangdong Liang

Submitted to the Department of Mathematics

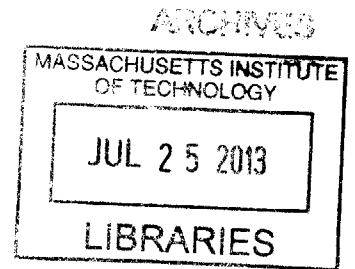in partial fulfillment of the requirements for the degree of

Doctor of Philosophy

at the

MASSACHUSETTS INSTITUTE OF TECHNOLOGY

February 2013

Author . . . .
Department of Mathematics
January 14, 2013

Certified by . . . .
Steven G. Johnson
Associate Professor of Applied Mathematics
Thesis Supervisor

Accepted by . . . .
Michel Goemans
Chairman, Department Committee on Graduate Theses

Modeling of Fluids and Waves with Analytics and Numerics

by

Xiangdong Liang

Abstract

Capillary instability (Plateau-Rayleigh instability) has been playing an important role in experimental work such as multimaterial fiber drawing and multilayer particle fabrication. Motivated by complex multi-fluid geometries currently being explored in these applications, we theoretically and computationally studied capillary instabilities in concentric cylindrical flows of N fluids with arbitrary viscosities, thicknesses, densities, and surface tensions in both the Stokes regime and for the full Navier-Stokes problem. The resulting mathematical model, based on linear-stability analysis, can quickly predict the breakup lengthscale and timescale of concentric cylindrical fluids, and provides useful guidance for material selections and design parameters in fiber-drawing experiments. A three-fluid system with competing breakup processes at very different length scales is demonstrated with a full Stokes flow simulation.

In the second half of this thesis, we study large-scale PDE-constrained microcavity topology optimization. Applications such as lasers and nonlinear devices require optical microcavities with long lifetimes Q and small modal volumes V. While most microcavities are designed mostly by hand using some understanding of the physical principles of the confinement, we let the computer discover its own structures. We formulate and solve a full 3d optimization scheme over all possible 2d-lithography patterns in a thin dielectric film. The key to our formulation is a frequency-averaged local density of states (LDOS), where the frequency averaging corresponds to the desired bandwidth, evaluated by a novel technique: solving a single electromagnetic wave scattering problem at a complex frequency.

Thesis Supervisor: Steven G. Johnson
Title: Associate Professor of Applied Mathematics

Acknowledgments

First of all, I want to thank my thesis advisor Prof. Steven G. Johnson. I am deeply indebted to Prof. Johnson for his advice, support, and encouragement. Thanks for spending an enormous amount of time with me over the past few years, talking about mathematics, physics and computation, teaching me how to make good presentations as well as debugging my numerical codes. I am very grateful and fortunate to have Prof. Johnson as my advisor.

I would like to thank my thesis committee: Prof. John Joannopoulos and Prof. Martin Bazant. Thanks for their time, effort, and helpful feedback.

I would also like to thank my collaborators: Prof. J-C Nave (McGill University), Dr. Daosheng Deng, Prof. Ayman Abouraddy (UCF), Prof. Yoel Fink. I really enjoyed the collaboration with them. I also thank Dr. Yang Zhang and Dr. Peter Buchak (U Mass) for their kind help on numerical simulations.

Being one of the cluster administrators in the ab-initio physics research group, I learned many Linux-cluster management skills from Dr. Peter Bermel, Dr. Ardavan Oskooi, Dr. Wenjun Qiu, and Dave Foss from RLE.

I thank all the members of SGJ and JDJ groups, in particular, Dr. Song Liang Chua, Dr. Hila Hashemi, Wade Chia Wei Hsu, Ognjen Ilic, Dr. Karen Lee, David Liu, Dr. Ling Lu, Dr. Alexander McCauley, Dr. Owen Miller, Dr. Homer Reid, Dr. Alejandro Rodriguez, Yichen Shen, Bo Zhen. Thanks for their kind help and valuable discussions.

Additionally, I would like to thank Prof. Roderick Wong and Prof. Ya Yan Lu at City University of Hong Kong. Studying at Hong Kong was a turning point in my life. Thanks for their generous help and advice during and beyond my study in CityU.

My Ph.D. journey would have been less enjoyable and much harder without my family's continuous support. I would like to thank my parents and my wife Lu Bai. Thanks for their unconditional love and constant support for my endeavors.

Contents

List of Figures

11

13

15

List of Tables

Chapter 1

Introduction

A JOURNEY WITH EPSILON

Small Quantity	Boundary Layer	Machine Precision	Dielectric Permittivity
Asymptotic Analysis	Fluid Mechanics	High Performance Computing	Electromagnetism

Mathematical Modelling | *Computational Fluid Dynamics* | *Computational Electrodynamics*

This thesis is a journey of epsilon (ε). In mathematics, epsilon may represent a small quantity, as the one in the ε–δ definition of limits from freshman mathematical analysis. By identifying different orders of small quantities (e.g., $\varepsilon, \varepsilon^2, \varepsilon^3, \cdots$), we can use asymptotic analysis to analyze problems. By dropping smaller terms, we can simplify real problems and build mathematically solvable models. In computation, epsilon may represent the machine precision, a tiny number giving the upper bound of the relative round-off errors (the relative difference between the computer approximation of a number and its exact mathematical value). To let the computer help us solve equations correctly and efficiently, we have to understand this epsilon well. In physics, epsilon may represent the dielectric permittivity (the square of refractive index) in electromagnetism and the thickness of the boundary layer in fluid mechanics. In applied mathematics, it seems that everything is connected by epsilon, such as mathematical modeling, computational fluid mechanics, and computational electromagnetism.

In the first half of this thesis (chapters 2–3), we use epsilon for analytical and numerical tools to study the instability phenomena due to surface tension in concentric cylindrical flows. In the second half (chapters 4–5), we design a structure by arranging different materials (namely, different dielectric constants ε) to trap light for a long time in a small volume.

1.1 Capillary instability

Chapters 2–3 of this thesis attack the problem of capillary instability in concentric multi-fluid systems. Capillary instability, also known as the Plateau-Rayleigh instability, is the instability induced by surface tension, which causes fluid cylinders to break up into droplets in order to reduce their surface area [36, 37, 68]. Figure 1-1 illustrates the breakup of a water jet due to surface tension at three different wavelengths [106]. Because the breakup point in the bottom picture is closer to the nozzle (on the left) than in the top two pictures, it implies that the perturbations with that wavelength grow much faster than at the other wavelengths. [36].

Plateau [97] first recognized the important role of surface tension in this breakup process [39]. Plateau used simple geometrical arguments based on comparing surface energies (surface areas) before and after small perturbations to show that, whenever a cylindrical jet's length exceeds its circumference, it is always unstable due to surface tension.

However, Plateau did not obtain the *most* unstable wavelength among all the unstable ones. The *most* unstable mode and its growth rate were obtained by Lord Rayleigh, who first introduced the powerful tool of linear stability analysis [33] and reconsidered inviscid water jets [101] and viscous liquid jets [102]. However, Lord Rayleigh only considered a *single* fluid jet in air. By considering the effect of the surrounding fluid, Ref. [117] generalized this analysis to a cylindrical viscous liquid surrounded by another viscous fluid.

All these analysis were for one- or two- fluid systems. However, current experimental research is looking at increasingly complicated fluid systems involving three
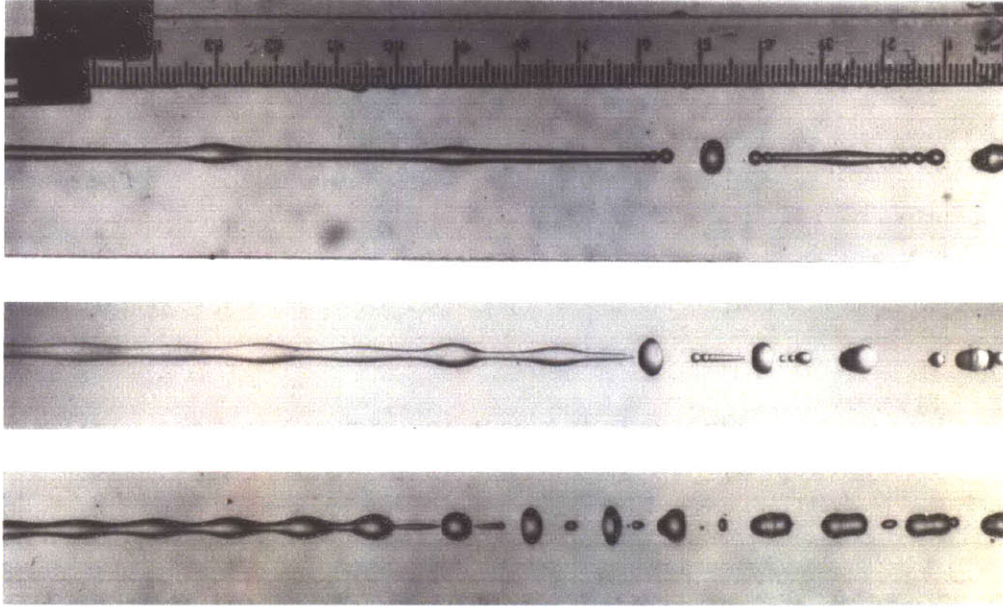
Figure 1-1: The breakup of a water jet at different wavelengths excited by a loud-speaker [120]. It illustrates that perturbations with different wavelengths grow at different rates, inferred from the distance between the breakup point and the nozzle at the left end. (Van Dyke, An Album of Fluid Motion, 1982, figure 122.)

or more fluid layers (of two or more fluids). For example, Ref. [119] recently demonstrated the fabrication of double emulsions (droplets within droplets) by exploring instabilities in three-fluid system (figure 1-2a). Because the available theory was limited to equal viscosities [112], the experimental researchers chose only fluids in that regime.

The capillary instability analysis for multi-fluid analysis in this thesis was motivated by complex multi-fluid geometries currently being explored in fiber-device manufacturing. In fiber drawing (figure 1-2b), a scale model (preform) of the desired device is heated to a viscous state and then pulled (drawn) to yield a long fiber with (ordinarily) identical cross-section but much smaller diameter. For example, concentric layers of different polymers and glasses can be drawn into a long fiber with submicron-scale layers that act as optical devices for wavelengths on the same scale as the layer thicknesses [1]. Other devices, such as photodetectors [110], semiconductor filaments [29, 30], and piezoelectric pressure sensors [40] have similarly been incorporated into microstructured fiber devices. That work motivates greater theoretical

investigation of multi-fluid geometries, and in particular the stability (or instability time scale) of different geometries is critical in order to predict whether they can be fabricated successfully.

(a) Double emulsions generated from a microcapillary device [119].

(b) Multiple-material fiber-drawing [1].
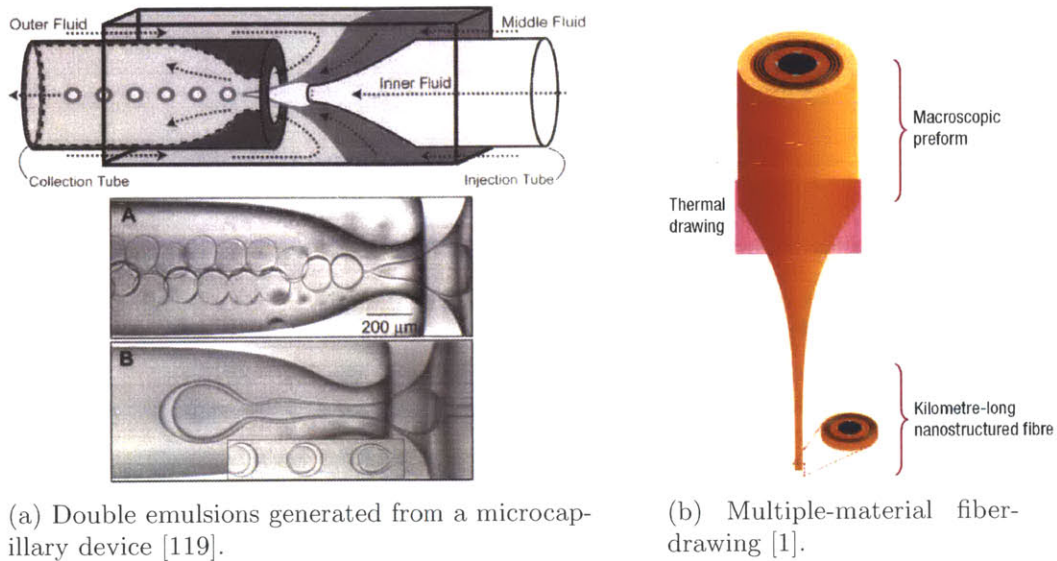
Figure 1-2: Capillary instability in multiple-fluid devices. Figure (a) demonstrates the fabrication of double emulsions (droplets within droplets) by exploring instabilities in three equal-viscosity fluids system [119]. Figure (b) sketches the fiber-drawing process: a preform of the desired device is heated to a viscous state and then pulled to yield a long fiber with identical cross-section but much smaller diameter [1].

In fiber drawing, one wants to keep the long drawn fiber intact instead of disintegrating. Therefore, the drawing time should be much smaller than the typical breakup time. In contrast, breakup is desired in particle fabrication. Reference [58] harnesses the inherent scalability of fiber production and in-fiber capillary instability for the fabrication of uniformly sized, structured spherical particles (figure 3-1).

In all of these applications, it is critical to understand the possible instabilities and the lengthscales and timescales of the growth modes, and have a quick way to explore different material parameters in order to design new devices and phenomena. Unfortunately, not much theoretical and computational work on capillary instability in multiple-fluid system had been done. Reference [112] analyzed the three-fluid ($N = 3$) Stokes cylinder problem, but only for equal viscosities. Reference [19] analyzed the $N = 3$ case where the inner two fluids have arbitrary viscosities and the

outermost fluid is inviscid gas, taking into account the full Navier–Stokes equations.

The goal of this part of my thesis, in chapters 2–3, is to fully generalize the analysis: study capillary instabilities in concentric cylindrical flows of N fluids with arbitrary viscosities, thicknesses, densities, and surface tensions in both the Stokes regime and for the full Navier–Stokes problem. The results of our linear stability analysis is a small semi-analytical expression for the growth modes and growth rates in terms of a small matrix problem. We check analytically that it reduces to the previous results for $N = 2$ and $N = 3$ cases. We also validate the analysis with full three-dimensional numerical simulations. Semi-analytical methods and large-scale Stokes flow simulations are complementary in studying capillary instabilities, since the former allow rapid exploration of wide parameter regimes (e.g. for materials design) as well as rigorous asymptotic results, while the latter can capture the culmination of the breakup process as it grows beyond the linear regime.

Almost no systems with three or more fluids have been analyzed before, so there are lots of possibilities to be explored. For a three fluid system with extremely thin shell (section 2.6.2), we show a connection to the classic single-cylinder and flat-plane results, consistent with a similar result for air-clad two-fluid jets [19]. In another three-fluid system, we exhibit an interesting case in which two growth modes at different wavelengths have the same effective growth rate, leading to competing breakup processes that we demonstrate with full 3-dimensional Stokes-flow simulations (section 2.7). We also consider some many-layer cases, including a limiting situation of a continuously varying viscosity (section 2.9).

The theoretical and computational tools we developed in this thesis are readily applicable to explain various experimental phenomena. For example, an interesting azimuthal (instead of typical axial) breakup process was observed experimentally [29] and has yet to be explained [28]; however, we show (section 2.2) that azimuthal instability does not arise in purely cylindrical geometries and must stem from the rapid taper of the fiber radius from centimeters to millimeters (the drawn-down "neck"), or some other physical influence (e.g., elastic effects, thermal gradients, or long-range van der Waals interactions). As a preliminary step, we study this problem as 2d

thin-film instability under the influences of surface tension and van der Waals forces in section 2.12. In chapter 3, we show its applications to multiple-layer particle fabrication, providing guidance on geometry parameters and material selections in experiments, as well as predicting the size of experimentally fabricated particles.

1.2 Micro-cavity optimization

Chapters 4–5 of this thesis are concerned with large-scale optimization of microcavities. What is a microcavity? A microcavity is an arrangement of materials (with different dielectric constants ε) that traps light for a long time in a small volume. A few examples of real fabricated cavities in silicon are shown in figure 1-3.
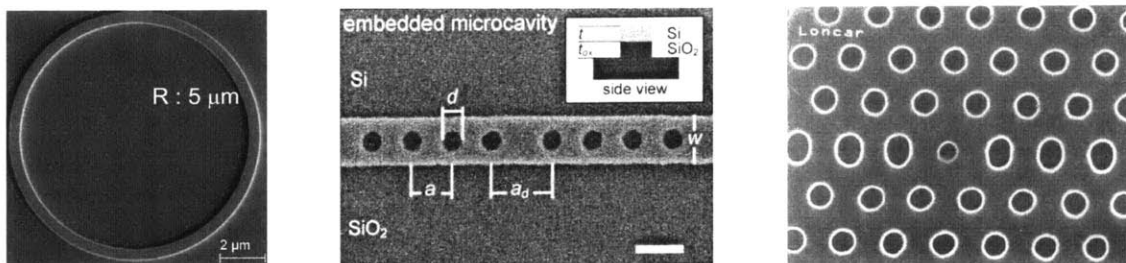
(a) Ring resonator [69].   (b) Cavity from 1d PhC [128].   (c) Cavity from 2d PhC [126].

Figure 1-3: Examples of real fabricated silicon cavities. (a) A simple ring resonator (a waveguide bent into a circle). (b) A fabricated microcavity formed by the introduction of a point defect (adding dielectric materials between two holes) into a periodic array of holes in the silicon waveguide [128]. (c) A fabricated microcavity formed by changing the radii of defect holes in 2d photonic crystals [126].

The simplest example is a ring resonator (figure 1-3a) [100]: just a waveguide bent into a circle. Whenever you bend the waveguide, light escapes into radiation, and the more tightly you bend it the faster the light escapes. There are two key figures of merit for a microcavity, Q and V. The quality factor Q, which is a dimensionless lifetime, is the number of optical periods that elapse before the energy decays by $e^{-2\pi}$, and $1/Q$ is a dimensionless decay rate. The mode volume V is simply a measurement of how big the mode is [a more precise definition is given in (4.3)]. The ring resonator example illustrates a common tradeoff[1] between the quality factor Q (which grows

---

[1]There are counter examples to this tradeoff, cavities with complete photonic bandgap [54] and

exponentially with the radius in this structure) and mode volume V (proportional to the circumference) [78]. For most applications with light–matter interactions (such as lasers, sensors, and nonlinear frequency conversions), maximal lifetime Q and minimal mode volume V are desirable.

Recently, people have looked at a wide variety of complicated patterns (figures 1-3b and 1-3c) to improve this Q versus V trade-off [4, 126, 128]. It turns out that many of these designs are based on starting with a periodic structure, called a photonic crystal, and then introducing a defect into the periodicity that traps light using something called a photonic bandgap [54]. However, in this thesis, we will develop algorithms to let the computer to discover these kinds of structure, periodic or not, using large-scale optimization.

We are interested in designing cavities that can be fabricated by lithography. With lithography, one starts with a planar slab of some material, and then etches some two-dimensional pattern into this planar slab (figure 1-4). The design question is what 2d pattern we should etch to trap a mode for as long as possible and in a volume as small as possible.
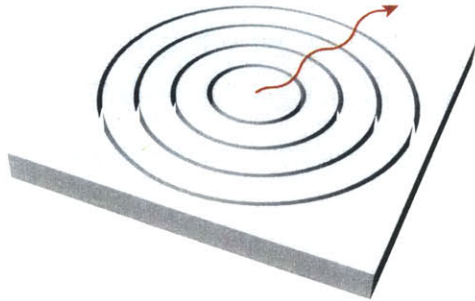
Figure 1-4: The sketch of a slab structure, which can be fabricated by lithography. The design question is what 2d pattern to etch so that it can trap a mode for as long as possible in a volume as small as possible.

To apply large-scale optimization, there are a few challenges we need to address. First, what precise optimization problem are we solving? It turns out extra care is needed to be well-posed. Once we formulate the problem, is it practical to apply

cavities with a special choice of dielectric constants [127], but neither can be realized in 3d with a single 2d lithography step.

large-scale topology optimization? We will show that choosing the right problem is the key to enable efficient algorithms. Given that cavities in silicon slabs have been heavily studied for more than 20 years [50, 54, 73, 87], can we obtain better results than these hand designs?

1.2.1 Previous work

Let me briefly review previous work on microcavity optimization. First of all, most cavities are designed "by hand" using some understanding of the physical principles of the confinement [4, 125]. Given a hand design, many groups [5, 89] have applied small-scale optimization, where they optimize a few parameters, such as the positions of a few air holes, to improve the performance (figure 1-5). However, this method mainly optimizes Q for a given V, because slightly changes in the structure typically do not change V much.

More recently, a few authors have studied large-scale topology optimization, where the patterns are essentially completely determined by the computer. Reference [32] minimized V for the 2d Maxwell equations subject to Dirichlet boundary conditions and there was no radiation loss in the system. Reference [57] maximized in-plane Q by imposing the radiation boundary conditions. However, V is not in the objective function and only implicitly bounded by the size of the optimized region. We are interested in optimizing Q and V *together* somehow, and including out of plane losses in 3d.

To avoid the expensive calculation in 3d, Ref. [75] proposed a so-called 2.5 optimization: do a 2d calculation and use a simple heuristic approximation for out of plane losses. They minimized the mode volume V subject to the constraint that there is no heuristic loss. But zero radiation loss in 2d turns into finite loss in 3d due to the imperfect approximation for the loss. For example, the optimized structure (figure 1-6) they obtained with this 2.5d formulation has $Q = 8000$ and $V = 0.31(\lambda/n)^3$.

Reference [41] performed real 3d calculations with finite element solver to optimize the Q by altering the hole shapes in the defect photonic crystal cavity. Instead of

28

(a) Optimization on the position of one hole in L_3 cavity [5]. Q=50000 and $V = 0.7(\lambda/n)^3$.
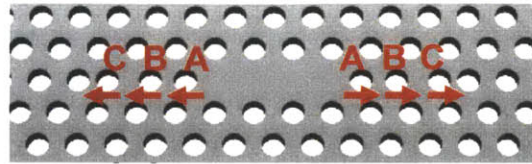
(b) Optimization on the positions of three holes in L_3 cavity [5]. Q=100000 and $V = 0.7(\lambda/n)^3$.
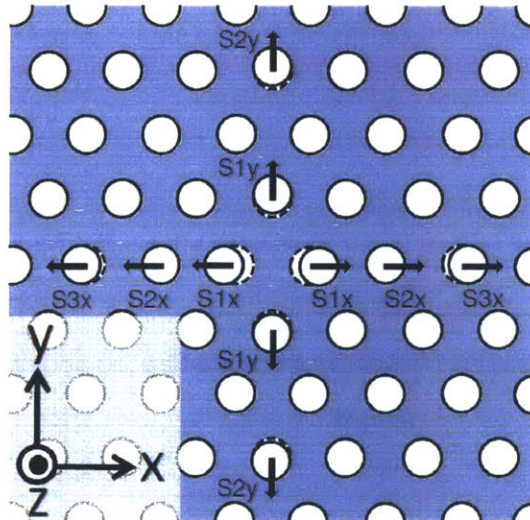
(c) Optimization on the positions of five holes in H_0 cavity [89]. Q=280000 and $V = 0.23(\lambda/n)^3$.

Figure 1-5: Small-scale microcavity optimization on the positions of a few air holes in L_3 and H_0 cavities.
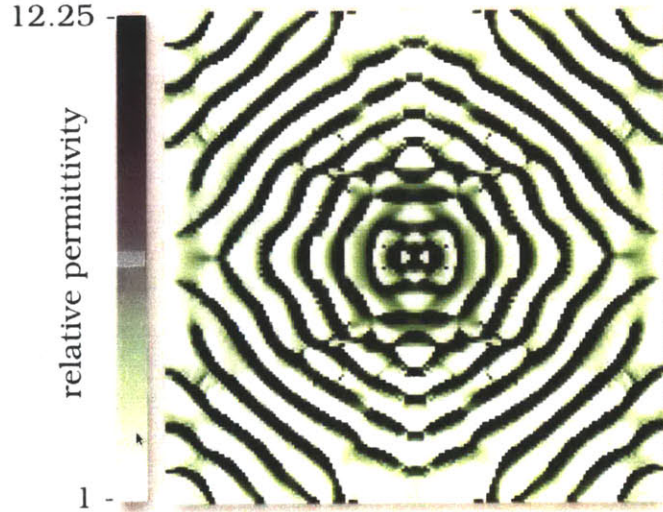
Figure 1-6: The structure obtained by large-scale 2.5d optimization ($Q = 8000$ and $V = 0.31(\lambda/n)^3$) [75]. The idea is to do a 2d calculation and use a simple heuristic approximation for out of plane losses.

solving for a mode or Q, they minimized the outgoing power of a line current near the center, taking the worst values at three frequencies. We will use similar ideas of solving a scattering problem rather than an eigenproblem, and of looking at a finite bandwidth. However, we believe that there are some fundamental changes that are required in their figure of merit. First, their work included an unphysical absorbing material within the cavity itself, leading to a heuristic objective whose calculation does not appear to have a rigorous quantitative relationship to relevant cavity properties. Second, even if the unphysical absorbing material is removed, we argue that the outgoing power should really be maximized, not minimized, in order to obtain high Q cavities.

1.2.2 Our approach

Unlike previous optimization work which focused on Q and/or V, in chapter 4 we start with a more fundamental quantity: the local density of states LDOS($\mathbf{x}, \omega$) (the number of states per unit volume per frequency) [50], defined precisely in section 4.3. We show that the LDOS or its variants are the most relevant figures of merit for light-matter interaction applications. The well-known Purcell factor Q/V and variations

thereof (sections 4.3 and B.1) are only approximations of the LDOS in the limit of high-Q cavities. Another advantage of the LDOS is its ease to compute, because it is well-known that the LDOS is related to the imaginary part of the Green's function, which is a solution to an electromagnetic scattering problem [25, 79, 90].

What does the LDOS look like? For a system without any loss, the LDOS$(\mathbf{x}, \omega)$ is simply a sum of Dirac delta functions at the eigenfrequencies, as described in section B.2. For a system with loss, the eigenvalues to the Maxwell eigenproblem are complex, and the LDOS$(\mathbf{x}, \omega)$ becomes a sum of Lorentzian peaks centered at its resonant frequencies. For illustration purpose, we plot the LDOS$(\mathbf{x}, \omega)$ at the center of a photonic crystal cavity (inset of figure 1-7) versus ω as the blue curve in figure 1-7.
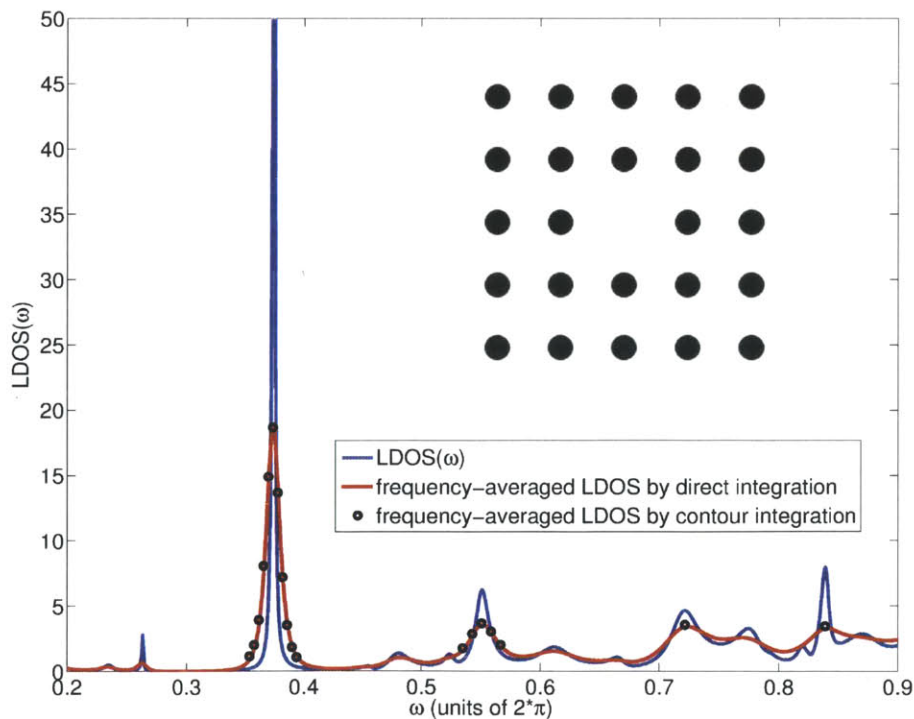
Figure 1-7: The illustration of the LDOS and frequency-averaged LDOS versus ω. The blue curve is the plot of the LDOS (at the center of a cavity, sketched in the inset), as a function of ω. The frequency-averaged LDOS with a bandwidth $\Gamma = \omega/80$, is computed by two methods: 1) direct integration (red curve), involving evaluating the LDOS at many real frequencies; 2) contour integration (black dots), only requiring the LDOS at one complex frequency.

Merely maximizing the LDOS at a single frequency, or equivalently the Q/V ratio (Purcell factor) of a cavity, is an uninteresting design problem because it has a trivial answer: infinity (e.g. for a ring resonator of infinite radius, in which Q diverges exponentially while V grows only linearly). Of course, one cannot achieve this in practice: Q is bounded in reality because of fabrication imperfections and material absorption, for example. Moreover, given a desired bandwidth and a loss tolerance, the required Q of the cavity is bounded and one is more interested in minimizing V given this Q. Equivalently, we want to maximize the LDOS over a given finite bandwidth, as described in section 4.4. In particular, we will maximize the mean of the LDOS(ω) over this bandwidth $L = \int_{-\infty}^{\infty} \text{LDOS}(\omega)W(\omega)d\omega$, where $W(\omega)$ is some weight/window function we choose, which has a peak around design frequency $\tilde{\omega}$ with bandwidth Γ (section 4.5). In our simple 2d cavity example, for a window function (the square of a Lorentzian with $\Gamma = \tilde{\omega}/80$) given in (4.26), the frequency-averaged LDOS is computed by direct numerical integration and plotted as the red curve in figure 1-7.

This direct method for computing the average L requires the LDOS over all ω, which involves solving scattering problems at many frequencies in the bandwidth. However, with the technique of contour integration in complex analysis, we convert the evaluation of the frequency-averaged LDOS (in section 4.4) into a single scattering problem at a complex frequency. Again, in our simple 2d PhC cavity example, the black dots in figure 1-7 are the frequency-averaged LDOS computed by this contour integration technique, and they agree quite well with direct numerical integration. Although such an application of complex analysis and contour integration to electromagnetic scattering problem is rather unusual, it is related to approaches more common in quantum field theory [96] and Casimir interactions in quantum field theory [56], and related ideas were recently applied to frequency averaged scattering cross-section in electromagnetism [47, 83].

Before we implement the parallel finite difference frequency domain (FDFD) Maxwell solver and run simulations with standard gradient-based optimization schemes in section 4.7, there is another important transformation to be applied. We show that

minimizing 1/LDOS is a better objective than maximizing LDOS, because this simple transformation turns a difficult narrow-ridge optimization problem into a simple shallow-valley one [86]. For silicon slabs, our numerical simulations discover a structure (figure 5-8) at reasonable large $Q = 30000$ with modal volume $0.06(\lambda/n)^3$, four times smaller than the smallest modal volume at same order of Q found in the literature [89].

Chapter 2

Capillary instabilities for concentric cylindrical shells

2.1 Introduction

In this chapter, which was published in [66], we generalize previous linear stability analyses [19, 101, 102, 112, 117] of Plateau–Rayleigh (capillary) instabilities in fluid cylinders to handle any number (N) of concentric cylindrical fluid shells with arbitrary thicknesses, viscosities, densities, and surface tensions. This analysis is motivated by the fact that experimental work is currently studying increasingly complicated fluid systems for device-fabrication applications, such as drawing of micro-structured optical fibers with concentric shells of different glasses/polymers [1, 29, 46, 63, 98, 110] or generating double emulsions [107, 119]. Although real experimental geometries may not be exactly concentric, we show that surface tension alone, in the absence of other forces, will tend to eliminate small deviations from concentricity. We show that our solution reduces to known results in several limiting cases, and we also validate it with full 3-dimensional Stokes-flow simulations. In addition, we show results for a number of situations that have not been previously studied. For the limiting case of a thin shell, we show a connection to the classic single-cylinder and flat-plane results, consistent with a similar result for air-clad two-fluid jets [19]. In a three-fluid system, we exhibit an interesting case in which two growth modes at different wavelengths

have the same effective growth rate, leading to competing breakup processes that we demonstrate with full 3-dimensional Stokes-flow simulations. We also consider some many-layer cases, including a limiting situation of a continuously varying viscosity. Using a simple geometrical argument, we generalize previous results [17, 97, 101] to show that only axial (not azimuthal) instabilities need be considered for cylindrical shells. Numerically, we show that the stability analysis in the Stokes regime can be reduced to a generalized eigenproblem whose solutions are the growth modes, which is easily tractable even for large numbers of layers. Like several previous authors [44, 45, 112, 117], we begin by considering the Stokes (low-Reynolds) regime, which is consistent with the high viscosities found in drawn-fiber devices [1, 29]. In section 2.11, we generalize the analysis to the full incompressible Navier-Stokes problem, which turns out to be a relatively minor modification once the Stokes problem is understood, although it has the complication of yielding an unavoidably nonlinear eigenproblem for the growth modes.

Let me begin by briefly reviewing the powerful tool, linear stability analysis, first introduced by Lord Rayleigh [101]. In linear stability analysis, one expands the radius R as a function of axial coordinate z in the form $R(z) = R_0 + \delta R e^{ikz - i\omega t}$, where $\delta R \ll R_0$, $2\pi/k$ is a wavelength of the instability, and $\sigma = \text{Im}\,\omega$ is an exponential growth rate. Given a geometry, one solves for the dispersion relation(s) $\omega(k)$ and considers the most unstable growth mode with the growth rate $\sigma_{\max}$ to determine the time scale of the breakup process. The wavelength $2\pi/k$ corresponding to $\sigma_{\max}$ has been experimentally verified to match the disintegration size of liquid jets [37].

We now formulate the mathematical problem that we solve, as depicted schematically in figure 2-1. The total number of viscous fluids is N and the viscosity of n-th $(n = 1, 2, \cdots, N)$ fluid is $\mu^{(n)}$. The surface-tension coefficient between the n-th and $(n + 1) - \text{th}$ fluid is denoted by $\gamma^{(n)}$. For the unperturbed steady state (figure 2-1b), we assume that the n-th fluid is in a cylindrical shell geometry with outer radius $R^{(n)}$ and inner radius $R^{(n-1)} < R^{(n)}$. The first $(n = 1)$ fluid is the innermost core and the N-th fluid is the outermost one (extending to infinity), so we set $R^{(0)} = 0$ and $R^{(N)} = +\infty$. To begin with, this system is analyzed in the Stokes regime (low

(a) Azimuthal cross-section   (b) Steady state   (c) Perturbed state
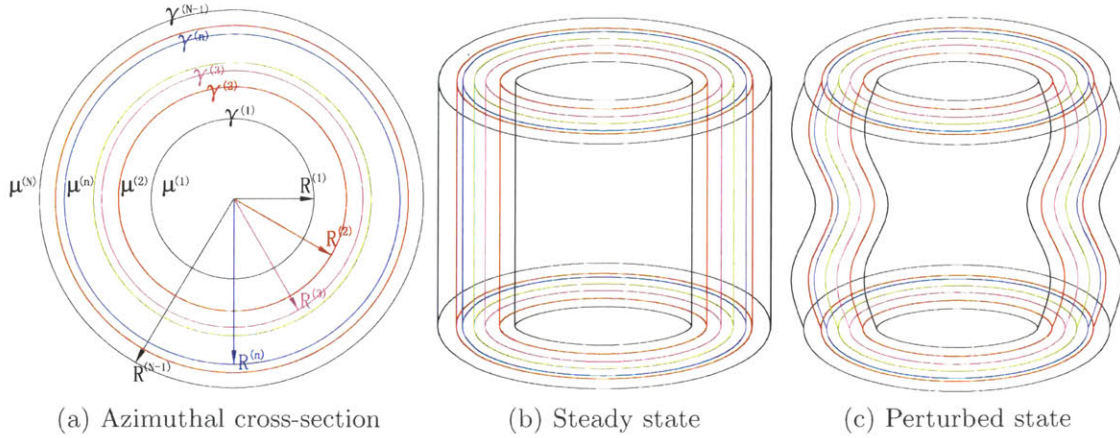
Figure 2-1: Schematic of the concentric-cylinder geometry considered in this chapter. (a) cross-section of N layers and corresponding radii $R^{(n)}$, viscosities $\mu^{(n)}$, and surface tensions $\gamma^{(n)}$. Starting with the perfect cylindrical geometry (b), we then introduce small sinusoidal perturbations (c) and analyze their growth with linear stability analysis.

Reynolds number) and we also neglect gravity [in the large Froude number limit, valid for fiber-drawing [28]], so the fluid densities are irrelevant. In Section 2.11, we extend this analysis to the Navier–Stokes regime, including an inertia term for each layer (with density $\rho^{(n)}$). As noted above, linear stability analysis consists of perturbing each interface $R^{(n)}$ by a small sinusoidal amount $\delta R^{(n)} e^{ikz - i\omega t}$, to lowest order in $\delta R^{(n)}$. Stokes' equations are then solved in each layer in terms of Bessel functions, and matching boundary conditions yields a set of equations relating ω and k. Although these equations can be cast in the form of a polynomial root-finding problem, similar to [117], such a formulation turns out to be ill-conditioned for large N, and instead we formulate it in the Stokes regime as a generalized eigenproblem of the form $\mathsf{M}_2(k)\boldsymbol{\xi} = i\omega \mathsf{M}_1(k)\boldsymbol{\xi}$, which is easily solved for the dispersion relations $\omega(k)$ (with the corresponding eigenvectors $\boldsymbol{\xi}$ yielding the relative amplitudes of each layer). In the Navier–Stokes regime, this becomes a nonlinear eigenproblem.

2.2   Azimuthal stability

For any coupled-fluids system of the type described in figure 2-1, a natural question to ask is whether that system is stable subject to a small perturbation. If an inter-

face with area $\mathcal{S}$ has surface energy $\gamma\mathcal{S}$, then a simple way to check stability is to compare surface energies (areas) for an initial configuration and a slightly deformed configuration with the same volume. In this way, it was shown that any azimuthal deformation is stable for a single cylindrical jet [17, 101]. Here, we employ a similar approach to demonstrate that same property also holds for multiple concentric cylindrical shells. Note that this analysis only indicates whether a system is stable; in order to determine the time scale of an instability, we must use linear stability analysis as described in subsequent sections.

For the unperturbed system, we define the level-set function $\bar{\phi}^{(n)} = r - R^{(n)}$. $\bar{\phi}^{(n)} = 0$ defines the interface between the n-th and $(n+1)$-th fluids. Similarly, we define the level-set function for the perturbed interface (figure 2-1c) between the n-th and $(n+1)$-th fluids by

$$\phi^{(n)}(r, z, \phi) = r - \zeta^{(n)}(z, \phi). \tag{2.1}$$

Following the method of normal modes [33], in the limit of small perturbations, a disturbed interface $\zeta^{(n)}$ can be chosen in the form

$$\zeta^{(n)}(z, \phi) = R^{(n)} + \delta R^{(n)} e^{i(kz+m\phi)} + O[(\delta R^{(n)})^2], \tag{2.2}$$

Assuming incompressible fluids in each layer so that volume is conserved (and assuming that the cylinder is much longer than its diameter so that any inflow/outflow at the end facets is negligible), we obtain a relation between $\zeta^{(n)}$ and $R^{(n)}$

$$\zeta^{(n)}(z, \phi) = R^{(n)} + \delta R^{(n)} e^{i(kz+m\phi)} - \frac{(\delta R^{(n)})^2}{4R^{(n)}} + O[(\delta R^{(n)})^3]. \tag{2.3}$$

Let $\mathcal{S}(\phi^{(n)})$ denote the surface area of $\phi^{(n)}(r, z, \phi) = 0$ in one wavelength $2\pi/k$. From equations (2.1) and (2.2), $\mathcal{S}(\phi^{(n)})$ can be expressed in cylindrical coordinates as:

$$\mathcal{S}(\phi^{(n)}) = \int_0^{\frac{2\pi}{k}} \int_0^{2\pi} \zeta^{(n)}(z, \phi) \sqrt{1 + (\frac{\partial \zeta^{(n)}}{\partial z})^2 + (\frac{1}{\zeta^{(n)}} \frac{\partial \zeta^{(n)}}{\partial \phi})^2} d\phi dz. \tag{2.4}$$

Now we can compare the total interfacial energy between the unperturbed system

38

$\bar{\mathcal{E}} = \sum_{n=1}^{N-1} \gamma^{(n)} \mathcal{S}(\bar{\phi}^{(n)})$ and the perturbed system $\mathcal{E} = \sum_{n=1}^{N-1} \gamma^{(n)} \mathcal{S}(\phi^{(n)})$:

$$\mathcal{E} - \bar{\mathcal{E}} = \sum_{n=1}^{N-1} \gamma^{(n)} \left[\mathcal{S}(\phi^{(n)}) - \mathcal{S}(\bar{\phi}^{(n)}) \right]$$

$$= \sum_{n=1}^{N-1} \gamma^{(n)} (\delta R^{(n)})^2 \pi^2 \frac{(kR^{(n)})^2 + m^2 - 1}{kR^{(n)}} + O[(\delta R^{(n)})^3]. \tag{2.5}$$

From the surface-energy point of view, small perturbations will grow only if $\mathcal{E} - \bar{\mathcal{E}} < 0$. Therefore, from (2.5), we can conclude that all the non-axisymmetric perturbations ($m \neq 0$) will be stable. There is one special case that needs additional consideration: if $k = 0$ and $m = 1$ in (2.5), the first term is zero, so one must consider the next-order term in order to show that this case is indeed stable (i.e. elliptical perturbations decay). Even more straightforwardly, however, $k = 0$ corresponds to a two-dimensional problem, in which case it is well known that the minimal surface enclosing a given area is a circle.

2.3   Linear stability analysis

In the previous section, we showed that only axisymmetric perturbations can lead to instability of concentric cylinders. Now we will use linear stability analysis to find out how fast the axisymmetric perturbations grow and estimate the break-up time scale for a coupled N-layer system.

Here, we consider fluids in the low Reynolds number regime [valid for fiber-drawing [1, 29]] and thus the governing equations of motion for each fluid are the Stokes equations [91]. The full Navier–Stokes equations are considered in Section 2.11. For the axisymmetric flow, the velocity profile of the n-th fluid is $\boldsymbol{u}^{(n)} = [u_r^{(n)}(r, z, t), u_z^{(n)}(r, z, t)]$, where $u_r^{(n)}$ is the radial component of the velocity and $u_z^{(n)}$ is the axial component of the velocity. The dynamic pressure in the n-th fluid is denoted by $p^{(n)}$. The Stokes

equations [12] are:

$$\mu^{(n)} \left(\frac{\partial^2 u_r^{(n)}}{\partial r^2} + \frac{1}{r} \frac{\partial u_r^{(n)}}{\partial r} - \frac{u_r^{(n)}}{r^2} + \frac{\partial^2 u_r^{(n)}}{\partial z^2} \right) = \frac{\partial p^{(n)}}{\partial r} \tag{2.6a}$$

$$\mu^{(n)} \left(\frac{\partial^2 u_z^{(n)}}{\partial r^2} + \frac{1}{r} \frac{\partial u_z^{(n)}}{\partial r} + \frac{\partial^2 u_z^{(n)}}{\partial z^2} \right) = \frac{\partial p^{(n)}}{\partial z} \tag{2.6b}$$

and the continuity equation (for incompressible fluids) is

$$\frac{\partial u_r^{(n)}}{\partial r} + \frac{u_r^{(n)}}{r} + \frac{\partial u_z^{(n)}}{\partial z} = 0. \tag{2.7}$$

2.3.1 Steady state

Because of the no-slip boundary conditions of viscous fluids, without loss of generality, we can take the equilibrium state of the outermost fluid to be

$$\bar{u}_r^{(N)} = 0 \qquad \bar{u}_z^{(N)} = 0 \qquad \bar{p}^{(N)} = 0 \tag{2.8}$$

for $r > R^{(N-1)}$, and of the n-th ($n < N$) fluid to be

$$\bar{u}_r^{(n)} = 0 \qquad \bar{u}_z^{(n)} = 0 \qquad \bar{p}^{(n)} = \sum_{j=n}^{N-1} \frac{\gamma^{(j)}}{R^{(j)}} \tag{2.9}$$

for $R^{(n-1)} < r < R^{(n)}$. (In Section 2.11, we generalize this to nonzero initial relative velocities for the case of inviscid fluids, where no-slip boundary conditions are not applied.)

2.3.2 Perturbed state

The perturbed interface, corresponding to the level set $\phi^{(n)} = r - \zeta^{(n)} = 0$, with an axisymmetric perturbation, takes the form

$$\zeta^{(n)}(z,t) = R^{(n)} + \delta R^{(n)} e^{i(kz - \omega t)} + O[(\delta R^{(n)})^2]. \tag{2.10}$$

40

Similarly, the perturbed velocity and pressure are of the form

$$\begin{bmatrix} u_r^{(n)}(r,z,t) \\ u_z^{(n)}(r,z,t) \\ p^{(n)}(r,z,t) \end{bmatrix} = \begin{bmatrix} \bar{u}_r^{(n)} \\ \bar{u}_z^{(n)} \\ \bar{p}^{(n)} \end{bmatrix} + \begin{bmatrix} \delta u_r^{(n)}(r) \\ \delta u_z^{(n)}(r) \\ \delta p^{(n)}(r) \end{bmatrix} e^{i(kz-\omega t)}. \tag{2.11}$$

Note that the Stokes equations (2.6) and continuity equation (2.7) imply that

$$\frac{\partial^2 p^{(n)}}{\partial r^2} + \frac{1}{r}\frac{\partial p^{(n)}}{\partial r} + \frac{\partial^2 p^{(n)}}{\partial z^2} = 0. \tag{2.12}$$

Substituting the third row of (2.11) into (2.12), we obtain an ordinary differential equation for $\delta p^{(n)}(r)$

$$\left(\frac{d^2}{dr^2} + \frac{1}{r}\frac{d}{dr} - k^2 \right) \delta p^{(n)}(r) = 0. \tag{2.13}$$

Clearly, $\delta p^{(n)}(r)$ satisfies the modified Bessel equation of order zero in terms of kr. Therefore, we have

$$\delta p^{(n)}(r) = c_1^{(n)} K_0(kr) + c_2^{(n)} I_0(kr), \tag{2.14}$$

where $K_0(\cdot)$ and $I_0(\cdot)$ are modified Bessel functions of the first and second kind (K_0 is exponentially decreasing and singular at origin; I_0 is exponentially growing), and $c_1^{(n)}$ and $c_2^{(n)}$ are constants to be determined. Inserting $\delta p^{(n)}(r)$ into (2.6) and solving two inhomogeneous differential equations, we obtain the radial component of velocity

$$\delta u_r^{(n)}(r) = c_1^{(n)} \frac{r K_0(kr)}{2\mu^{(n)}} + c_2^{(n)} \frac{r I_0(kr)}{2\mu^{(n)}} + c_3^{(n)} \frac{K_1(kr)}{2\mu^{(n)}k} + c_4^{(n)} \frac{I_1(kr)}{2\mu^{(n)}k} \tag{2.15}$$

and the axial component of velocity

$$\delta u_z^{(n)}(r) = c_1^{(n)} \left[\frac{i K_0(kr)}{\mu^{(n)}k} - \frac{ir K_1(kr)}{2\mu^{(n)}} \right] + c_2^{(n)} \left[\frac{i I_0(kr)}{\mu^{(n)}k} + \frac{ir I_1(kr)}{2\mu^{(n)}} \right]$$
$$- c_3^{(n)} \frac{i K_0(kr)}{2\mu^{(n)}k} + c_4^{(n)} \frac{i I_0(kr)}{2\mu^{(n)}k}, \tag{2.16}$$

41

where $c_3^{(n)}$ and $c_4^{(n)}$ are constants to be determined. Imposing the conditions that the velocity and pressure must be finite at $r = 0$ and $r = +\infty$, we immediately have

$$c_1^{(1)} = c_3^{(1)} = c_2^{(N)} = c_4^{(N)} = 0. \tag{2.17}$$

2.3.3 Boundary conditions

In order to determine the unknown constants $\boldsymbol{c}^{(n)} = (c_1^{(n)}, c_2^{(n)}, c_3^{(n)}, c_4^{(n)})$ in each layer, we close the system by imposing boundary conditions at each interface. Let $\boldsymbol{n}^{(n)}$ be the unit outward normal vector of interface $r = \zeta^{(n)}(z, t)$ and $\boldsymbol{t}^{(n)}$ be the unit tangent vector. Formulas for $\boldsymbol{n}^{(n)}$ and $\boldsymbol{t}^{(n)}$ are given by equations (A.1) and (A.2) of Appendix A.1. First, the normal component of the velocity is continuous at the interface, since there is no mass transfer across the interface, and so

$$\boldsymbol{u}^{(n)}\big|_{r=\zeta^{(n)}} \cdot \boldsymbol{n}^{(n)} = \boldsymbol{u}^{(n+1)}\big|_{r=\zeta^{(n)}} \cdot \boldsymbol{n}^{(n)}. \tag{2.18}$$

For the at-rest steady state (2.8) and (2.9), this condition is equivalent (to first order) to the continuity of radial velocity:

$$u_r^{(n)}(r, z, t)\big|_{r=\zeta^{(n)}} = u_r^{(n+1)}(r, z, t)\big|_{r=\zeta^{(n)}}. \tag{2.19}$$

Second, the no-slip boundary condition implies that the tangential component of the velocity is continuous at the interface:

$$\boldsymbol{u}^{(n)}\big|_{r=\zeta^{(n)}} \cdot \boldsymbol{t}^{(n)} = \boldsymbol{u}^{(n+1)}\big|_{r=\zeta^{(n)}} \cdot \boldsymbol{t}^{(n)}. \tag{2.20}$$

(The generalization to inviscid fluids, where no-slip boundary conditions are not applied, is considered in Section 2.11.) For the at-rest steady state (2.8) and (2.9), this is equivalent (to first order) to the continuity of axial velocity:

$$u_z^{(n)}(r, z, t)\big|_{r=\zeta^{(n)}} = u_z^{(n+1)}(r, z, t)\big|_{r=\zeta^{(n)}}. \tag{2.21}$$

42

Third, the tangential stress of the fluid is continuous at the interface. The stress tensor of the n-th fluid in cylindrical coordinates for axisymmetric flow [62] can be expressed as

$$\tau^{(n)} = \begin{bmatrix} -p^{(n)} + 2\mu^{(n)}\frac{\partial u_r^{(n)}}{\partial r} & \mu^{(n)}\left(\frac{\partial u_r^{(n)}}{\partial z} + \frac{\partial u_z^{(n)}}{\partial r}\right) \\ \mu^{(n)}\left(\frac{\partial u_r^{(n)}}{\partial z} + \frac{\partial u_z^{(n)}}{\partial r}\right) & -p^{(n)} + 2\mu^{(n)}\frac{\partial u_z^{(n)}}{\partial z} \end{bmatrix}. \tag{2.22}$$

The continuity of the tangential stress at the interface implies that

$$\boldsymbol{n}^{(n)} \cdot \tau^{(n)}\big|_{r=\zeta^{(n)}} \cdot \boldsymbol{t}^{(n)} = \boldsymbol{n}^{(n)} \cdot \tau^{(n+1)}\big|_{r=\zeta^{(n)}} \cdot \boldsymbol{t}^{(n)}, \tag{2.23}$$

The leading term of (2.23) leads to

$$\mu^{(n)}\left(\frac{\partial u_r^{(n)}}{\partial z} + \frac{\partial u_z^{(n)}}{\partial r}\right)\big|_{r=\zeta^{(n)}} = \mu^{(n+1)}\left(\frac{\partial u_r^{n+1}}{\partial z} + \frac{\partial u_z^{n+1}}{\partial r}\right)\big|_{r=\zeta^{(n)}}. \tag{2.24}$$

Fourth, the jump of the normal stress across the interface must be balanced by the surface-tension force per unit area. The equation for normal stress balance at the interface is

$$\boldsymbol{n}^{(n)} \cdot \left(\tau^{(n+1)} - \tau^{(n)}\right)\big|_{r=\zeta^{(n)}} \cdot \boldsymbol{n}^{(n)} = \gamma^{(n)}\kappa^{(n)}, \tag{2.25}$$

where $\kappa^{(n)}(r, z, t)$ is the mean curvature of the interface. The curvature can be calculated directly from the unit outward normal vector of the interface by $\kappa^{(n)} = \boldsymbol{\nabla} \cdot \boldsymbol{n}^{(n)}$ (see Appendix A.1). Substituting (2.22), (A.1), and (A.5) into (2.25), we have following equation (accurate to first order in $\delta R^{(n)}$) for the dynamic boundary condition:

$$\left[-p^{(n+1)} + 2\mu^{(n+1)}\frac{\partial u^{(n+1)}}{\partial r} - \left(-p^{(n)} + 2\mu^{(n)}\frac{\partial u_r^{(n)}}{\partial r}\right)\right]\big|_{r=\zeta^{(n)}}$$

$$= \gamma^{(n)}\left[\frac{1}{R^{(n)}} + \frac{\delta u_r^{(n)}(R^{(n)})}{-\mathrm{i}\omega}\left(k^2 - \frac{1}{(R^{(n)})^2}\right)\mathrm{e}^{\mathrm{i}(kz-\omega t)}\right]. \tag{2.26}$$

2.3.4 Dispersion relation

Substituting (2.11) and (2.14)–(2.16) into the boundary conditions [(2.19), (2.21), (2.24) and (2.26)] and keeping the leading terms, we obtain a linear system in terms of

43

the unknown constants $\boldsymbol{c}^{(n)} = (c_1^{(n)}, c_2^{(n)}, c_3^{(n)}, c_4^{(n)})$. After some algebraic manipulation, these equations can be put into a matrix form:

$$\left(\mathsf{A}^{(n,n)} + \frac{1}{-i\omega} \mathsf{B}^{(n)} \right) \boldsymbol{c}^{(n)} - \mathsf{A}^{(n,n+1)} \boldsymbol{c}^{(n+1)} = 0, \qquad (2.27)$$

where $\mathsf{A}^{(n,n')}$ and $\mathsf{B}^{(n)}$ are 4×4 matrices given below.

$$\mathsf{A}^{(n,n')} = \begin{bmatrix} \dfrac{kR^{(n)}K_0^{(n)}}{\mu^{(n')}} & \dfrac{kR^{(n)}I_0^{(n)}}{\mu^{(n')}} & \dfrac{K_1^{(n)}}{\mu^{(n')}} & \dfrac{I_1^{(n)}}{\mu^{(n')}} \\ \dfrac{2K_0^{(n)} - kR^{(n)}K_1^{(n)}}{\mu^{(n')}} & \dfrac{2I_0^{(n)} + kR^{(n)}I_1^{(n)}}{\mu^{(n')}} & -\dfrac{K_0^{(n)}}{\mu^{(n')}} & \dfrac{I_0^{(n)}}{\mu^{(n')}} \\ kR^{(n)}K_0^{(n)} - K_1^{(n)} & kR^{(n)}I_0^{(n)} + I_1^{(n)} & K_1^{(n)} & I_1^{(n)} \\ kR^{(n)}K_1^{(n)} & -kR^{(n)}I_1^{(n)} & K_0^{(n)} + \dfrac{K_1^{(n)}}{kR^{(n)}} & -I_0^{(n)} + \dfrac{I_1^{(n)}}{kR^{(n)}} \end{bmatrix},$$

$$(2.28)$$

$$\mathsf{B}^{(n)} = \frac{-\gamma^{(n)}k\left(1 - \frac{1}{(kR^{(n)})^2}\right)}{2\mu^{(n)}} \begin{bmatrix} 0 & 0 & 0 & 0 \\ 0 & 0 & 0 & 0 \\ 0 & 0 & 0 & 0 \\ kR^{(n)}K_0^{(n)} & kR^{(n)}I_0^{(n)} & K_1^{(n)} & I_1^{(n)} \end{bmatrix}, \qquad (2.29)$$

Here, $K_0^{(n)}, K_1^{(n)}, I_0^{(n)}$ and $I_1^{(n)}$ denote the corresponding modified Bessel functions evaluated at $kR^{(n)}$. Combining the boundary conditions from all $N - 1$ interfaces, we have the matrix equation

$$\mathsf{M}^{(N)}\boldsymbol{\xi} = 0 \qquad (2.30)$$

44

for the undetermined constants $\boldsymbol{\xi} = (c_2^{(1)}, c_4^{(1)}, \boldsymbol{c}^{(2)}, \boldsymbol{c}^{(3)}, \cdots, \boldsymbol{c}^{(N-1)}, c_1^{(N)}, c_3^{(N)})$, with

$$
\mathsf{M}^{(N)} = \mathsf{M}_1^{(N)} + \frac{1}{-i\omega}\mathsf{M}_2^{(N)}
$$

$$
= \begin{bmatrix}
\tilde{\mathsf{A}}^{(1,1)} & -\mathsf{A}^{(1,2)} & & & & \\
& \mathsf{A}^{(2,2)} & -\mathsf{A}^{(2,3)} & & & \\
& & \ddots & \ddots & & \\
& & & \mathsf{A}^{(N-2,N-2)} & -\mathsf{A}^{(N-2,N-1)} & \\
& & & & \mathsf{A}^{(N-1,N-1)} & -\tilde{\mathsf{A}}^{(N-1,N)}
\end{bmatrix}
$$

$$
+ \frac{1}{-i\omega} \begin{bmatrix}
\tilde{\mathsf{B}}^{(1)} & 0 & & & & \\
& \mathsf{B}^{(2)} & 0 & & & \\
& & \ddots & \ddots & & \\
& & & \mathsf{B}^{(N-2)} & 0 & \\
& & & & \mathsf{B}^{(N-1)} & 0
\end{bmatrix}, \quad (2.31)
$$

where $\tilde{\mathsf{A}}^{(1,1)}$ and $\tilde{\mathsf{B}}^{(1)}$ are the second and fourth columns of $\mathsf{A}^{(1,1)}$ and $\mathsf{B}^{(1)}$, and $\tilde{\mathsf{A}}^{(N-1,N)}$ is the first and third columns of $\mathsf{A}^{(N-1,N)}$. To obtain a non-trivial solution of equation (2.30), the coefficient matrix $\mathsf{M}^{(N)}$ must be singular, namely

$$
\det(\mathsf{M}^{(N)}) = 0. \quad (2.32)
$$

Since $\mathsf{B}^{(n)}$ is zero except in its fourth row, ω only occurs in the 4th, 8th, $\cdots$, $4(N-1)$-th rows of $\mathsf{M}^{(N)}$. The Leibniz formula implies that equation (2.32) is a polynomial in $1/\omega$ with degree $N-1$. Therefore, we could obtain the dispersion relation $\omega = \omega(k)$ by solving the polynomial equation (2.32). Instead, to counteract roundoff-error problems, we solve the corresponding generalized eigenvalue problem as described in § 2.4.

2.3.5   Eigen-amplitude and maximum growth rate

The $N-1$ roots of (2.32) are denoted by $\omega_j(k)$, where $j = 1, 2, \cdots, N-1$. Since $\mathsf{M}^{(N)}$ is singular when $\omega = \omega_j$, $\boldsymbol{\xi}$ can be determined by equation (2.30) up to a proportional-

45

ity constant. Therefore, for each $\omega_j(k)$, the corresponding perturbed amplitude $\delta R_j^{(n)}$ on the n-th interface can also be determined up to a proportionality constant by equations (2.15) and (A.4). Let us call the vector $\boldsymbol{\delta R_j} = (\delta R_j^{(1)}, \delta R_j^{(2)}, \cdots, \delta R_j^{(n)}, \cdots, \delta R_j^{(N-1)})$, where we normalize $\|\boldsymbol{\delta R_j}\|_1 = 1$, the "eigen-amplitudes" of frequency ω_j. Any arbitrary initial perturbation amplitudes $\boldsymbol{A} = (A^{(1)}, A^{(2)}, \cdots, A^{(N-1)})$ can be decomposed into a linear combination of eigen-amplitudes, namely $\boldsymbol{A} = \sum_{j=1}^{N-1} a_j \boldsymbol{\delta R_j}$ for some a_j. Since the whole coupled system is linear, the small initial perturbation $\boldsymbol{A}\mathrm{e}^{\mathrm{i}kz}$ will grow as $\sum_{j=1}^{N-1} a_j \boldsymbol{\delta R_j} \mathrm{e}^{\mathrm{i}[kz - \omega_j(k)t]}$.

The growth rate for a single mode is $\sigma_j(k) = \mathrm{Im}\,\omega_j(k)$ since our time dependence is $\mathrm{e}^{-\mathrm{i}\omega_j t}$. If $\sigma_j > 0$, then the mode is unstable. As described above, for an N-layer system, we have $N - 1$ different growth rates for a single k, and we denote the largest growth rate by $\sigma_{\max}(k) = \max_j[\sigma_j(k)]$. Moreover, the maximum growth rate over all k is denoted by $\sigma_{\max} = \max_k[\sigma_{\max}(k)] = \max_{j,k}[\sigma_j(k)]$, and the corresponding eigen-amplitudes of this most-unstable mode are denoted by $\boldsymbol{\delta R}_{\max}$. $k_{\max}$ denotes the corresponding wavenumber.

2.4 Generalized eigenvalue problem

It is well known that finding the roots of a polynomial via its coefficients is badly ill-conditioned [118]. Correspondingly, we find that solving the determinant equation (2.32) directly, by treating it as a polynomial, is highly susceptible to roundoff errors when N is not small. In particular, it is tempting to use the block structure of $\mathsf{M}^{(N)}$ to reduce (2.32) to a 4×4 determinant problem via a recurrence. However, the entries of this 4×4 matrix are high-degree polynomials in ω whose coefficients thereby introduce roundoff ill-conditioning. Instead, we can turn this ill-conditioned root-finding problem into a generalized eigenvalue problem by exploiting the matrix-pencil structure of $\mathsf{M}^{(N)}$:

$$\mathsf{M}^{(N)}\boldsymbol{\xi} = 0 \Leftrightarrow \mathsf{M}_2^{(N)}(k)\boldsymbol{\xi} = \mathrm{i}\omega \mathsf{M}_1^{(N)}(k)\boldsymbol{\xi}. \tag{2.33}$$

Thus, finding the dispersion relation $\omega(k)$ turns out to be a generalized eigenvalue problem with matrices $(\mathsf{M}_1^{(N)}, \mathsf{M}_2^{(N)})$. Since $\mathsf{M}_1^{(N)}$ is non-singular, this (regular) generalized eigenvalue problem is typically well-conditioned [27] and can be solved via available numerical methods [6]. In principle, further efficiency gains could be obtained by exploiting the sparsity of this pencil, but dense solvers are easily fast enough for N up to hundreds.

2.5 Validation of our formulation

As a validation check, our N-layer results can be checked against known analytical results in various special cases. We can also compare to previous finite-element calculations [28].

2.5.1 Tomotika's case: $N = 2$

[117] discussed the instability of one viscous cylindrical thread surrounded by another viscous fluid, which is equivalent to our model with $N = 2$. It is easy to verify that $\det(\mathsf{M}^{(2)}) = 0$, where $\mathsf{M}^{(2)} = [\tilde{\mathsf{A}}^{(1)} + \frac{1}{-\mathrm{i}\omega}\tilde{\mathsf{B}}^{(1)}, \tilde{\mathsf{D}}^{(1)}]$, gives the same determinant equation as (34) in [117].

Compared with the Stokes-equations approach, Tomotika begun with the full Navier–Stokes equations, treating the densities of the inner fluid ρ' and the outer fluid ρ as small parameters and taking a limit to reach the Stokes regime. However, special procedures must be taken in order to obtain a meaningful determinant equation in this limit, because substituting $\rho' = 0$ and $\rho = 0$ directly would result in dependent columns in the determinant. Tomotika proposed a procedure of expanding various functions in ascending powers of ρ and ρ', subtracting the leading terms in dependent columns, dividing a quantity proportional to $\rho\rho'$, and finally taking limit of $\rho \to 0$ and $\rho' \to 0$. We generalize this idea to the N-shell problem in Section 2.11, but such procedures are unnecessary if the Stokes equations are used from the beginning.

47

2.5.2 $N = 3$ with equal viscosities $\mu^{(1)} = \mu^{(2)} = \mu^{(3)}$

This equal-viscosity case was first discussed by [112]. Putting this special case $\mu^{(1)} = \mu^{(2)} = \mu^{(3)}$ into (2.32) and solving it with Matlab's Symbolic Math Toolbox (MuPad), we obtain the same solution as equation (8) in [112].

2.5.3 Navier–Stokes and inviscid cases

In Section 2.11, we validate the generalized form of our instability analysis against previous results for inviscid and/or Navier–Stokes problems. For example, we find identical results to [19] for the $N = 3$ case of a two-fluid compound jet surrounded by air (with negligible air density and viscosity).

2.5.4 Comparison with numerical experiments

[28] studied axisymmetric capillary instabilities of the concentric cylindrical shell problem ($N = 3$) for various viscosity contrasts by solving the full Navier–Stokes equation via finite-element methods. [The Stokes equation is a good approximation for their model, in which the Reynolds number is extremely low ($\mathrm{Re} \approx 10^{-10}$).] In particular, they input a fixed initial perturbation wavenumber k_0, evolve the axisymmetric equations, and fit the short-time behavior to an exponential in order to obtain a growth rate. With their parameters $R^{(1)} = 60$ μm, $R^{(2)} = 120\mu$m, $\gamma^{(1)} = \gamma^{(2)} = 0.6$N/m, $\mu^{(2)} = 10^5$ Pa·s, and $\mu^{(1)} = \mu^{(3)} = \eta\mu^{(2)}$ ($\eta = 10^{-4}, 10^{-3}, \cdots, 10^3$), we compute the maximum growth rate σ_{max} for each ratio η via the equation $\det(\mathsf{M}^{(3)}) = 0$. For comparison, we also compute the growth rate $\sigma_{\mathrm{max}}(k_0)$ for their fixed $k_0 = 7.9 \times 10^3\mathrm{m}^{-1}$. [Because numerical noise and boundary artifacts in the simulations will excite unstable modes at $k \neq k_0$, it is possible that σ_{max} and not $\sigma_{\mathrm{max}}(k_0)$ will dominate in the simulations even at short times if the former is much larger.] The inset of figure 2-2 plots the wavenumber k_{max} that results in the maximum growth rate versus the viscosity ratio η ($\mu^{(1,3)}/\mu^{(2)}$). In figure 2-2, we see that the growth rate obtained by [28] (represented by blue circles) agrees well with the growth rate $\sigma_{\mathrm{max}}(k_0)$ predicted by linear stability analysis (labeled by blue line) except at large viscosity
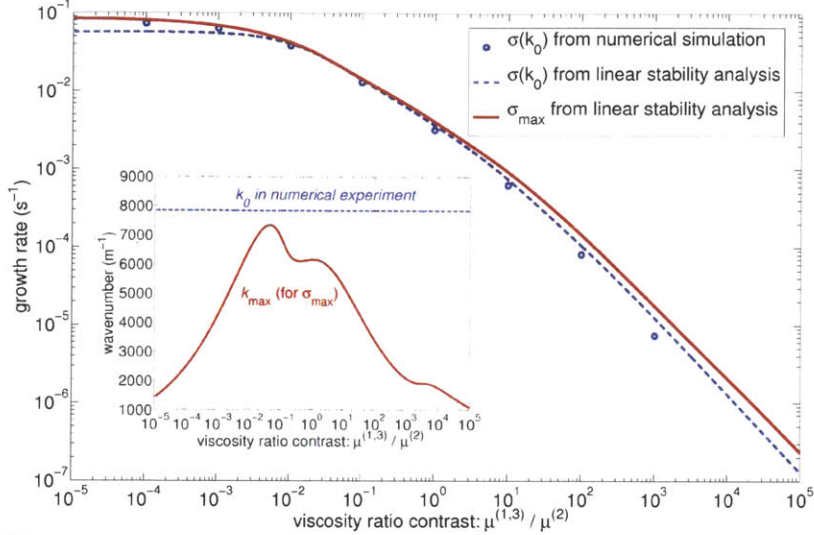
Figure 2-2: Comparison between linear stability analysis and numerical experiments [data from [28]] for $N = 3$ cylindrical-shell model. The growth rate $\sigma_{max}(k_0)$ computed by [28] numerically via the finite-element method (blue circles) agrees well with the growth rate predicted by linear stability analysis (dashed blue line), except for small discrepancies in the regime of large viscosity contrast where accurate numerical simulation is difficult. The red line indicates the maximum growth rate σ_{max} obtained by linear stability analysis. In the inset, the red line shows the wavenumbers k_{max} for various viscosity-ratio contrasts and the dashed blue line represents the fixed k_0 used in numerical simulations. Model parameters: $R^{(1)} = 60$ μm, $R^{(2)} = 120\mu$m, $\gamma^{(1)} = \gamma^{(2)} = 0.6$N/m, $\mu^{(2)} = 10^5$ Pa·s, $\mu^{(1)} = \mu^{(3)} = \eta\mu^{(2)}$ ($\eta = 10^{-4}, 10^{-3}, \cdots, 10^3$), and $k_0 = 7.9 \times 10^3 \text{m}^{-1}$.

contrasts ($\eta \gg 1$ or $\eta \ll 1$). These small discrepancies are due to the well-known numerical difficulties in accurately solving a problem with large discontinuities.

2.6 $N = 3$ examples

In this section, we study the three-fluid ($N = 3$) problem. Three or more concentric layers are increasingly common in novel fiber-drawing processes [1, 29, 46, 63, 98]. By exploring a couple of interesting limiting cases, in terms of shell viscosity and shell thickness, we reveal strong connections between the $N = 3$ case and the classic $N = 2$ problem.

2.6.1 Case $N = 3$ and $\mu^{(2)}/\mu^{(1,3)} \to 0$: shell viscosity $\ll$ cladding viscosity

We first consider the limiting case in which the shell viscosity $\mu^{(2)}$ is much smaller than the cladding viscosities $\mu^{(1)}$ and $\mu^{(3)}$. Substituting $\mu^{(2)}/\mu^{(1)} = 0$ and $\mu^{(2)}/\mu^{(3)} = 0$ into $\mathsf{M}^{(3)}$, equation (2.32) gives simple formulas for the growth rates

$$\sigma_1(k) = \frac{\gamma^{(1)}}{2\mu^{(1)}R^{(1)}} \frac{(kR^{(1)})^2 - 1}{1 + (kR^{(1)})^2 - (kR^{(1)})^2 \frac{I_0^2(kR^{(1)})}{I_1^2(kR^{(1)})}} \tag{2.34}$$

and

$$\sigma_2(k) = \frac{\gamma^{(2)}}{2\mu^{(3)}R^{(2)}} \frac{1 - (kR^{(2)})^2}{1 + (kR^{(2)})^2 - (kR^{(2)})^2 \frac{K_0^2(kR^{(2)})}{K_1^2(kR^{(2)})}}. \tag{2.35}$$

Note that $\sigma_1(k)$ is independent of $\gamma^{(2)}$, $R^{(2)}$, and $\mu^{(3)}$, while $\sigma_2(k)$ is independent of $\gamma^{(1)}$, $R^{(1)}$, and $\mu^{(1)}$. In particular, these growth rates are *exactly* the single-cylinder results predicted by Tomotika's model, as if the inner and outer layers were entirely decoupled. This result is not entirely obvious, because even if the shell viscosity can be neglected, it is still incompressible and hence might be thought to couple the inner and outer interfaces. [[28] conjectured a similar decoupling, but only in the form of a dimensional analysis.]

Case $N = 3$, $\mu^{(2)}/\mu^{(1,3)} \to 0$ and $R^{(2)} \to \infty \iff N = 2$ and $\mu_{\text{out}}/\mu_{\text{in}} \to 0$

In the regime that the shell viscosity $\mu^{(2)}$ is much smaller than the cladding viscosities $\mu^{(1)}$ and $\mu^{(3)}$, we further consider the limit $R^{(2)} \to \infty$. It corresponds to the case $N = 2$ with a high viscous fluid embedded in another low viscosity fluid, which must of course correspond exactly to Tomotika's case. From the asymptotic formulas of modified Bessel functions $K_0(z)$ and $K_1(z)$ for large arguments [2], we obtain

$$\sigma_2(k) \approx -\frac{\gamma^{(2)}|k|}{2\mu^{(3)}} < 0 \qquad \text{as} \qquad R^{(2)} \to +\infty. \tag{2.36}$$

Thus, the growth rate of possible unstable modes is given by $\sigma_1(k)$ in equation (2.34). Tomotika discussed this limiting case ($N = 2$) and gave a formula (37) [117], which

is exactly (2.34).

Case $N = 3, \mu^{(2)}/\mu^{(1,3)} \to 0$ and $R^{(1)} \to 0 \Longleftrightarrow N = 2$ and $\mu_{out}/\mu_{in} \to \infty$

The limit $R^{(1)} \to 0$ is equivalent to $N = 2$ with a low-viscous fluid embedded in a high-viscosity fluid. For this case, it is easy to check that $\sigma_2(k)$ in equation (2.35) agrees with formula (36) in [117]. However, we still have another unstable mode with a growth rate $\sigma_1(k)$. Using the asymptotic formulas for $I_0(z)$ and $I_1(z)$ with small arguments [2], we obtain

$$\sigma_1(k) \sim \frac{\gamma^{(1)}}{6\mu^{(1)}R^{(1)}} \qquad \text{as} \qquad R^{(1)} \to 0. \tag{2.37}$$

This extra unstable mode $\sigma_1(k)$ results from the instability of a viscous cylinder with infinitesimally small radius $R^{(1)}$. In other words, (2.37) is the growth rate of a viscous cylinder in the air with a tiny but nonzero radius, which is also given by equation (35) of [102].

2.6.2 Thin shell case: $R^{(2)} = R^{(1)}(1 + \varepsilon)$, $\varepsilon \to 0$

Next, we study a three-layer structure with a very thin middle shell; that is, $R^{(2)} = R^{(1)}(1 + \varepsilon)$ with $\varepsilon \to 0$. A sketch of such a geometry is given in figure 2-3a. This is motivated by a number of experimental drawn-fiber devices, which use very thin (submicron) layers in shells hundreds of microns in diameter in order to exploit optical interference effects [46, 63, 98].

Considering ε as a small parameter, we expand the determinant equation (2.32) in powers of ε. For a given wavenumber k, the two roots of this equation are $\sigma^+(k) = \sigma_0(k) + O(\varepsilon)$ and $\sigma^-(k) = O(\varepsilon^2)$, where $\sigma_0(k)$ can be computed analytically by dropping the terms of order $O(\varepsilon^2)$ in the determinant equation (2.32). After some algebraic manipulation, we find that $\sigma_0(k)$ actually is the solution for the $N = 2$ structure (i.e., ignoring the thin shell) with a modified surface-tension coefficient $\gamma^{(1)} + \gamma^{(2)}$. It is also interesting to consider a limit in which $\mu^{(2)}$ grows as ε shrinks. In this case, we find the same asymptotic results as long as $\mu^{(2)}/\mu^{(1,3)}$ grows more slowly
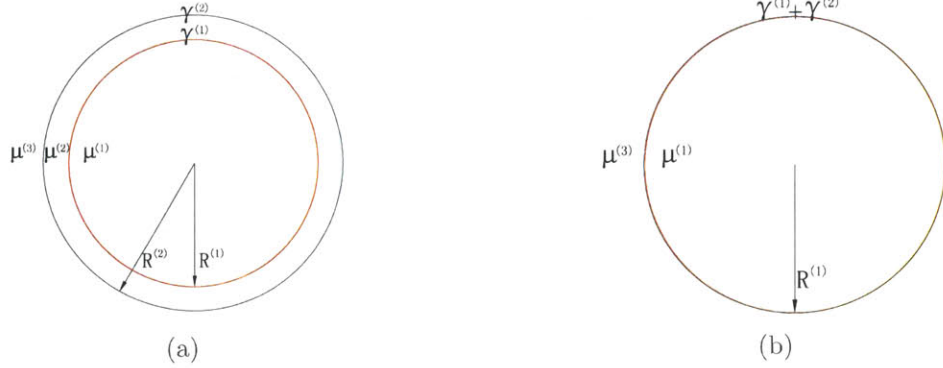
Figure 2-3: (a) Sketch of a very thin shell in a three-layer structure with radius $R^{(2)} = R^{(1)}(1 + \varepsilon)$, surface-tension coefficients $\gamma^{(1)}$ and $\gamma^{(2)}$. (b) In the limit of infinitesimal ε, we obtain an equivalent $N = 2$ geometry with a modified surface-tension coefficient $\gamma^{(1)} + \gamma^{(2)}$.

than $1/\varepsilon$. Conversely, if it grows faster than $1/\varepsilon$, then the thin-shell fluid acts like a "hard wall" and all growth rates vanish. Instead presenting a lengthy expression for $\sigma^+(k)$, we demonstrate a numerical verification in figure 2-4. As indicated in figure 2-4a, the growth rate $\sigma^+(k = 0.5)$ for $N = 3$ approaches to the growth rate of $N = 2$ with the summed surface-tension coefficients as $\varepsilon \to 0$. The parameters are $R^{(1)} = 1, \gamma^{(1)} = 1, \gamma^{(2)} = 2, \mu^{(1)} = 1, \mu^{(2)} = 2$ and $\mu^{(3)} = 3$. In figure 2-4b, we show that the growth rate $\sigma^-(k)$ decreases like ε^2 as $\varepsilon \to 0$.

To better understand these two modes, we consider the eigen-amplitudes at the two interfaces. For the mode with growth rate $\sigma^+(k)$, two interfaces are moving exactly in phase. Since the thickness of this shell is so thin, it is not surprising that one can treat two interfaces as one with a modified surface-tension coefficient $\gamma^{(1)} + \gamma^{(2)}$ for this mode (see figure 2-3b and the inset of figure 2-4a). The eigen-amplitude (defined in section 2.3.5) corresponding to this in-phase mode is $(1/2, 1/2)$, independent of $\gamma^{(1)}$ and $\gamma^{(2)}$. For the other mode, with growth rate $\sigma^-(k)$, the two interfaces are moving out of phase (see the inset of figure 2-4b). The eigen-amplitude for this out-of-phase mode is found to be $(-\gamma^{(2)}, \gamma^{(1)})/(\gamma^{(1)} + \gamma^{(2)})$, which means that the two interfaces are moving in opposite directions with amplitudes inversely proportional to their surface tensions. Due to the tiny thickness of the shell compared to its radius of curvature, this case approaches the case of a flat sheet, which is known to be always stable [33],

52

(a) In-phase mode σ^+ (b) Out-of-phase mode σ^-
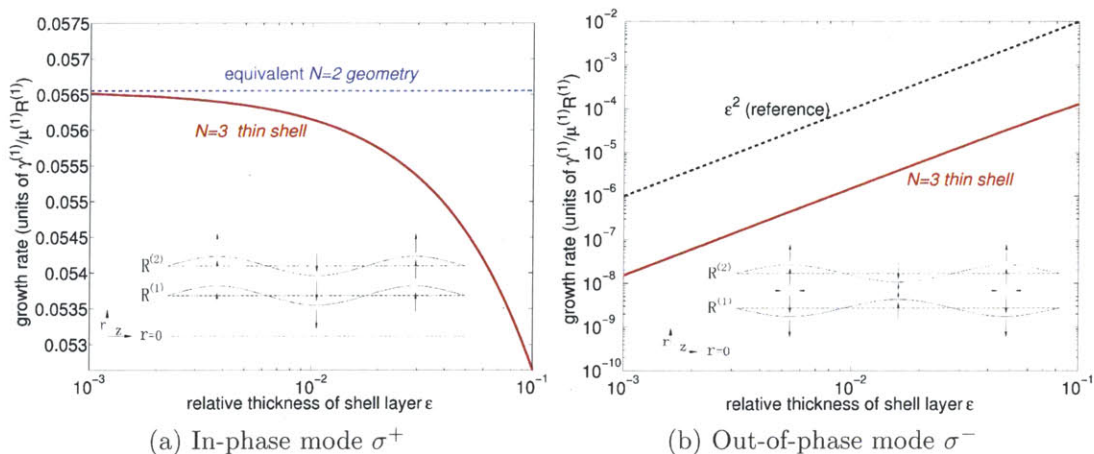
Figure 2-4: Two modes σ^+ and σ^- for thin shell layer geometry, with $R^{(1)} = 1$, $R^{(2)} = R^{(1)}(1 + \varepsilon), \gamma^{(1)} = 1, \gamma^{(2)} = 2, \mu^{(1)} = 1, \mu^{(2)} = 2, \mu^{(3)} = 3$ and $k = 0.5$. (a) illustrates that the growth rate of the in-phase mode $\sigma^+(k)$ for $N = 3$ approaches to the growth rate of $N = 2$ structure with the summed surface-tension coefficients as $\varepsilon \to 0$. (b) demonstrates that the out-of-phase growth rate $\sigma^-(k)$ decreases like ε^2 as $\varepsilon \to 0$.

as can be proved via a surface-energy argument.

A related thin-shell problem was investigated by [19] for the Navier–Stokes equations with an inviscid (gaseous) outer fluid. Those authors also found that the problem reduced to $N = 2$ instabilities (single fluid surrounded by gas) with a summed surface tension.

2.7   Effective growth rate and competing modes

In previous work on linear stability analysis, most authors identified the maximum σ with the dominant breakup process [101, 102, 117]. This exclusive emphasis on the maximum σ was continued in recent studies of $N = 3$ systems [19, 112], but here we argue that the breakup process is more complicated for $N > 2$. In a multi-layer situation, however, there is a geometric factor that complicates this comparison: not only are there different growth rates σ, but there are also different length scales $R^{(n)}$ over which breakup occurs. As a result, it is natural to instead compare a breakup time scale given by a distance ($\tilde{R}$) divided by a velocity, where $\tilde{R}$ is some average
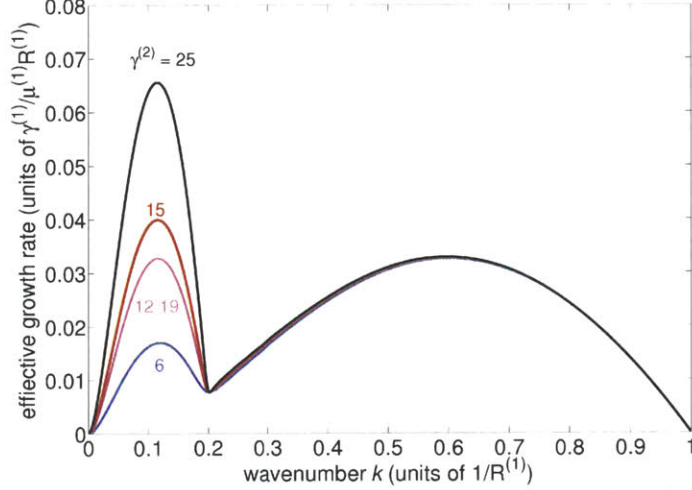
Figure 2-5: Maximum effective growth rates vs. wavenumber k. For a three-layer structure with $R^{(1)} = 1, R^{(2)} = 5, \mu^{(1)} = \mu^{(2)} = 1$, and $\gamma^{(1)} = 1$, the maximum effective growth rates $\sigma_{\text{max}}^{\text{eff}}(k)$ are plotted for several values of $\gamma^{(2)}$. For $\gamma^{(2)} = 12.19$ (magenta line), there are two equal maximum effective growth rates $\sigma_{\text{max}}^{\text{eff}}(k_1 \approx 0.58) = \sigma_{\text{max}}^{\text{eff}}(k_2 \approx 0.114)$.

radius for a given growth mode (weighted by the unit-norm eigen-amplitudes $\delta R^{(n)}$). In our case, we find that a harmonic-mean radius $\tilde{R}$ is convenient, and we define an effective growth rate ($\sim 1/\text{breakup time} \sim \text{velocity}/\tilde{R}$) by:

$$\sigma_j^{\text{eff}}(k) = \sigma_j(k) \sum_{n=1}^{N-1} \frac{\delta R_j^{(n)}}{R^{(n)}}. \tag{2.38}$$

Now, it is tempting to wonder what happens if two different wavenumbers k_1 and k_2 have the same maximum effective growth rates, a question that does not seem to have been considered in previous linear stability analysis. Let us consider a particular three-layer structure with $R^{(1)} = 1, R^{(2)} = 5, \mu^{(1)} = \mu^{(2)} = 1$, and $\gamma^{(1)} = 1$. The maximum effective growth rates $\sigma_{\text{max}}^{\text{eff}}(k) = \max_j[\sigma_j^{\text{eff}}(k)]$ vs. k are plotted in figure 2-5 for several values of $\gamma^{(2)}$. For example, at $\gamma^{(2)} = 12.19$, we find that $\sigma_{\text{max}}^{\text{eff}}(k_1 \approx 0.58) = \sigma_{\text{max}}^{\text{eff}}(k_2 \approx 0.114)$, so that there are two competing modes at very different length scales $2\pi/k_1 = 10.83$ and $2\pi/k_2 = 55.12$. In contrast, for $\gamma^{(2)} = 6$ we see that the short length-scale instability should dominate, while at $\gamma^{(2)} = 25$ the long length scale instability should dominate.

To test our predictions, we implemented a full 3-dimensional Stokes-flow numer-

(a)	(b) $\gamma^{(2)} = 6$	(c) $\gamma^{(2)} = 15$	(d) $\gamma^{(2)} = 25$
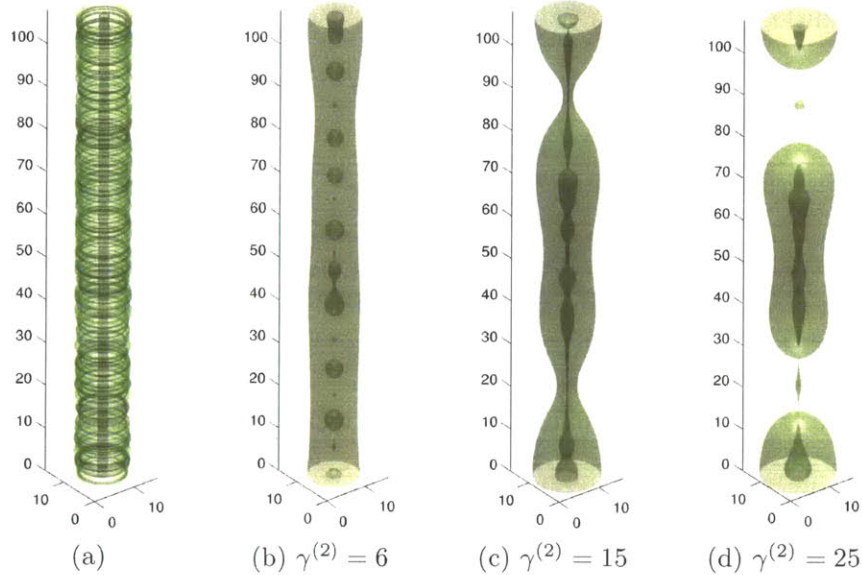
Figure 2-6: Numerical Stokes-flow simulations for three-layer systems with different $\gamma^{(2)}$. (a) Initial white-noise perturbations of the interfaces. As predicted by maximum effective growth rates, the systems with $\gamma^{(2)} = 6$ (b) and $\gamma^{(2)} = 25$ (d) exhibit breakup initially via the short- and long-scale modes, respectively (which are dominated by motion of the inner and outer cylinders, respectively). Near-simultaneous breakup occurs for $\gamma^{(2)} = 15$ (c).

ical scheme to simulate the breakup process of this cylindrical-shell system. A brief description of this hybrid scheme, a combined spectral and level-set method, is given in Section 2.10. We use initial white-noise perturbations on both interfaces $R^{(1)}$ and $R^{(2)}$ (see figure 2-6a). The computational box is $16 \times 16 \times 108$ with resolutions $160 \times 160 \times 480$ pixels. As predicted, $\gamma^{(2)} = 6$ and $\gamma^{(2)} = 25$ exhibit breakup initially via the short- and long-scale modes, respectively (which are dominated by motion of the inner and outer cylinders, respectively). It is interesting to estimate the intermediate $\gamma^{(2)}$ where the two breakup processes occur simultaneously. Linear stability analysis predicts $\gamma^{(2)} \approx 12.19$, and indeed we find numerically that near-simultaneous breakup occurs for $\gamma^{(2)} \approx 15$ (see figure 2-6c). In contrast, simply looking at $\sigma_{\max}$ rather than $\sigma_{\max}^{\text{eff}}$ would lead one to predict that simultaneous breakup occurs at $\gamma^{(2)} \approx 4.15$, in which case all three $\gamma^{(2)}$ values in figure 2-6 would have looked like figure 2-6d (large scale dominating). In the case of near-simultaneous breakup timescales, the dominant breakup process may be strongly influenced by the initial conditions (i.e., the

initial amplitudes of the modes), which offers the possibility of sensitive experimental tunability of the breakup process.

The final breakup of the fluid neck is described by a self-similar scaling theory for the case of a single fluid jet [38], and so it is interesting to examine numerically to what extent a similar description is possible for the $N = 3$ system. In particular, at the last stage of a single-cylinder breakup process, a singularity develops at the point of breakup which does not possess a characteristic scale, and hence a set of self-similar profiles can be predicted [37]. For both a viscous jet in gas [38] and a viscous thread in another viscous fluid ($N = 2$) [22, 70], these principles predict that the neck radius $h(t)$ vanishes linearly with time as $h(t)\mu/\gamma \sim (t_0 - t)$ where t_0 is the breakup time. However, there is no available scaling theory for $N \geq 3$ systems. Here, we simply use our numerical simulations above to study the rate at which the neck radius vanishes in an $N = 3$ system. For all three cases with different $\gamma^{(2)}$, the neck radius of the outer interface vanishes with time in an asymptotically linear fashion as the breakup time is approached (see figure 2-7). This is not surprising in the $\gamma^{(2)} = 6$ case where the inner surface has already broken up—the breakup of the outer surface reduces to an $N = 2$ problem when the neck becomes thin enough—and we find that $h(t)\mu/\gamma^{(2)} \approx 0.024(t_0 - t)$, in reasonable agreement with the 0.033 value predicted analytically [22] given the low spatial resolution with which we resolve the breakup singularity ($h/R^{(2)} = 0.1$ corresponds to 5 pixels). Moreover, we find that in this equal-viscosity $N = 3$ system, all three $\gamma^{(2)}$ values yield slopes of $h(t)\mu/\gamma^{(2)}$ that are within 10% of one another, indicating that the inner-surface tension $\gamma^{(1)} = 1$ has a relatively small impact on the outer-surface breakup.

2.8 Breakup analysis for each interface

In previous section, we introduce the effective growth rate (2.38) to include the geometric factor from different length scales $R^{(n)}$ over which breakup occurs. In this section, we study the breakup timescale and lengthscale for each interface. Moreover, we treat the problem more rigorously: given a statistical distribution of initial
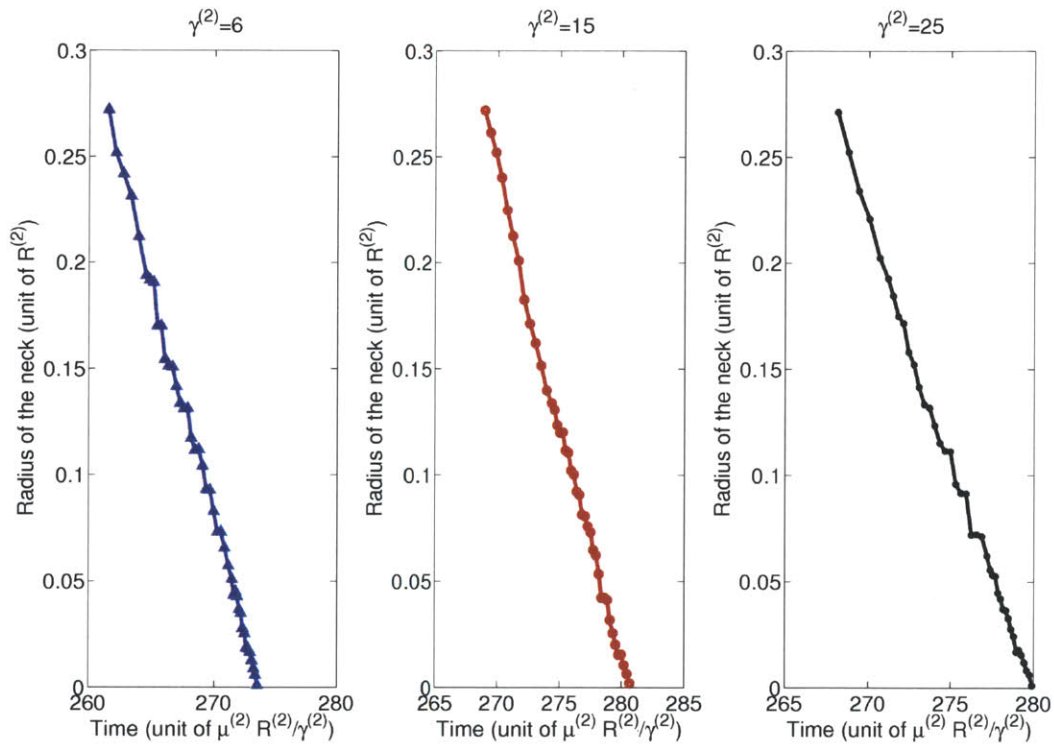
Figure 2-7: Radius of the fluid neck versus time during the final phase of the breakup of the outermost interface, from the 3-dimensional Stokes simulations of figure 2-6. This breakup is asymptotically linear with time, similar to the predictions of the scaling theory for $N = 2$ systems [22, 70].

perturbations, we determine the mean effect of each mode on each interface and the corresponding mean breakup times.

For the j-th mode with growth rate $\sigma_j(k)$ at wavelength k, the corresponding eigen-amplitudes is $\boldsymbol{\delta R}_j = (\delta R_j{}^{(1)}, \delta R_j{}^{(2)}, \cdots, \delta R_j^{(n)}, \cdots, \delta R_j{}^{(N-1)})^T$, where we normalize $\|\boldsymbol{\delta R}_j\|_1 = 1$. Any initial perturbations can be decomposed into a linear combination of eigen-amplitudes, namely $\boldsymbol{A} = \sum_{j=1}^{N-1} a_j \boldsymbol{\delta R}_j$ for some a_j. Since the whole coupled system is linear, the small initial perturbation $\boldsymbol{A}e^{ikz}$ will grow as $\sum_{j=1}^{N-1} a_j \boldsymbol{\delta R}_j e^{i[kz - \omega_j(k)t]}$.

We examine two possible hypotheses for the statistics of the initial perturbation. First, one possibility is that the perturbations of each interface are proportional to the radius of that interface, e.g. if the interfaces have some random fractional ellipticity. More precisely, we consider the case where the perturbation of the n-th $(n = 1, 2, \cdots, N-1)$ interface is $R^{(n)} X^{(n)}$, where $X^{(n)}$ are independent identical random variables. For this kind of perturbation, we can express a_j in terms of random variables, namely,

$$
\begin{bmatrix} a_1 \\ a_2 \\ \vdots \\ a_j \\ \vdots \\ a_{N-1} \end{bmatrix} = \boldsymbol{M} \begin{bmatrix} X^{(1)} \\ X^{(2)} \\ \vdots \\ X^{(n)} \\ \vdots \\ X^{(N-1)} \end{bmatrix},
\tag{2.39}
$$

where

$$
\boldsymbol{M} = (\boldsymbol{\delta R}_1, \boldsymbol{\delta R}_2, \cdots, \boldsymbol{\delta R}_j, \cdots, \boldsymbol{\delta R}_{N-1})^{-1} \begin{bmatrix} R^{(1)} & & & & & \\ & R^{(2)} & & & & \\ & & \ddots & & & \\ & & & R^{(n)} & & \\ & & & & \ddots & \\ & & & & & R^{(N-1)} \end{bmatrix}.
\tag{2.40}
$$

Another possible scenario is that of random perturbations of the same amplitude for all interfaces, independent of radius, e.g. for small-scale surface roughness. That would correspond to perturbations $X^{(n)}$ (uniform perturbations on all the interfaces), in which case $M = (\delta R_1, \delta R_2, \cdots, \delta R_j, \cdots, \delta R_{N-1})^{-1}$.

The j-th row of (2.39) implies that $a_j = \sum_n M_{jn} X^{(n)}$. Since $X^{(n)}$ are identical independent random variables with $\langle X \rangle = 0$, we have $\langle a_j^2 \rangle = \sum_n M_{jn}^2 \langle X^2 \rangle$. Without loss of generality, we assume $\langle X^2 \rangle = 1$. Therefore we have $\tilde{a}_j = \sqrt{\langle a_j^2 \rangle} = \sum_n M_{jn}^2$.

Now we can define the breakup time of n-th interface due to j-th mode at wavelength k as a distance $[R^{(n)}]$ divided by the velocity from j-th mode $[\sigma_j(k)\tilde{a}_j(k)\delta R_j^{(n)}(k)]$:

$$T_j^{(n)}(k) = \frac{R^{(n)}}{\sigma_j(k)\tilde{a}_j(k)\delta R_j^{(n)}(k)}. \tag{2.41}$$

Therefore, the breakup time of n-th interface due to perturbations at wavenumber k is

$$T^{(n)}(k) = \min_j T_j^{(n)}(k). \tag{2.42}$$

Among all the wavenumbers k, we define $k_{\max}^{(n)}$, the dominant mode for the n-th interface, as the wavenumber leading to shortest breakup time for that interface: $k_{\max}^{(n)} = \arg\min T^{(n)}(k)$. Hence, the breakup lengthscale of n-th interface is $\lambda^{(n)} = 2\pi/k_{\max}^{(n)}$, and the breakup timescale of n-th interface is

$$T^{(n)} = \min_k T^{(n)}(k) = \min_k \min_j T_j^{(n)}(k). \tag{2.43}$$

If we define the dominant mode $k_{\max}$ as the mode leading to the shortest breakup time of any one interface, and this shortest time T as the breakup time for the whole system, we have

$$T = \min_n T^{(n)} = \min_n \min_k \min_j T_j^{(n)}(k), \tag{2.44}$$

and the dominant mode $k_{\max} = \arg\min T(k)$. We checked that when $N = 2$, this definition agrees with the normal definition given in section 2.3.5. An application of this analysis to core-shell particle fabrication is discussed in section 3.3.
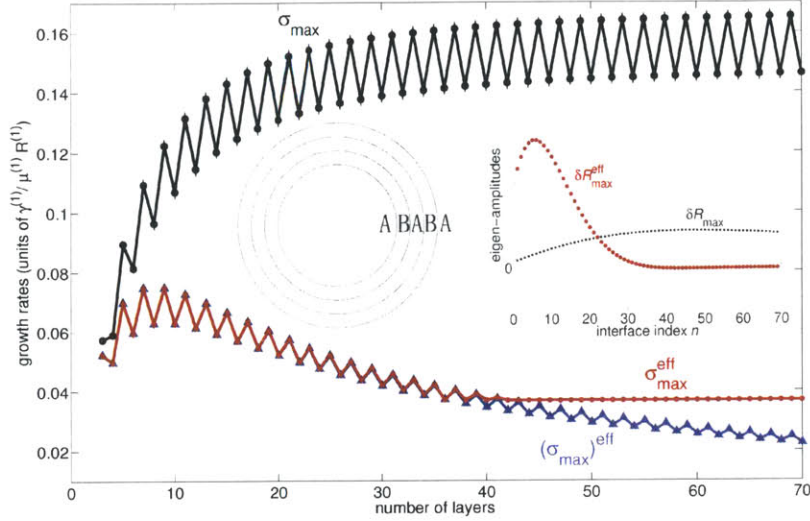
Figure 2-8: Growth rates of an $ABABAB\cdots$ alternating structure. Both σ_{max} (black line) and σ_{max}^{eff} (red line) converge to finite asymptotic values as $N \to \infty$, although in the former case the asymptotic value depends on the parity of N. The differences between σ_{max}^{eff} (red line) and $(\sigma_{max})^{eff}$ (blue line) imply that the modes corresponding to σ_{max} and σ_{max}^{eff} are not always the same. The right inset shows the eigen-amplitudes $\boldsymbol{\delta R}_{max}$ (black dots) and $\boldsymbol{\delta R}_{max}^{eff}$ (red circles) for $N = 70$, corresponding to σ_{max} and σ_{max}^{eff} respectively. The left inset depicts the structure whose parameters are $R^{(n)} = 1 + 0.2(n - 1)$, $\gamma^{(n)} = 1$, and $\mu^{(n)} = 1$ if n is odd or $\mu^{(n)} = 2$ otherwise.

2.9 N-Layer structures

Since all previous work has studied only $N = 2$ or $N = 3$, it is interesting to consider the opposite limit of $N \to \infty$. We consider two examples: a repeating structure of two alternating layers, and a structure with continuously varying viscosity, both of which are approached as $N \to \infty$. In fact, concentric-shell structures with dozens of alternating fluid layers have been used experimentally in optical fibers [46, 63]. However, the motivation of this section is primarily exploratory, rather than engineering—to begin to discover what new phenomena may arise for large N.

2.9.1 Alternating structure

First we consider an $ABABAB\cdots$ structure of two alternating, repeating layers A and B as shown schematically in the left inset of figure 2-8. We choose $\mu^{(n)} = 1$ if n is odd and $\mu^{(n)} = 2$ otherwise. The other parameters are $R^{(n)} = 1 + 0.2(n - 1)$ and

60

$\gamma^{(n)} = 1.$

For this multilayer structure, we find that both the maximum growth rate $\sigma_{\max}$ of the fastest-growing mode and equation (2.38)'s maximum effective growth rate $\sigma_{\max}^{\mathrm{eff}}$ (corresponding to the shortest breakup time scale) apparently converge to finite asymptotic values as $N \to \infty$ (figure 2-8). (We have checked that the absolute value of the slope of $\sigma_{\max}$ is monotonically decreasing for a broader range N values up to $N = 120$, and the slope is $\sim 10^{-5}$ for $N = 120$. A rigorous proof of convergence requires a more difficult analysis, however.) The oscillations in figure 2-8 are due to the varying viscosity of the ambient fluid, which depends on the parity of N. It is interesting to know whether the fastest-growing mode and the mode with maximum effective growth are identical for a given N. To see this, we plot the effective growth rate of the fastest-growing mode $(\sigma_{\max})^{\mathrm{eff}}$ vs. N and compare it with $\sigma_{\max}^{\mathrm{eff}}$ vs. N in figure 2-8. Note that $(\sigma_{\max})^{\mathrm{eff}} = \{\max_{j,k}[\sigma_j(k)]\}^{\mathrm{eff}}$ and $\sigma_{\max}^{\mathrm{eff}} = \max_{j,k}[\sigma_j^{\mathrm{eff}}(k)]$. From figure 2-8, we can see that $(\sigma_{\max})^{\mathrm{eff}}$ and $\sigma_{\max}^{\mathrm{eff}}$ are different for large N, which implies that the modes corresponding to $\sigma_{\max}$ and $\sigma_{\max}^{\mathrm{eff}}$ are not always the same.

In the right inset of figure 2-8, we plot the eigen-amplitudes $\delta R_{\max}$ and $\delta R_{\max}^{\mathrm{eff}}$ for $N = 70$, corresponding to $\sigma_{\max}$ and $\sigma_{\max}^{\mathrm{eff}}$ respectively. The mode $\sigma_{\max}$ is mostly motion of outer interfaces, while the mode $\sigma_{\max}^{\mathrm{eff}}$ is mostly motion of inner interfaces. The mostly outer-interface motion for $\sigma_{\max}$ explains why the value of $\sigma_{\max}$ oscillates depending on the ambient fluid. Physically, the association of $\sigma_{\max}^{\mathrm{eff}}$ with the inner interfaces makes sense because, in our definition (2.38) of effective breakup rate, it is easier to break up at smaller radii (a smaller distance to break up). Alternatively, if we defined "breakup distance" in terms of the *thickness* of individual layers, then $\sigma_{\max}$ would make more sense.

2.9.2 *N*-Layer structure for a continuous model

In this subsection, we build an N-layer model to approximate a three-layer structure with a continuous viscosity. The viscosity of intermediate layer μ_{mid} of this three-layer structure is continuously varying from the viscosity of inner core μ_{in} to the viscosity of ambient fluid μ_{out}. A simple example is the linearly varying μ_{mid}, namely, $\mu_{\mathrm{mid}}(r) =$
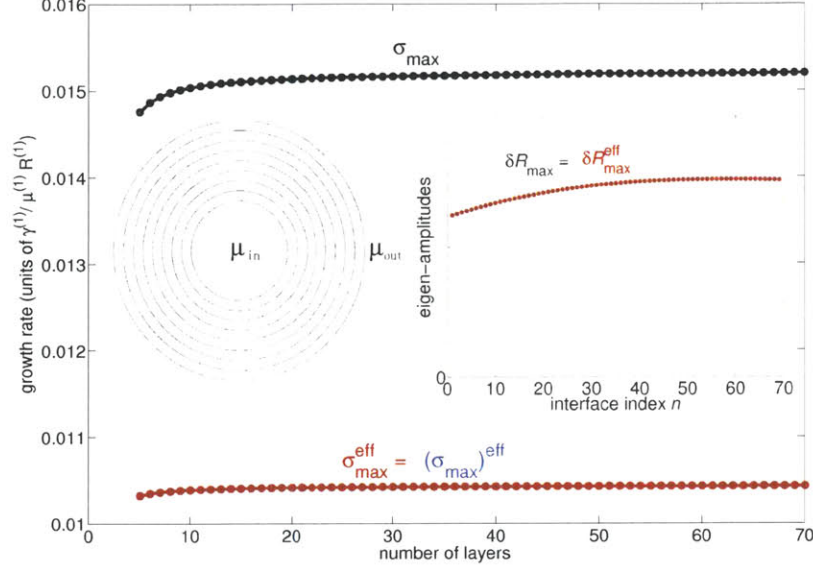
Figure 2-9: Growth rates for a continuous N-layer structure. Both $\sigma_{\max}$ and $\sigma_{\max}^{\text{eff}}$ approach constants as $N \to \infty$. The right inset plots the corresponding eigen-amplitudes $\boldsymbol{\delta R}_{\max}$ and $\boldsymbol{\delta R}_{\max}^{\text{eff}}$ (for $N=70$). The left inset sketches the N-layer structure: radius $R^{(1)} = R_{\text{in}}$, $R^{(N-1)} = R_{\text{out}}$, $R^{(n)} = R^{(1)} + \frac{R^{(N-1)}-R^{(1)}}{N-2}(n-1)$, and viscosity $\mu^{(1)} = \mu_{\text{in}}$, $\mu^{(N)} = \mu_{\text{out}}$, and $\mu^{(n)} = \mu^{(1)} + \frac{\mu^{(N)}-\mu^{(1)}}{N-1}(n-1)$, approximating a continuously and linearly varying three-layer viscosity.

$\mu_{\text{in}} + \frac{\mu_{\text{out}}-\mu_{\text{in}}}{R_{\text{out}}-R_{\text{in}}}(r - R_{\text{in}})$, where $R_{\text{in}} < r < R_{\text{out}}$. The N-layer structure (left inset of figure 2-9) with radius $R^{(1)} = R_{\text{in}}$, $R^{(N-1)} = R_{\text{out}}$, $R^{(n)} = R^{(1)} + \frac{R^{(N-1)}-R^{(1)}}{N-2}(n - 1)$, and viscosity $\mu^{(1)} = \mu_{\text{in}}$, $\mu^{(N)} = \mu_{\text{out}}$, and $\mu^{(n)} = \mu^{(1)} + \frac{\mu^{(N)}-\mu^{(1)}}{N-1}(n-1)$ approaches this continuous model for large N. In order to obtain a physically realistic continuous-viscosity model with an energy that is both finite and extensive (proportional to volume), we postulate a volume energy density η_{cont} analogous to surface energy. We approximate this by an N-layer model constructed to have the same total interfacial energy:

$$\eta_{\text{cont}} \int_{R_{\text{in}}}^{R_{\text{out}}} 2\pi r \mathrm{d}r = \sum_{n=1}^{N-1} \gamma^{(n)} 2\pi R^{(n)}, \tag{2.45}$$

where η_{cont} is an appropriate energy (per unit volume) of the inhomogeneity. Corresponding to a uniform η_{cont}, the surface-tension coefficient in this N-layer structure is same on all the interfaces: namely $\gamma^{(n)} = \gamma(N)$ for all n. From (2.45), we obtain

62

the equivalent surface tension $\gamma(N)$ in a N-layer structure

$$\gamma(N) = \frac{\eta_{\text{cont}} \int_{R_{\text{in}}}^{R_{\text{out}}} r \mathrm{d}r}{\sum_{n=1}^{N-1} \left[R_{\text{in}} + \frac{R_{\text{out}} - R_{\text{in}}}{N-2}(n-1) \right]} = O\left(\frac{1}{N}\right). \qquad (2.46)$$

With the parameters described above, we compute the maximum growth rate σ_{max} and the maximum effective growth rate $\sigma_{\text{max}}^{\text{eff}}$ for this N-layer structure. As shown in figure 2-9, both σ_{max} and $\sigma_{\text{max}}^{\text{eff}}$ approach constants as $N \to \infty$, which should be the corresponding growth rates of the continuous three-layer model. In this example, $\sigma_{\text{max}}^{\text{eff}}$ and $(\sigma_{\text{max}})^{\text{eff}}$ are the same for all N. The corresponding eigen-amplitudes δR_{max} and $\delta R_{\text{max}}^{\text{eff}}$ (for N=70) are plotted in the right inset of figure 2-9.

2.10 Full 3-dimensional Stokes-flow numerical simulation scheme for coupled cylindrical-shell system

In this section, we briefly present the numerical scheme that we used in § 2.7 to simulate the instabilities of coupled cylindrical-shell systems. We adopt a 3-dimensional Cartesian level-set approach. We use a separate level-set function $\phi^{(n)}$ to denote each interface, and generalize the formulation of [18] to N fluids by using $N - 1$ level-set functions governed by the following equations:

$$-\nabla p + \nabla \cdot \left[\mu(\nabla U + \nabla U^{\text{T}})\right] = \sum_{n=1}^{N-1} \gamma^{(n)} \delta(\phi^{(n)}) \kappa(\phi^{(n)}) \frac{\nabla \phi^{(n)}}{|\nabla \phi^{(n)}|}, \qquad (2.47)$$

and

$$\frac{\partial \phi^{(n)}}{\partial t} + U \cdot \nabla \phi^{(n)} = 0, \qquad (2.48)$$

where U is velocity, p is pressure, $\phi^{(n)} = 0$ denotes the interface between the n-th and $(n + 1)$-th layers, $\gamma^{(n)}$ is the surface-tension coefficient of the n-th interface, $\delta(\cdot)$ is a Dirac delta function, κ is curvature, and μ is viscosity.

The viscosity μ, now defined in the whole coupled system, is

$$\mu(\boldsymbol{x}) = \mu^{(1)} + \sum_{n=1}^{N-1} (\mu^{(n+1)} - \mu^{(n)}) H(\phi^{(n)}(\boldsymbol{x})), \qquad (2.49)$$

where $H(\cdot)$ is the Heaviside step function. The curvature $\kappa(\phi^{(n)})$ can be computed directly by $\kappa(\phi^{(n)}) = \boldsymbol{\nabla} \cdot \frac{\boldsymbol{\nabla}\phi^{(n)}}{|\boldsymbol{\nabla}\phi^{(n)}|}$, since $\frac{\boldsymbol{\nabla}\phi^{(n)}}{|\boldsymbol{\nabla}\phi^{(n)}|}$ is the unit outward normal vector of the n-th interface.

Given the level-set function $\phi^{(n)}(\boldsymbol{x}, t)$ at time t, we first solve the steady Stokes equations (2.47) to obtain the velocity $\boldsymbol{U}(\boldsymbol{x}, t)$. With the known velocity $\boldsymbol{U}(\boldsymbol{x}, t)$ at time t, the level-set function $\phi^{(n)}(\boldsymbol{x}, t + \Delta t)$ can be obtained by solving the convection equation (2.48).

In our implementation, the computation cell is a box with dimensions $a \times a \times \ell$ in Cartesian coordinates, with periodic boundary conditions. We choose a and ℓ large enough such that the periodicity does not substantially affect the breakup process. We solve equations (2.47) by a spectral method: we represent $\boldsymbol{U}$ and p by Fourier series (discrete Fourier transforms). For the constant μ case of § 2.7, (2.47) is diagonal in Fourier space and can be solved in one step by fast Fourier transforms (FFTs). More generally, for variable viscosity, we find that an iterative solver such as GMRES or BiCGSTAB [11] converges in a few iterations with a constant μ preconditioner (i.e., block Jacobi) using the average μ. The level-set functions are described on the same grid, but using finite differences [WENO [72] in space, RK3-TVD [108] in time]. The $\delta(\cdot)$ function is smoothed over 3 pixels with a raised-cosine shape [93]. We use the reinitialization scheme of [114] to preserve the signed distance-function property $|\boldsymbol{\nabla}\phi^{(n)}| = 1$ of $\phi^{(n)}$ after each time step.

Our simulation code is validated against a well-studied case: the evolution of a 2-dimensional elliptical blob [23, 24, 49, 61, 116]. It is known that the plane Stokes flow, initially bounded by a simple smooth closed elliptic curve, will eventually become circular under the effect of surface tension. [23] illustrated that the evolution via a series of ellipse shapes is remarkably good approximation to the dynamics of a sintering ellipse [even though [49] showed that the exact evolution shapes are not
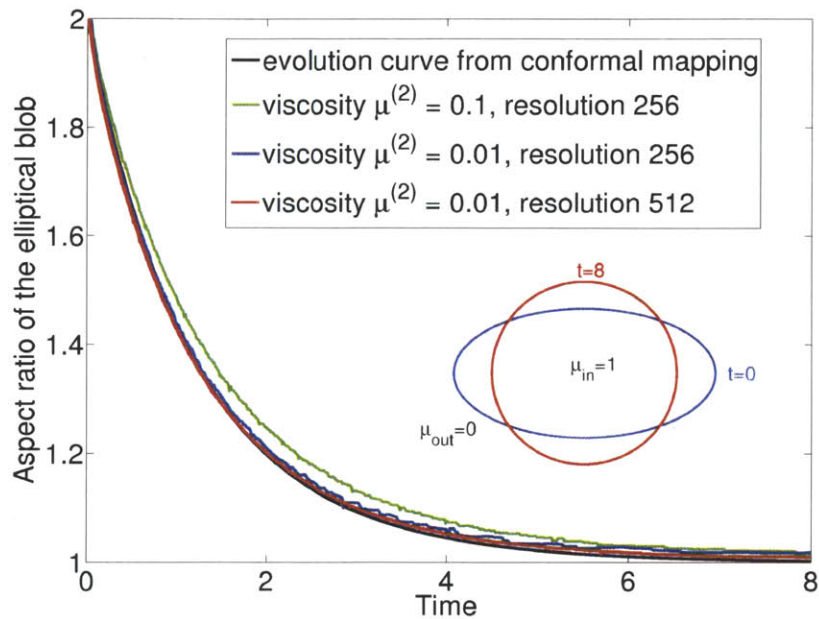
Figure 2-10: The aspect ratio of a 2-dimensional elliptical blob vs. time, obtained by different methods and implementations. For the system initially bounded by $x^2/4 + y^2 = 1$, with the elliptical blob viscosity $\mu_{\text{in}} = 1$, the ambient fluid viscosity $\mu_{\text{out}} = 0$ and the surface tension $\gamma = 1$, [15] used the conformal mapping method via finite element implementation, obtaining the black evolution curve. The evolution curves (green, blue and red) given by our simulations converge to the black curve with the increasing resolutions and as the ambient viscosity $\mu^{(2)}$ goes to zero.

strictly elliptical]. Suppose the plane Stokes flow is bounded by the ellipse $x^2/4 + y^2 = 1$ at $t = 0$. The viscosity of the elliptical blob $\mu_{\text{in}} = 1$, the viscosity of ambient fluid $\mu_{\text{out}} = 0$, and the surface tension $\gamma = 1$. [15] implemented the conformal mapping method [23, 24, 116] and computed the evolution of the boundaries. The aspect ratio (the major axis over the minor axis) of the ellipses vs. time is plotted (the black curve) in figure 2-10. Since our simulation code only works for non-zero $\mu^{(n)}$, the evolution under $\mu^{(1)} = 1$ and $\mu^{(2)} \to 0$ is expected to converge to the black evolution curve obtained by the conformal mapping. In figure 2-10, we also plotted the evolution curves from our method with $\mu^{(2)} = 0.1$ and resolution 256×256 (the green curve), $\mu^{(2)} = 0.01$ and resolution 256×256 (the blue curve), and $\mu^{(2)} = 0.01$ and resolution 512×512 (the red curve). With high resolutions and small $\mu^{(2)}$, the evolution curves obtained by our simulation codes converge to the one given by a different method with an independent implementation.

2.11 Linear stability analysis for concentric fluid shells governed by the full Navier–Stokes equations

In this section, we extended our linear stability analysis to concentric cylindrical fluid-shells governed by the full Navier–Stokes equations. Let $\rho^{(n)}$ and $\mu^{(n)}$ denote the density and viscosity of the n-th fluid. $u_r^{(n)}(z)$ is the radial component of the velocity and $u_z^{(n)}(z)$ is the axial component of the velocity. Following a linear stability analysis similar to §2.3.2, we find that the pressure $p^{(n)}(z)$ in the n-th fluid still satisfies Laplace's equation (2.12). Therefore, the perturbed pressure still satisfies the modified Bessel equation (2.13) and the solution in (2.14) is still valid. The velocity is obtained by solving the linearized Navier–Stokes equations

$$-\rho^{(n)}\frac{\partial u_r^{(n)}}{\partial t} + \mu^{(n)}\left(\frac{\partial^2 u_r^{(n)}}{\partial r^2} + \frac{1}{r}\frac{\partial u_r^{(n)}}{\partial r} - \frac{u_r^{(n)}}{r^2} + \frac{\partial^2 u_r^{(n)}}{\partial z^2}\right) = \frac{\partial p^{(n)}}{\partial r} \qquad (2.50)$$

and

$$-\rho^{(n)}\frac{\partial u_z^{(n)}}{\partial t} + \mu^{(n)}\left(\frac{\partial^2 u_z^{(n)}}{\partial r^2} + \frac{1}{r}\frac{\partial u_z^{(n)}}{\partial r} + \frac{\partial^2 u_z^{(n)}}{\partial z^2}\right) = \frac{\partial p^{(n)}}{\partial z}. \tag{2.51}$$

Note that the nonlinear convection terms do not appear in the linearized equations (2.50) and (2.51) because the basic steady state [(2.8)–(2.9)] is at rest. Substituting the perturbed pressure (2.14) into equations (2.50)–(2.51), we find that the radial component of the perturbed velocity in (2.15) is replaced by

$$\delta u_r^{(n)}(r) = c_1^{(n)}\frac{K_1(kr) - K_1(k^{(n)}r)}{-\mathrm{i}\omega\rho^{(n)}/k} - c_2^{(n)}\frac{I_1(kr) - I_1(k^{(n)}r)}{-\mathrm{i}\omega\rho^{(n)}/k}$$
$$+ c_3^{(n)}\frac{K_1(k^{(n)}r)}{2\mu^{(n)}k} + c_4^{(n)}\frac{I_1(k^{(n)}r)}{2\mu^{(n)}k} \tag{2.52}$$

and the axial component of the perturbed velocity in (2.16) now becomes

$$\delta u_z^{(n)}(r) = c_1^{(n)}\frac{K_0(kr) - \lambda^{(n)}K_0(k^{(n)}r)}{\rho^{(n)}\omega/k} + c_2^{(n)}\frac{I_0(kr) - \lambda^{(n)}I_0(k^{(n)}r)}{\rho^{(n)}\omega/k}$$
$$- c_3^{(n)}\frac{\mathrm{i}\lambda^{(n)}K_0(k^{(n)}r)}{2\mu^{(n)}k} + c_4^{(n)}\frac{\mathrm{i}\lambda^{(n)}I_0(k^{(n)}r)}{2\mu^{(n)}k}, \tag{2.53}$$

where

$$\lambda^{(n)} = \sqrt{1 + \frac{-\mathrm{i}\omega\rho^{(n)}}{\mu^{(n)}k^2}} \qquad \text{and} \qquad k^{(n)} = \lambda^{(n)}k. \tag{2.54}$$

After matching boundary conditions [(2.19), (2.21), (2.24) and (2.26)], we can obtain the dispersion relation by solving the same determinant equation (2.32), except that $\mathsf{A}^{(n,n')}$ and $\mathsf{B}^{(n)}$ from (2.28) and (2.29) are replaced by

$$\mathsf{A}_{\mathrm{ns}}^{(n,n')} =$$

$$\begin{bmatrix} \dfrac{K_1^{(n)} - K_1[k^{(n')}R^{(n)}]}{\rho^{(n')}/2k^2} & -\dfrac{I_1^{(n)} - I_1[k^{(n')}R^{(n)}]}{\rho^{(n')}/2k^2} & \dfrac{K_1[k^{(n')}R^{(n)}]}{\mu^{(n')}} & \dfrac{I_1[k^{(n')}R^{(n)}]}{\mu^{(n')}} \\ \dfrac{K_0^{(n)} - \lambda^{(n')}K_0[k^{(n')}R^{(n)}]}{-\rho^{(n')}/2k^2} & \dfrac{I_0^{(n)} - \lambda^{(n')}I_0[k^{(n')}R^{(n)}]}{-\rho^{(n')}/2k^2} & \dfrac{\lambda^{(n')}K_0[k^{(n')}R^{(n)}]}{-\mu^{(n')}} & \dfrac{\lambda^{(n')}I_0[k^{(n')}R^{(n)}]}{\mu^{(n')}} \\ \dfrac{K_1^{(n)} - \alpha^{(n')}K_1[k^{(n')}R^{(n)}]}{\rho^{(n')}/2\mu^{(n')}k^2} & \dfrac{I_1^{(n)} - \alpha^{(n')}I_1[k^{(n')}R^{(n)}]}{-\rho^{(n')}/2\mu^{(n')}k^2} & \alpha^{(n')}K_1[k^{(n')}R^{(n)}] & \alpha^{(n')}I_1[k^{(n')}R^{(n)}] \\ \triangle_1 & \triangle_2 & \triangle_3 & \triangle_4 \end{bmatrix}, \tag{2.55}$$

where

$$\alpha^{(n')} = 1 + \frac{-\mathrm{i}\omega\rho^{(n')}}{2\mu^{(n')}k^2} \tag{2.56}$$

67

$$\triangle_1 = \frac{\alpha^{(n')}K_0^{(n)} + K_1^{(n)}/kR^{(n)}}{\rho^{(n')}/2\mu^{(n')}k^2} - \frac{\lambda^{(n')}K_0[k^{(n')}R^{(n)}] + K_1[k^{(n')}R^{(n)}]/kR^{(n)}}{\rho^{(n')}/2\mu^{(n')}k^2} \qquad (2.57)$$

$$\triangle_2 = \frac{\alpha^{(n')}I_0^{(n)} - I_1^{(n)}/kR^{(n)}}{\rho^{(n')}/2\mu^{(n')}k^2} + \frac{-\lambda^{(n')}I_0[k^{(n')}R^{(n)}] + I_1[k^{(n')}R^{(n)}]/kR^{(n)}}{\rho^{(n')}/2\mu^{(n')}k^2} \qquad (2.58)$$

$$\triangle_3 = \lambda^{(n')}K_0[k^{(n')}R^{(n)}] + K_1[k^{(n')}R^{(n)}]/kR^{(n)} \qquad (2.59)$$

$$\triangle_4 = -\lambda^{(n')}I_0[k^{(n')}R^{(n)}] + I_1[k^{(n')}R^{(n)}]/kR^{(n)} \qquad (2.60)$$

and

$$\mathsf{B}_{\mathrm{ns}}^{(n)} = \frac{-\gamma^{(n)}k\left[1 - \frac{1}{(kR^{(n)})^2}\right]}{2}$$
$$\times \begin{bmatrix} 0 & 0 & 0 & 0 \\ 0 & 0 & 0 & 0 \\ 0 & 0 & 0 & 0 \\ \frac{K_1^{(n)} - K_1[k^{(n)}R^{(n)}]}{\rho^{(n)}/2k^2} & -\frac{I_1^{(n)} - I_1[k^{(n)}R^{(n)}]}{\rho^{(n)}/2k^2} & \frac{K_1[k^{(n)}R^{(n)}]}{\mu^{(n)}} & \frac{I_1[k^{(n)}R^{(n)}]}{\mu^{(n)}} \end{bmatrix}. \qquad (2.61)$$

Note that, because of the ω in $\lambda^{(n)}$ and $k^{(n)}$, the matrix $\mathsf{M}^{(N)}$ becomes nonlinear in ω (or $1/\omega$), and can no longer be reduced to a generalized eigenproblem. Instead, one must solve the nonlinear eigenproblem $\mathsf{M}_2^{(N)}(k,\omega)\boldsymbol{\xi} = i\omega\mathsf{M}_1^{(N)}(k,\omega)\boldsymbol{\xi}$. Numerous methods have been developed for such problems [7, 43, 67, 105, 121].

The formulas (2.28) and (2.29) of $\mathsf{A}^{(n,n')}$ and $\mathsf{B}^{(n)}$ for Stokes flow can be obtained directly from the formulas (2.55) and (2.61) of $\mathsf{A}_{\mathrm{ns}}^{(n,n')}$ and $\mathsf{B}_{\mathrm{ns}}^{(n)}$ for general flow by taking the limit $\rho^{(n)} \to 0$. As mentioned in § 2.5.1, the most straightforward formulation of the Navier–Stokes matrices yields dependent columns when $\rho \to 0$. Here, we have chosen an appropriate linear combination of columns to avoid this difficulty, which is equivalent to the procedure suggested by [117].

However, the corresponding formulas for inviscid fluids cannot be obtained by simply taking the limit $\mu^{(n)} \to 0$. For any small but nonzero $\mu^{(n)}$, the current formulation takes into account the boundary-layer effects [12] by imposing a no-slip condition. For inviscid flows, we cannot assume that the axial velocities are continuous across the interfaces, since no-slip boundary conditions are not applied. Whenever the no-slip

boundary condition is not applied, one has an additional degree of freedom, the equilibrium-state velocities $\bar{u}_z^{(n)}$ of the layers. This is easily incorporated, because it merely converts several ω expressions to $\omega - \bar{u}_z^{(n)}k$. This happens in two places. First, the velocity adds an additional inertial term $-\rho^{(n)}\bar{u}_z^{(n)}\frac{\partial u_r^{(n)}}{\partial z}$ to the left side of (2.50) and $-\rho^{(n)}\bar{u}_z^{(n)}\frac{\partial u_z^{(n)}}{\partial z}$ to the left side of (2.51). Second, it adds a new first-order term to equation (2.18) for continuity of normal velocity, since there is a term from $\bar{u}_z^{(n)}$ multiplied by the $\delta R^{(n)}$ in the numerator of (A.1) for the normal vector. These terms change ω to $\omega - \bar{u}_z^{(n)}k$ in (2.54) for $\lambda^{(n)}$ and to $\omega - \bar{u}_z^{(n')}k$ in (2.56) for $\alpha^{(n')}$, and they also multiply every $\mathsf{B}_{\mathrm{ns}}^{(n)}$ matrix (including $\tilde{\mathsf{B}}_{\mathrm{ns}}^{(1)}$) by $\omega/(\omega - \bar{u}_z^{(n)}k)$ [canceling the $1/\omega$ factor multiplying $\mathsf{M}_2^{(N)}$ in (2.31)]; the $\mathsf{A}_{\mathrm{ns}}^{(n,n')}$ and $\mathsf{B}_{\mathrm{ns}}^{(n)}$ matrices are otherwise unchanged, since $\bar{u}_z^{(n)}$ must be equal for adjacent viscous layers. If the n-th fluid is inviscid while the $(n-1)$-th and/or $(n+1)$-th fluids are viscous, then $\mathsf{A}_{\mathrm{ns}}^{(n-1,n-1)}$ and $\mathsf{B}_{\mathrm{ns}}^{(n-1)}$, and/or $\mathsf{A}_{\mathrm{ns}}^{(n,n+1)}$, respectively, become 3×4 matrices that can be obtained from (2.55) and (2.61) by eliminating the second row (corresponding to continuity of the tangential component of the velocity). If the n-th layer is inviscid, regardless of the adjacent layers, $\mathsf{A}_{\mathrm{invsd}}^{(n',n)}$ and $\mathsf{B}_{\mathrm{invsd}}^{(n)}$ are 3×2 matrices: not only has continuity of the tangential component of the velocity disappeared, but also the $\partial/\partial r$ derivatives of the velocities in the momentum equations (2.50) and (2.51) disappear when $\mu^{(n)} = 0$, eliminating the $c_{\{3,4\}}^{(n)}$ degrees of freedom. (This eliminates the need for the linear combinations of columns mentioned above, further simplifying these matrices.) More explicitly, the $\mathsf{A}_{\mathrm{invsd}}^{(n',n)}$ and $\mathsf{B}_{\mathrm{invsd}}^{(n)}$ matrices for an inviscid n-th layer are obtained by matching the boundary conditions (2.18), (2.24), and (2.26), giving

$$
\mathsf{A}_{\mathrm{invsd}}^{(n',n)} = \begin{bmatrix} \frac{\omega - \bar{u}_z^{(n')}k}{\omega - \bar{u}_z^{(n)}k}\frac{K_1^{(n')}}{\rho^{(n)}/2k^2} & -\frac{\omega - \bar{u}_z^{(n')}k}{\omega - \bar{u}_z^{(n)}k}\frac{I_1^{(n')}}{\rho^{(n)}/2k^2} \\ 0 & 0 \\ -\mathrm{i}(\omega - \bar{u}_z^{(n)}k)K_0^{(n')} & -\mathrm{i}(\omega - \bar{u}_z^{(n)}k)I_0^{(n')} \end{bmatrix}
\tag{2.62}
$$

$$
\mathsf{B}_{\mathrm{invsd}}^{(n)} = \frac{\omega}{\omega - \bar{u}_z^{(n)}k}\frac{-\gamma^{(n)}k\left[1 - \frac{1}{(kR^{(n)})^2}\right]}{2} \begin{bmatrix} 0 & 0 \\ 0 & 0 \\ \frac{K_1^{(n)}}{\rho^{(n)}/2k^2} & -\frac{I_1^{(n)}}{\rho^{(n)}/2k^2} \end{bmatrix}.
\tag{2.63}
$$

69

For the special case $\bar{u}_z^{(n)} = 0$ (at-rest steady state), the above formulas are equivalent to the ones obtained by eliminating the second row, eliminating the third and fourth columns, then taking the limit $\mu^{(n)} \to 0$ in the general formulas (2.55) and (2.61). More precisely, for the viscosity term in (2.50) and (2.51) to be negligible, one must have $\mu^{(n)} \ll \omega\rho^{(n)}/k^2$. (Note that this is length- and time-scale dependent, so the validity of neglecting viscosity terms depends on the ω and k of the dominant growth mode.) It is also interesting to consider a Galilean transformation in which a constant $\bar{v}_z$ is added to $\bar{u}_z^{(n)}$ for all n, which cannot change the physical results. Here, because all ω factors are accompanied by $-\bar{u}_z^{(n)}k$, it is clear that such a transformation merely shifts all of the mode frequencies $\omega_j(k)$ by $\bar{v}_z k$, which does not change the growth rates (the imaginary part), while the shift in the real frequency is simply due to the frequency-k spatial oscillations moving past any fixed z at velocity $\bar{v}_z$.

As a validation check, we find that our formulation gives the same dispersion relations for various Navier–Stokes cases discussed in the previous literature: e.g., a single inviscid jet in air (ignoring the air density and viscosity) [101], a single viscous jet in air (ignoring the air density and viscosity) [102], a single viscous jet with high velocity in air (considering the air density but ignoring the viscosity) [111] and a compound jet in air (ignoring the air density and viscosity) [19].

2.12 Azimuthal instability revisited: a 2d thin film approach

In this section, we revisit the azimuthal stability/instability. In section 2.2, we showed that surface tension can only drive axisymmetric instabilities. In other words, the surface tension alone can only lead to axial, not azimuthal, breakup. However, in recent experiments [29], it was found that when the shells' thicknesses are in nanometer scales (more precisely, sub-100 nm Se layer in Se/PSU combination and 3 nm As_2Se_3 layer in As_2Se_3/PES combination), the thin shells break up in the azimuthal direction. Our previous analysis implies that this instability must stem from the rapid

70

taper of the fiber radius from centimeters to millimeters (the drawn-down "neck"), or some other physical influence (e.g., elastic effects, thermal gradients, or long-range van der Waals interaction). As a first study, we focus on the effects of van der Waals interaction. Since the shell thickness (nanometers) is much smaller than the fiber diameter (millimeters), the curvature effect due to the fiber radius is negligible, and we can treat this instability problem as a 2d thin film problem.

2.12.1 Linear stability analysis for 2d thin film under van der Waals interactions
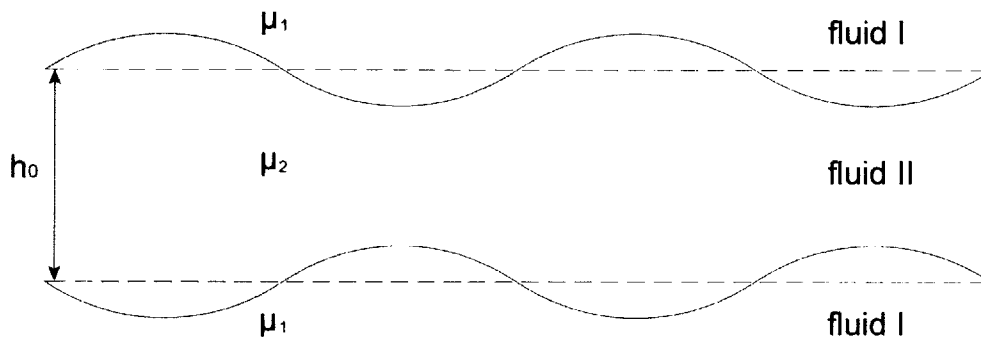
Figure 2-11: Sketch of 2d thin film with small perturbations.

In this section, we study the stability of a thin film with height h_0 embedded in two semi-infinite fluids (sketched in figure 2-11) under the effects of surface tension and van der Waals forces. Since both the top and bottom fluids in experiments are the same polymer in viscous state [29], we choose same fluid properties (viscosities $\mu^{(1)}$ and surface tension γ) for both top and bottom fluids.

Many researchers had looked at the thin film breakups due to van der Waals forces. References [104, 122] analyzed a thin film on a substrate (top layer air and bottom layer solid) for long wavelength mode ($kh_0 \ll 1$) with lubrication theory, Ref. [104, 124] studied the thin free liquid film problems (both top and bottom layers are air), and Ref. [76, 77, 123] analyzed the three-fluid layer problem with linear stability analysis staring from the full Navier–Stokes equations. Reference [14] presented

the overview of wetting/dewetting phenomena and Ref. [92] reviewed the long-scale evolution of thin liquid film.

Although the results from Ref. [77] applied to our problem, we found that the linear stability analysis staring from the Stokes formulation, instead of the full Navier–Stokes equations, makes the analysis more convenient and easier, since the real problem we are interested in is in the Stokes regime. By using approaches similar to those we presented in section 2.3, namely solving the linearized equations in each fluid layer and matching four boundary conditions at the interfaces, we obtain the growth rate $\sigma(k)$:

$$\sigma(k) = -\frac{\gamma_{\text{eff}}k}{2}\frac{\mu_2(\cosh(kh_0) - 1) + \mu_1(\sinh(kh_0) - kh_0)}{\mu_2^2(\sinh(kh_0) + kh_0) + 2\mu_1\mu_2\cosh(kh_0) + \mu_1^2(\sinh(kh_0) - kh_0)}. \quad (2.64)$$

Here γ_{eff} is the effective surface tension: the effects of both surface tension and van der Waals interactions

$$\gamma_{\text{eff}} = \gamma + \frac{2}{k^2}\frac{\mathrm{d}^2 G}{\mathrm{d}h^2}\Big|_{h=h_0}, \quad (2.65)$$

where γ is the regular surface tension between two fluids and $G(h)$ is the van der Waals potential energy per unit area as a function of spacing h. A typical representation for $G(h)$ is in terms of the Hamaker constant A [51], namely

$$G(h) = -\frac{A}{12\pi h^2}. \quad (2.66)$$

This is accurate in the limit of sufficiently small h, whereas for large h the energy will go as $1/h^3$ and is called a Casimir energy [16]. More generally, the full $G(h)$ in both regimes can be computed (in the "proximity force approximation" [31], which neglects the curvature of the surface and is valid when the radius of curvature is much greater h) using the Lifshitz formula for the Casimir interaction between two planar semi-infinite dielectric materials, assuming the absorption spectrum of the materials is known over a wide enough bandwidth [35, 84].

For a mode with wavenumber k or wavelength $\lambda = 2\pi/k$, it will grow if $\sigma(k) > 0$. Therefore, the critical wavenumber k_c and critical wavelength λ_c can be determined

by

$$\sigma(k_c) = 0 \implies k_c = \sqrt{-\frac{2}{\gamma}\frac{\mathrm{d}^2 G}{\mathrm{d}h^2}} \qquad \text{and} \qquad \lambda_c = 2\pi\sqrt{-\frac{\gamma}{2}\left(\frac{\mathrm{d}^2 G}{\mathrm{d}h^2}\right)^{-1}}. \qquad (2.67)$$

Note that this critical wavelength can also be determined from a simple energy comparison argument: for a small sinusoidal perturbation with wave number k to grow, the total sum of surface energy and van der Waals potential energy must be decreasing, which will give exactly the same k_c and λ_c.

To obtain the fastest growth mode $k_{\max}$ (or $\lambda_{\max}$) that maximizes the growth rate $\sigma(k)$ given in (2.64) , we need to solve this optimization problem numerically. Under the assumptions that $kh_0 \ll \mu_1/\mu_2$ and $kh_0 \ll \mu_2/\mu_1$, Ref. [77, 123] showed that

$$\sigma(k) \approx -\frac{\gamma_{\text{eff}} k^3 h_0^2}{8\mu_1}, \qquad k_{\max} \approx \frac{k_c}{\sqrt{3}} \qquad \text{and} \qquad \sigma_{\max} = \frac{h_0^2}{6\mu_1}\sqrt{\frac{2}{3\gamma}}\left(-\frac{\mathrm{d}^2 G}{\mathrm{d}h^2}\right)^{3/2}. \tag{2.68}$$

When the viscosity ratio μ_1/μ_2 is not of order one (for example, the ratio is around 10^5 in the PSU/Se case), these assumptions are not valid and the fastest mode must be found numerically. We will demonstrate such a case in the following section.

2.12.2 Comparison with azimuthal breakup experiments

In Ref. [29], it was observed that As_2Se_3 layer (in pair with PES) breaks up around 5 nm (between 3 nm and 14 nm), and Se layer (in pair with PSU) breaks up around 100 nm (between 96 nm and 700 nm). The typical fiber drawing time in these experiments are around 120 seconds. The goal of this section is to predict these threshold thicknesses and understand the mechanism for the threshold difference (5 nm versus 100 nm) in these two configurations.

In the following calculations, we use $\gamma = 0.1$ N/m, the viscosity of polymers 10^5 Pa $\cdot$ s, the viscosity of As_2Se_3 10^5 Pa $\cdot$ s, and viscosity of Se 1 Pa $\cdot$ s. The typical range of the Hamaker constant A is $[0.4, 4] \times 10^{-19}$ J [51].

As mentioned above, a more general expression for the long-range interaction is the Lifshitz formula [35, 84], which gives both the Hamaker expression for small h

73

and the Casimir interaction for large h. Evaluation of the Lifshitz formula requires the complete dispersion relation $\varepsilon(\omega)$ for the materials used. (Technically, it requires ε along the imaginary-ω axis, which can be determined from $\text{Im}[\varepsilon]$ along the real-ω axis, which is the absorption spectrum.) Unfortunately, we do not currently have the absorption spectrum of the materials used in these experiments over a broad enough spectrum to apply the Lifshitz formula accurately. As a simple approximation, however, we can neglect material dispersion and suppose that the materials have frequency-independent refractive indices of 1.6 for the polymer and 2.2–3.5 for the glass. For nondispersive materials, the Lifshitz expression simplifies to a Casimir energy of the form:

$$G(h) = -\frac{C_3}{3}\frac{\hbar c}{h^3}, \tag{2.69}$$

where $\hbar$ is Planck constant, c is the speed of light, and C_3 is a dimensionless number. For these refractive indices (1.6 for polymer and 3.5 for glass), the dimensionless constant C_3 is around 0.002.

In the experiments, a thin, circular semiconductor shell is embedded in the polymer with shell diameter 0.5 mm. Since this diameter is so much larger than the thickness h, we can consider it to be a flat film but with finite length $L = \pi \times 0.5 = 1.57\,\text{mm}$ (with periodic boundaries). Therefore, the critical wavelength λ_{c} should be smaller than the length of the thin film L, which implies that

$$\lambda_{\text{c}} = 2\pi\sqrt{-\frac{\gamma}{2}\left(\frac{\text{d}^2 G}{\text{d}h^2}\right)^{-1}} < L \quad \Longrightarrow h_0 \approx \begin{cases} 300\text{--}500\,\text{nm}, & \text{Hamaker theory eq. 2.66} \\ 200\,\text{nm}, & \text{Casimir theory eq 2.69.} \end{cases} \tag{2.70}$$

Note that in these two different combinations PES/As$_2$Se$_3$ and PSU/Se, the viscosities of the polymers PES and PSU are roughly the same, while the viscosity of Se is five orders of magnitude smaller than that of As$_2$Se$_3$. In order to understand the effect of this viscosity contrast, we choose three different film thicknesses, say $h_0 = 5, 10, 25$ nm, and compute the breakup times $\tau(\lambda) = 1/\sigma(\lambda)$ for these two combinations with both Hamaker theory and Casimir theory. From figure 2-12, we can see that both As$_2$Se$_3$ (red curve) and Se (blue curve) layer with thickness $h_0 = 5$ nm can

break up within the typical fiber drawing time 120 seconds (black curve). However, the breakup time for the Se layer is three orders of magnitude smaller than that of the As_2Se_3 layer, which is purely from the viscosity difference (low viscosity of Se 1 Pa·s and high viscosity of As_2Se_3 10^5 Pa·s). When the glass layer thickness is increased to 10 nm, the shortest breakup time for Se is still below the threshold, while this is not the case for As_2Se_3 layer (figure 2-13). If the layer thickness is increased further to 25 nm, even the Se layer can barely breakup during the typical drawing time (figure 2-14). From these calculations, our model implies that within the drawing time 120 seconds, the threshold thickness for azimuthal breakup is 5nm for As_2Se_3 and 25nm for Se. Comparing with experimental data, this prediction agrees with As_2Se_3 case and within a factor of 4 for the Se case. To improve this model, one may need to consider the dispersion of the material (refractive index as a function frequency), viscoelasticity, the rapid taper of the fiber, as well as the dynamics beyond the linear regime.

breakup time vs. wavelength for film thickness h_b = 5nm

PES/As_2Se_3 (μ_1/μ_2 = 1); Hamaker approach
PES/As_2Se_3 (μ_1/μ_2 = 1); Casimir apparoach
PSU/Se (μ_1/μ_2 = 1e+5); Hamaker approach
PSU/Se (μ_1/μ_2 = 1e+5); Casimir apparoach
fiber drawing time 120 seconds

breakup time τ (unit seconds)

wavelength λ (unit μm)
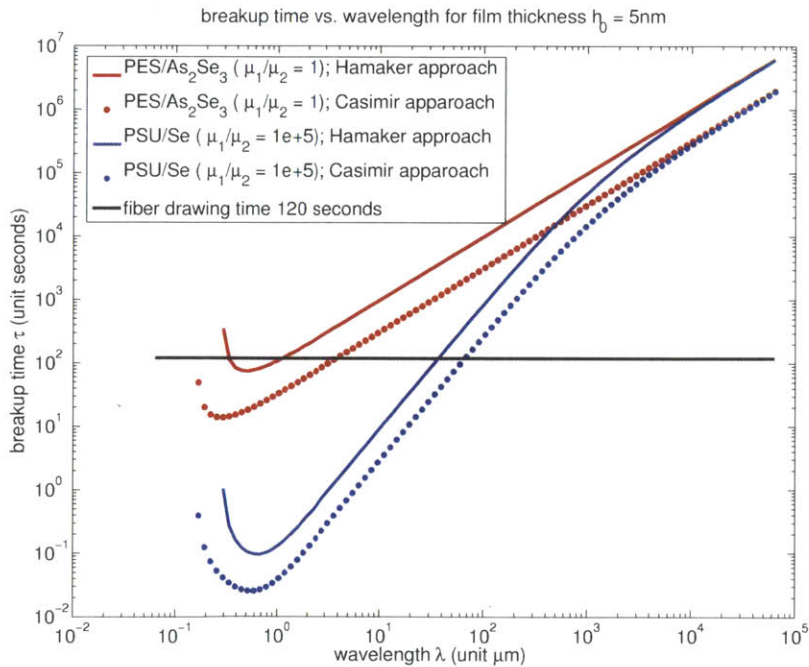
Figure 2-12: Breakup time versus wavelength for film thickness h_0 = 5 nm, computed for a planar film under competing influences of surface tension (which resists breakup) and attractive long-range (van der Waals/Casimir) interactions (which favor breakup), as discussed in section 2.12.1.

75
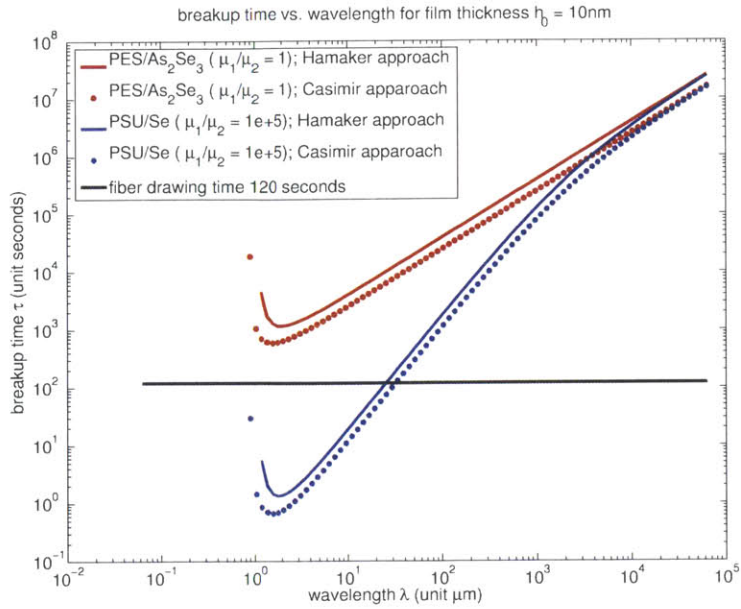
Figure 2-13: Breakup time vs wavelength for film thickness $h_0 = 10$ nm, computed for a planar film under competing influences of surface tension (which resists breakup) and attractive long-range (van der Waals/Casimir) interactions (which favor breakup), as discussed in section 2.12.1.
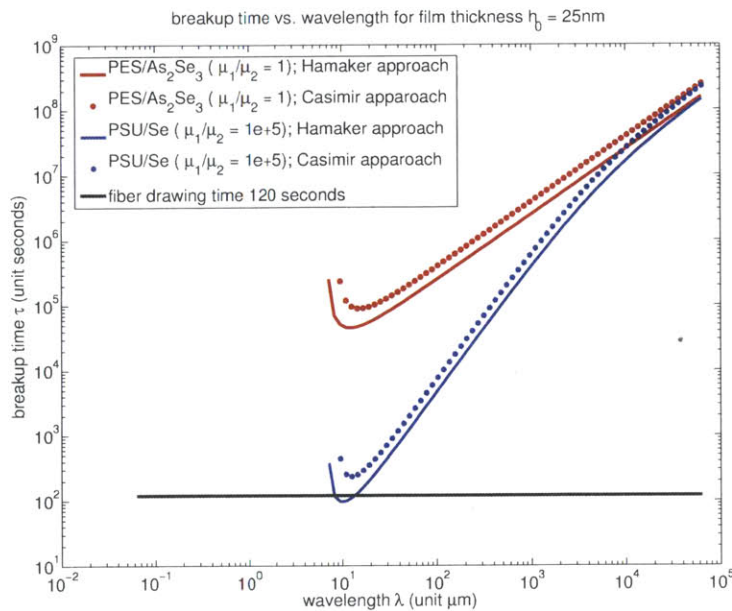
Figure 2-14: Breakup time vs wavelength for film thickness $h_0 = 25$ nm, computed for a planar film under competing influences of surface tension (which resists breakup) and attractive long-range (van der Waals/Casimir) interactions (which favor breakup), as discussed in section 2.12.1.

2.13 Conclusions

In this chapter, we presented a complete linear stability analysis of concentric cylindrical shells in the Stokes regime (with the Navier–Stokes regime in Section 2.11) and considered a few interesting examples and limiting cases. Many possibilities present themselves for future work. First, even in the cylindrical Stokes regime, only a few combinations of thicknesses and material properties have been considered so far—it seems quite possible that consideration of larger parameter spaces, perhaps aided by computational optimization, could identify additional regimes for breakup processes, such as competitions between additional length scales or "effective" properties in many-layer systems that differ substantially from the constituent materials. Second, one could extend this work beyond the incompressible Navier–Stokes regime to include fluid compressibility or even other physical phenomena such as viscoelasticity that may play a role in experiments (for example, fibers are drawn under tension). Third, one could consider non-cylindrical geometries. This seems especially important in light of the recent experimental observations of azimuthal breakup in cylindrical thin-shell fiber structures [29], since this chapter points out that azimuthal breakup cannot arise in purely cylindrical structures (at least, not from surface tension alone). Instead, one may need to consider the "neck-down" structure of the fiber-drawing process, in which a large preform is pulled to a long strand with a much smaller diameter. More generally, such intriguing experimental results indicate that a rich variety of new instability phenomena may arise in emerging multi-fluid systems, with corresponding new opportunities for theoretical analysis.

Chapter 3

Applications of in-fiber capillary instability

In this chapter, we describe how our theoretical approach was successfully applied to experimental micro- and nano- particle fabrication recently performed by our collaborators and published in [58]. By controlling the in-fiber fluid instability, our collaborators recently developed a novel technique to fabricate uniformly sized, structured spherical particles spanning an exceptionally wide range of sizes from millimeters down to nanometers [58]. With this new approach, they also produced composite spherical particles, such as core-shell particles (figure 3-3) and two-compartment Janus particles (figure 3-7). We first review this approach of particle fabrication in section 3.1, then apply our theoretical and computational tools developed in chapter 2 into these experimental breakup processes (sections 3.2 and 3.4), and predict consistent results for the size of core-shell particles (section 3.2).

3.1   In-fiber fluid instability

Here we briefly describe the experimental approach to particle generation with capillary instability. The first step is to prepare the preform, which is assembled from the intended particle constituent materials encased in a supporting cladding. The next step is to heat the preform to viscous state and thermally draw it into an extend fiber
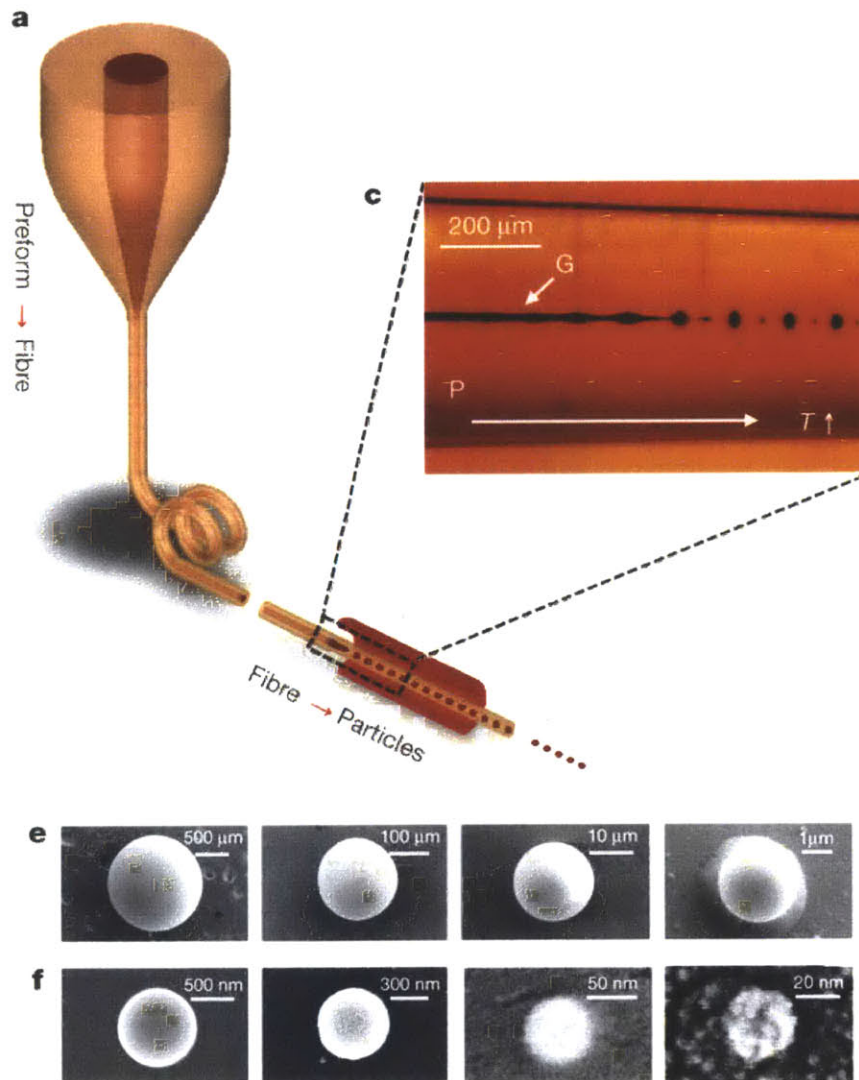
Figure 3-1: Fluid capillary instabilities in multimaterial fibers as a route to size-tunable particle fabrication (Kaufman, et al. 2012). (a) A preform is drawn into a fiber. (c) The capillary instability induced breakup of the fiber core with a temperature gradient. (e–f) SEM images of microparticles and nanoparticles.

until the core diameter approaches the required particle size (figure 3-1a). Finally, these extended fibers are put into furnace and heated (figure 3-1b). As the temperature increases, surface tension dominates and a sinusoidal perturbation grows, causing the core to break up into a string of particles (figure 3-1c). Depending on the diameter of the fiber put into the furnace, one can get a wide range of particles from millimeter to nanometer scales. (figures 3-1e-f).
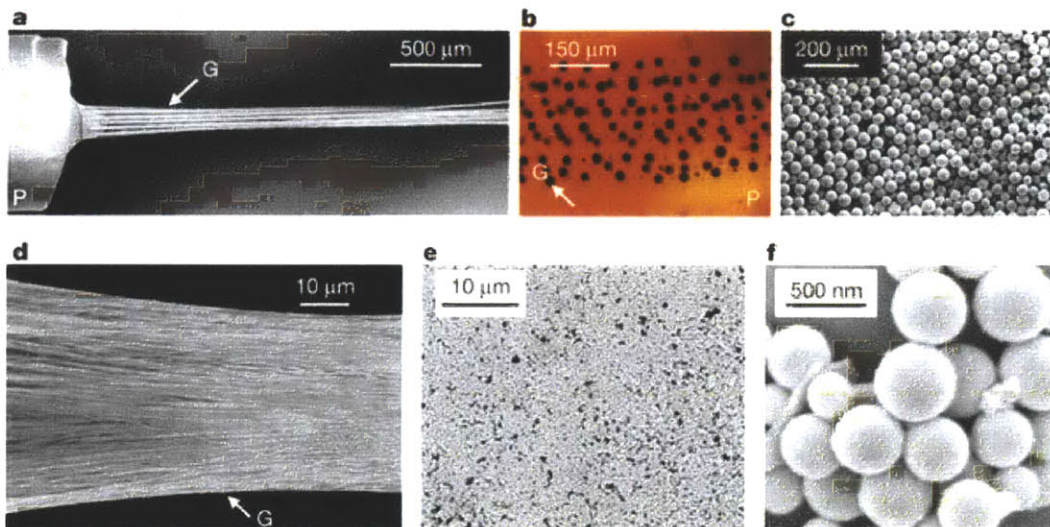
Figure 3-2: Scalable fabrication of micro- and nano-scale spherical particles (Kaufman, et al. 2012). (a) SEM micrograph of 12 20-micron glass cores. (b) Transmission optical micrograph of the fiber side-view, after the global heating of the fiber. (c) SEM image of glass particles (averages diameter 40-μm). (d) SEM micrograph of 27000 200-nm glass cores. (e–f) SEM images of glass particles (average diameter 400-nm).

One key aspect of the in-fiber breakup process is its scalability, that is the ability to produce large number of particles by parallelizing the simultaneous breakup of many cores occupying the same long fiber. Staring from a 1 mm preform and using the stack-and-draw approach, our collaborators were able to produce either 12 20-micron glass cores (figure 3-2a) or 27000 200-nm diameter glass cores (figure 3-2d), and break up all cores simultaneously into particles. The SEM images of the resulting particles are shown in figures 3-2c, f.

Another characteristic of this approach is the ease to produce complicated structured particles, like the core-shell particle (figure 3-3) and Janus particles (figure 3-7).

Because the preform is constructed at the centimeter scale, complex preform geometries may be readily designed and realized, so that the capillary instability driven breakup in the drawn fiber produces a desired particle structure.

3.2 Core-shell particles

In this section, we analyze the breakup process for core-shell particles reported in [58] with two techniques developed in previous chapter: linear stability analysis and full 3d Stokes simulations. The preform used to produce the core-shell particles consists of a polymer-core (diameter D_1) and glass cladding (diameter $D_2 = 2.5D_1$), surrounded by a polymer matrix (figure 3-3a; cross-sections shown in figure 3-3b, c). The polymer core and glass shell undergo a correlated capillary instability driven breakup that results in core-shell particles, observed experimentally (figures 3-3d, e, g, h).

The key quantity to determine is the wavelength of the growth mode with the fastest growth rate, which should determine the size of the generated droplets [101]. (Here, because there are two interfaces, we use the "effective" growth rate defined in section 2.7 which weights the growth rates by the relative amplitudes of the motion of each interface.) The dominant breakup wavelength, in units of the initial outer diameter, is plotted as a function of the viscosity ratio in figure 3-4. For much of the viscosity range, we actually find two growth modes that have very similar growth rates but at different lengthscales, which indicates that there may be competing breakup processes, offering the future possibility of controlling the droplet size by switching between these processes via changes in temperature or other parameters. The breakup lengthscale is consistent with the experimentally measured lengthscale λ as inferred from the final droplet radius D_1' and the initial diameter D_1 by conservation of mass $(\pi D_1'^3/6 = \lambda\pi D_1^2/4)$. Highlighted regions reflect the experimental uncertainty in D_1 (20–25 μm) and in the viscosity contrast due to the variation in temperature during the experiment, resulting in an uncertainty in λ.

Linear stability analysis only describes the initial growth of small perturbations.
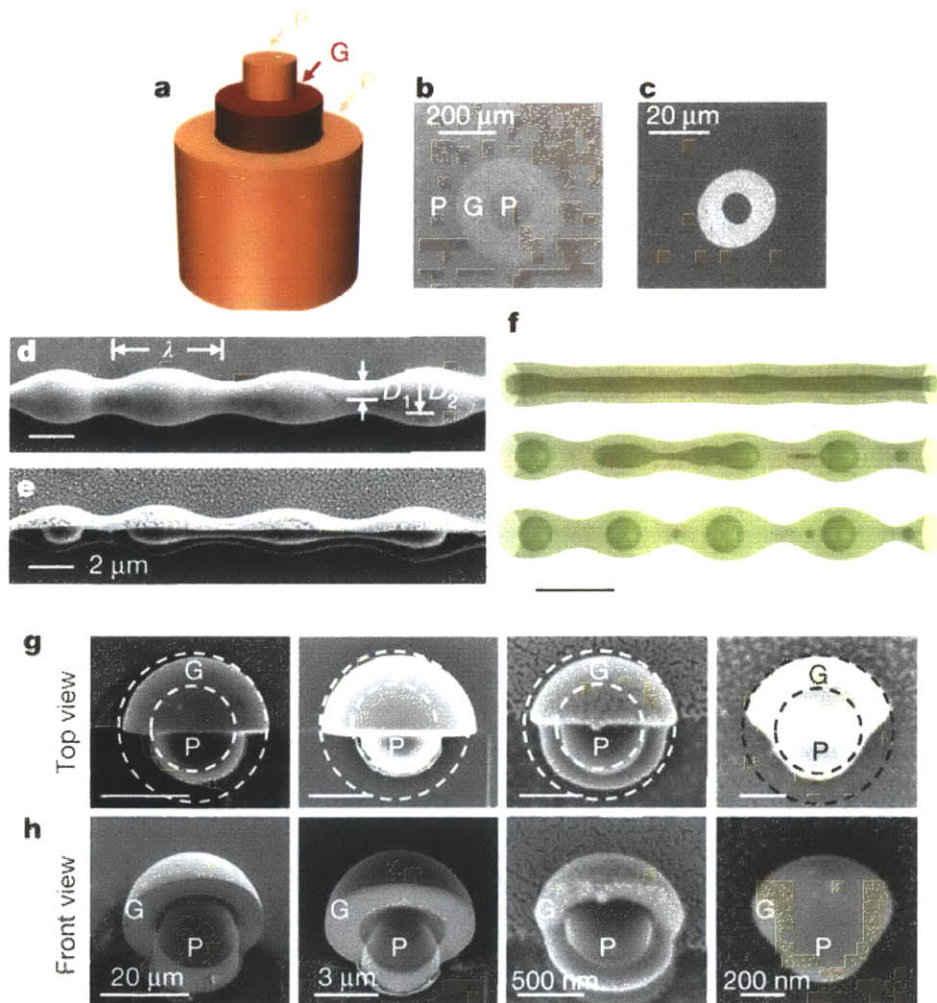
Figure 3-3: Polymer-core/glass-shell spherical particle fabrication (Kaufman, et al. 2012). (a) Schematic of the fiber structure. (b–c) SEM images of fiber cross-sections. (d) SEM image of glass-shell outer interface. (e) SEM image of inner polymer/glass interface and outer glass/polymer interface. (f) Three snapshots from a three-dimensional simulation of the Stokes equations using a representative fiber structure, illustrating the full breakup process. Time progresses from top to bottom. Dark green, polymer core; light green, glass shell; the outer polymer scaffold cladding is made transparent for clarity. (g–h) SEM top and front views of four differently sized core-shell particles.
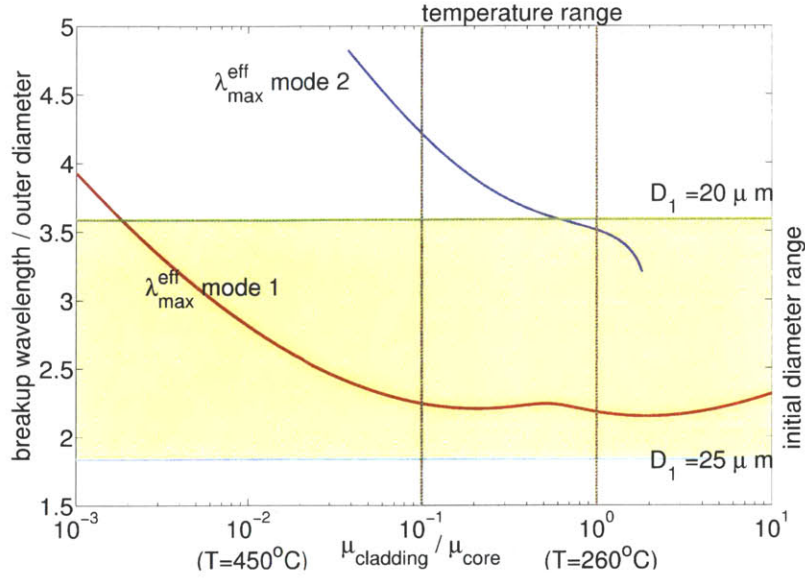
Figure 3-4: The dominant breakup wavelength, in units of the initial outer diameter, plotted as a function of the viscosity ratio. The breakup lengthscale (mode 1) is consistent with the experimentally measured lengthscale, within the uncertainties (highlighted region) in initial diameter D_1 and viscosity contrast.

To describe the full breakup process, particularly in the presence of competing growth modes, we turn to full 3d simulations of the Stokes equations (valid here since the Reynolds number is low [28]) by a level-set/spectral method described in our earlier work [66]. For illustration purposes, we picked parameters corresponding to equal viscosities $\mu = 10^5$ and an initial diameter $d = 23$ μm. Three snapshots of the simulation (starting from a white-noise initial perturbation) are shown in figure 3-3f, and illustrate the complexity of the breakup process. The inner interface breaks up first, as predicted from stability analysis and observed experimentally. As in the experimental image (figure 3-3e) at intermediate times we see droplets forming in some regions while the core is still connected in other regions, and we also occasionally observe small "satellite" droplets forming in between the larger droplets.

3.3 Design for single-droplet embedded core-shell particles

In this section, we propose a geometric criterion to have exactly one polymer (PES) droplet inside the glass (As_2Se_3) shell (figure 3-5a). More precisely, given the inner diameter D_1 and viscosities, we determine the range of D_2 to ensure single PES particle embedded in the As_2Se_3 shell.

(a) Single droplet embedded in one core-shell particle.

(b) Multiple droplets embedded in one core-shell particle.
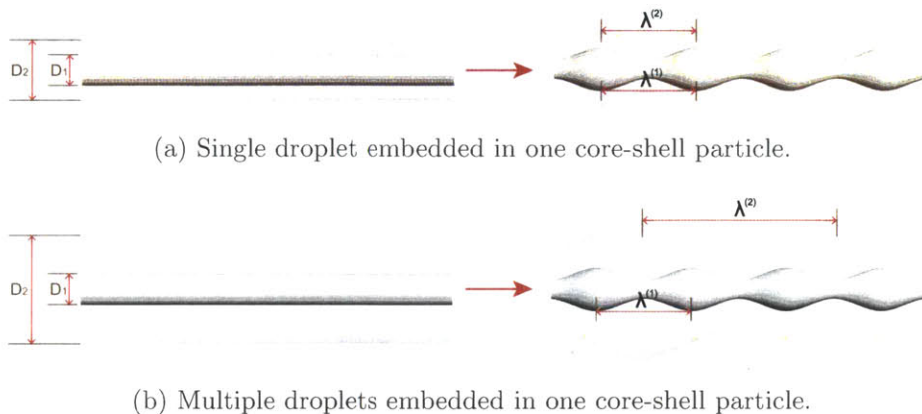
Figure 3-5: Sketches for (a) single and (b) multiple droplets embedded in one core-shell particle during breakup processes.

The analysis in section 2.8 can be applied to predict the breakup lengthscales of inner and outer interfaces $\lambda^{(1)}$ and $\lambda^{(2)}$. A possible choice of figure of merit is FOM $= (\lambda^{(2)} - \lambda^{(1)})/(\lambda^{(2)} + \lambda^{(1)})/2$, a dimensionless measure of the difference between breakup wavelengths of inner and outer interfaces. In figure 3-6, we plot the value of FOM as the map of viscosity ratio $\mu_{\text{shell}}/\mu_{\text{core}}$ and the diameter difference $(D_2 - D_1)/D_1$. The contours FOM $= 0.2, 0.3, 0.4$ are indicated by black curves. Note that figure 3-6a is for the case where the initial perturbations on inner and outer interfaces have the same amplitudes, while figure 3-6b assumes the initial perturbations on interfaces are proportional to their radii, as described in section 2.8.

If we choose some reasonable threshold, say FOM < 0.4, as the criterion for the formation of single-droplet embedded in core-shell particles, it predicts that structures with $(D_2 - D_1)/D_1 \leq 1.5$ or $D_2 \leq 2.5D_1$ are candidates to have single-droplet in each core-shell particle. The experimental observations of fabricated core-shell par-
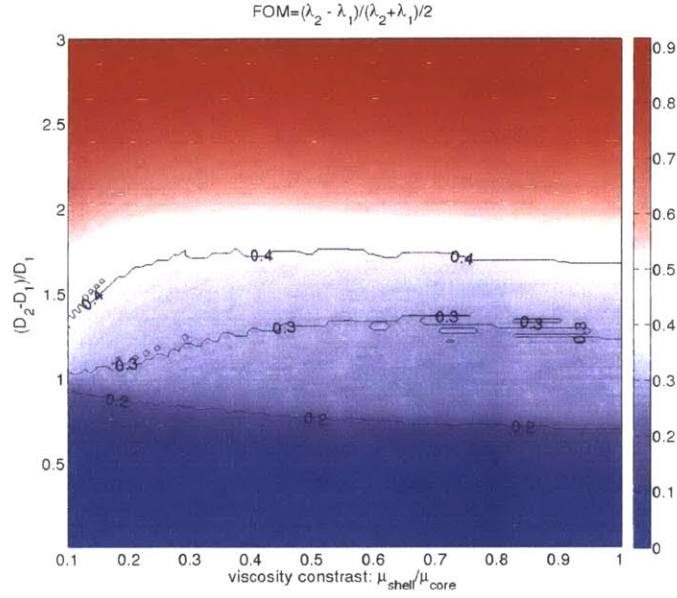
(a) Map of FOM for the case same initial perturbation amplitudes on both interfaces.
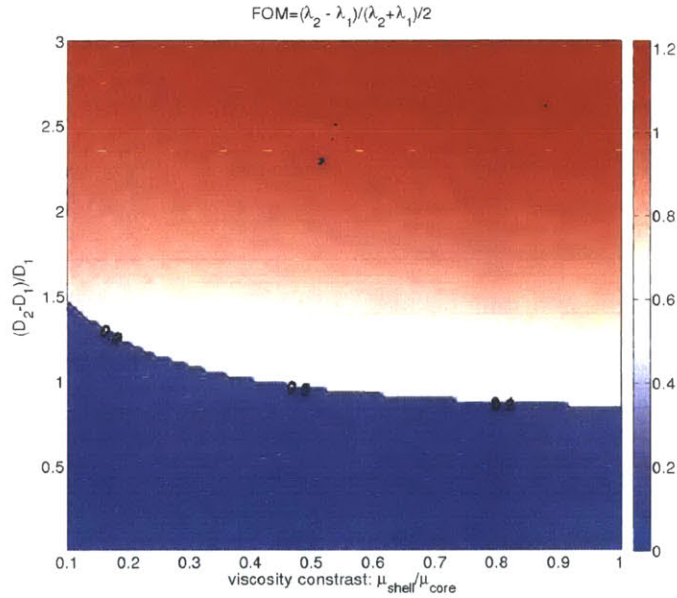
(b) Map of FOM for the case initial perturbation amplitudes on interfaces proportional to radii.

Figure 3-6: Maps of the figure of merit (FOM $= (\lambda^{(2)} - \lambda^{(1)})/(\lambda^{(2)} + \lambda^{(1)})/2$), a dimensionless measurement of the difference between breakup wavelengths of inner and outer interfaces, as a function of viscosity ratio $\mu_{\text{shell}}/\mu_{\text{core}}$ and diameter difference $(D_2 - D_1)/D_1$. Figures (a) and (b) are based on different assumptions of initial perturbation amplitudes on inner and outer interfaces (independent or proportional to radii).

ticles in section 3.2 support this prediction, and more experiments with different shell thicknesses are to be performed to further check this prediction. The same analysis can also be easily applied to the design of multi-layer ($N > 3$) nested particles.

3.4   Janus particles

Another interesting structured particle produced in [58] is a broken-symmetry, spherical Janus particle, comprising two hemispheres of different optical glasses (figure 3-7).The preform core is constructed of two half cylinders, each of a different semiconducting glass with distinct complex refractive index (figure 3-7a–c). The induced breakup produces spherical Janus particles held immobilized with the same orientation in the cladding (figure 3-7d). Figure 3-7e shows a reflection optical micrograph of a single Janus particle removed from the cladding.
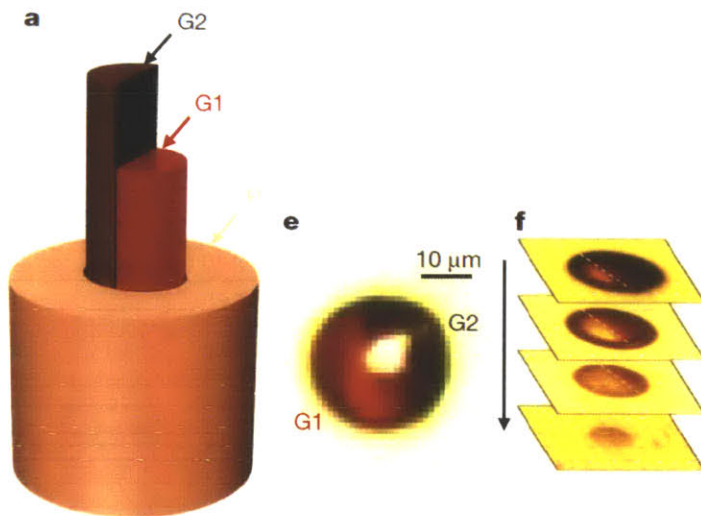
Figure 3-7: Broken-symmetry Janus particle fabrication (Kaufman, et al. 2012). (a) Schematic of the Janus preform. (e) Reflection optical micrograph of an Janus particle. (f) Optical micrographs of multiple sections at different depths within a single Janus particle.

Modeling Janus-particle formation is difficult because it involves a point where three fluids meet, so that sophisticated level-set techniques are required to describe the interfaces [109]. The physics of such a contact point is not well understood [34], although it is likely to be less relevant in the Stokes regime [26, 51]. Nevertheless,

energy considerations yield some qualitative predictions. A large glass-glass surface tension, compared to that between glass and polymer, would make it energetically favorable for the Janus particles to pinch in the center. On the other hand, for negligible glass-glass tension, if the glass-polymer surface tension were very different for the two glasses, energy would be lowered if one glass were to flow to envelop the other. As neither of these scenarios is observed experimentally (figures 3-7d, e), we can conclude that the observed breakup process is consistent with low glassglass surface tension and similar glass-polymer tensions. These considerations indicate a general strategy for the construction of particles with even more complex geometry.

Chapter 4

Microcavity optimization via the frequency-averaged local density of states

4.1 Introduction

In this chapter, we formulate a full 3d microcavity optimization problem with a novel technique involving a frequency-averaged local density of states (LDOS) [90]; in the next chapter, we solve this 3d optimization problem over all possible 2d-lithography patterns in a thin dielectric film and obtain a structure with lifetime $Q = 30000$ and modal volume $V = 0.06(\lambda/n)^3$. Unlike previous optimization work [5, 32, 41, 57, 89] which focused on Q and/or V (and was mainly limited to 2d computations), we start with a more fundamental physical quantity: the local density of states. With this new formulation, we are able to circumvent some difficulties in the Q and V approaches. For example, the simple formulation of maximizing Q/V leads to an ill-posed problem, because the maximum of Q/V is ∞, for example via a ring resonator (figure 1-3a) with infinite radius [78]. If Q/V is optimized, the finite Q and V obtained are just an artifact of the finite computation domain. In practice, there is an upper bound on the usable Q due to manufacturing constraints and other considerations discussed

in section 4.2, which we incorporate indirectly by optimizing a frequency-averaged LDOS as discussed below. Furthermore, for any optimization formulation involving Q and V through solving the Maxwell eigenproblem, there is a fundamental question of which eigenvalue should be optimized; simply asking for a mode closest to some design frequency $\tilde{\omega}$ leads to discontinuities. We avoid these difficulties by optimizing the local density of states or its variants (depending on specific applications), which involves solving only a scattering problem (a linear equation) rather than an eigenproblem. As we review below, the LDOS is related to the imaginary part of the Green's function, which is a solution to Maxwell's scattering problem [25, 79, 90], and in fact, the LDOS is actually proportional to the power radiated by an oscillating dipole current [50, 90]. Moreover, by exploring the causality of the scattering problem [the electric fields come after (not before) the current] in section 4.4.1, we turn the problem of maximizing the LDOS over some bandwidth, which seems to involve solving scattering problems at many frequencies in the bandwidth, into a single scattering problem at a complex frequency, using the technique of contour integration. In section 4.3, we propose different figures of merit in terms of the LDOS based on different real applications, e.g., a dipole at a fixed point with a fixed polarization (equivalent of optimizing Purcell factor), a dipole at a fixed point with random polarization, or dipoles randomly distributed in some region following some distribution. Since causality applies to all of these situations, the same frequency-averaging technique works for all of them. From the optimization perspective, we show in section 4.7.2 that minimizing 1/LDOS is a better objective than maximizing the LDOS, because this simple transformation turns the difficult narrow-ridge optimization problem into a simpler shallow-valley one. Numerically, we implement a parallel finite difference frequency domain (FDFD) solver for Maxwell's scattering problem with the sparse-matrix library PETSc [8, 9, 10] and spare-direct solver library PaStiX [48] as described in section 4.7. We use the standard gradient-based optimization methods (e.g., quasi-Newton algorithm LBFGS [71] and conservative convex separable approximation (CCSA) methods [115]) with our in-house optimization toolkit NLOPT [55] as described in section 4.7.2. As presented in the next chapter, our numerical simulations discover a silicon-slab

structure at reasonable large $Q = 30000$ with modal volume $0.06(\lambda/n)^3$, four times smaller than the smallest modal volume (at same order of Q) found in the literature [89]. We obtained promising results for heavily studied silicon slabs in infrared, for which various small-parameter hand optimizations had been performed for more than 20 years [54]. If our large-scale optimization is applied to less studied material regimes, e.g. metal-coated dielectrics (surface plasmon modes), or lower-index materials for visible light (weak or no 2d photonic bandgaps [54] to build off of), the potential gains seem even greater.

This chapter is organized as follows. To circumvent the difficulties of eigenproblem formulation for cavity optimization (section 4.2), we introduce our novel LDOS formulation (section 4.3) and propose a technique to obtain frequency-averaged LDOS by solving a single scattering problem (section 4.4). We summarize our LDOS formulation in section 4.6 and discuss the numerical implementation for FDFD solver as well as optimization schemes in section 4.7.

4.2 Eigenproblem formulation

There are two key figures of merit for a resonant mode $\mathbf{E}^n(\mathbf{x})$ of a cavity: quality factor Q and modal volume V. The quality factor Q is a dimensionless lifetime, and $1/Q$ is a dimensionless decay rate [54]. Mathematically, Q is related to the frequency-domain Maxwell eigenvalue problem:

$$\nabla \times \frac{1}{\mu(\mathbf{x})} \nabla \times \mathbf{E}^n(\mathbf{x}) = \omega_n^2 \varepsilon(\mathbf{x}) \mathbf{E}^n(\mathbf{x}) \tag{4.1}$$

with radiation boundary conditions. Because of the lossy boundary conditions, the eigenproblem is non-Hermitian and the eigenvalues are complex. The Q for the mode $\mathbf{E}^n(\mathbf{x})$ with eigenfrequency ω_n [54] is

$$Q = \frac{\Re[\omega_n]}{-2\operatorname{Im}[\omega_n]}. \tag{4.2}$$

The modal volume V [21], defined as

$$V = \frac{\int \varepsilon(\mathbf{x})|\mathbf{E}^n(\mathbf{x})|^2 d\mathbf{x}}{\max\{\varepsilon(\mathbf{x})|\mathbf{E}^n(\mathbf{x})|^2\}},$$ (4.3)

is a measurement for how big the mode is. The Purcell factor [99], known as the enhancement of spontaneous emission rate, can be written as [60, 90]

$$F = \frac{3Q}{4\pi^2 V}\left(\frac{\lambda}{n}\right)^3.$$ (4.4)

Here λ is the wavelength, and n is the index of refraction.

For most applications with light-matter interactions (such as lasers, sensors, and nonlinear frequency converters), maximal life time Q and minimal modal volume V are desirable. It is tempting to use the Purcell factor F in (4.4) or Q/V as the figure of merit for cavity optimization. Unfortunately, maximizing Q/V leads to an ill-posed problem, because the maximum of Q/V is ∞ as in the example of a perfect ring resonator with infinite radius. Reference [78] showed that there is a trade-off between V (proportional to the circumference) and Q (proportional to exponential of the radius). In practice, any optimization in a finite computation cell will obtain a finite Q and V, but the values are just an artifact of the finite computational domain. In this sense, maximizing Q/V is not well-posed because the solution does not converge as you increase the size of the computational domain.

In practice, however, there is an upper bound on the useful Q for two reasons. First, besides the intrinsic radiation loss (Q_{rad}), there are also radiation losses due to surface roughness ($Q_{roughness}$) and material absorption ($Q_{absorption}$). The total loss rate $1/Q_{loss}$ is the sum of these three effects:

$$\frac{1}{Q_{loss}} = \frac{1}{Q_{rad}} + \frac{1}{Q_{roughness}} + \frac{1}{Q_{absorption}}.$$ (4.5)

In real applications, the Q_{loss} cannot be arbitrarily large. For example, in integrated optics it is difficult to get Q_{loss} more than a few million due to surface roughness. Second, there is another quality factor in the system. For any cavity based device,

the cavity is always intentionally coupled to some channels (e.g., waveguides) to get light in and out. That coupling process will be described by its own life time Q_{coupling}. It turns out that the losses in this coupled device go like $Q_{\text{coupling}}/Q_{\text{loss}}$. Once these losses are decreased below some threshold, it does not matter in practice if we decrease them further.

Now we have a better formulation:

$$\min V$$
$$\text{s.t.} Q \geq \tilde{Q},$$

$$(4.6)$$

where $\tilde{Q}$ is determined by the bandwidth and loss tolerance of applications. By solving the non-Hermitian Maxwell eigen-problem (4.1), we can obtain Q and V from eigenvectors $\mathbf{E}^n(\mathbf{x})$ and eigenvalues ω_n through (4.2) and (4.3). Then a natural question to ask is which eigenvalue we should optimize. In practice, we have some design frequency $\tilde{\omega}$ given by the application, so we should optimize the eigenvalue closest to $\tilde{\omega}$. (Note that Maxwell's equations are scale invariant. We can just rescale the structure to put any eigenvalue at any frequency we want, so we can just pick $\tilde{\omega}$ arbitrarily. The only real computational choice is the resolution: the number of pixels per wavelength.) However, asking for the mode closest to $\tilde{\omega}$ leads to discontinuities: as the structure changes during optimization, it will tend to hop discontinuously between modes. Although there are some ways to deal with this [32], the problem becomes worse when we simulate the radiation loss, because in this case the finite cell is approximating a continuum of radiation modes above and below the slab. As a result, there are more and more closely spaced modes as the cell size increases. Hence, we want to circumvent this difficulty by adopting a new approach: turning the eigenproblem into a linear scattering problem.

4.3 LDOS formulation

The Local Density of States (LDOS) (the number of states per unit volume per unit frequency) [50] is a more fundamental physical quantity than Q/V or the Purcell

factor (4.4). For example, in quantum electrodynamics, the spontaneous emission rate of an oscillating dipole ($\delta(\mathbf{x} - \mathbf{x}')e^{-i\omega t}\hat{\mathbf{e}}_j$) is proportional to the partial local density of states (or local density of states per polarization) LDOS_j. Mathematically, LDOS_j is easy to compute because it is well known that it only depends on the dyadic Green's tensor $\mathbf{G}(\mathbf{x}, \mathbf{x}')$:

$$\text{LDOS}_j(\omega, \mathbf{x}') = \frac{6\omega}{\pi} \text{Im}[\hat{\mathbf{e}}_j \cdot \mathbf{G}(\mathbf{x}', \mathbf{x}') \cdot \hat{\mathbf{e}}_j]. \tag{4.7}$$

The Green's tensor satisfies

$$\left[\nabla \times \frac{1}{\mu(\mathbf{x})} \nabla \times -\varepsilon(\mathbf{x})\omega^2 \right] \mathbf{G}(x, x') = \mathbf{I}\delta(\mathbf{x} - \mathbf{x}'). \tag{4.8}$$

In appendix B.2, we reviewed the derivation that the integration of LDOS_j over all the polarizations and the space gives the density of states (DOS).

One can also understand the LDOS from another point of view [50, 90]: it is proportional to the power radiated or dissipated by a point dipole $\mathbf{J}(\mathbf{x}) = \delta(\mathbf{x} - \mathbf{x}')\hat{\mathbf{e}}_j$. Poynting's theorem [52] implies that the power radiated by a dipole $\mathbf{J}(\mathbf{x})$ is

$$P_j(\omega, \mathbf{x}') = -\frac{1}{2} \int \Re\left[\mathbf{J}^*(\mathbf{x}) \cdot \mathbf{E}(\mathbf{x})\right] d\mathbf{x}, \tag{4.9}$$

where $\mathbf{E}(\mathbf{x})$ is the total electric field solving the frequency-domain scattering problem

$$\mathcal{M}(\varepsilon, \omega)\mathbf{E}(\mathbf{x}) = i\omega\mathbf{J}(\mathbf{x})$$
$$\mathcal{M}(\varepsilon, \omega) = \nabla \times \frac{1}{\mu(\mathbf{x})} \nabla \times -\varepsilon(\mathbf{x})\omega^2 \tag{4.10}$$
$$\mathbf{J}(\mathbf{x}) = \delta(\mathbf{x} - \mathbf{x}')\hat{\mathbf{e}}_j.$$

Because the dyadic Green's tensor is precisely proportional to this solution $\mathbf{E}$ by definition, it is easy to see that $P_j(\omega, \mathbf{x}')$ is proportional to LDOS_j

$$P_j(\omega, \mathbf{x}') = -\frac{1}{2} \int \Re\left[\mathbf{J}^*(\mathbf{x})\mathcal{M}^{-1}(i\omega\mathbf{J}(\mathbf{x}))\right] d\mathbf{x} = \frac{\omega}{2} \text{Im}[\hat{\mathbf{e}}_j \cdot \mathbf{G}(\mathbf{x}', \mathbf{x}') \cdot \hat{\mathbf{e}}_j] = \frac{\pi}{12}\text{LDOS}_j(\omega, \mathbf{x}'), \tag{4.11}$$

94

We propose that LDOS$_j$ or its variants can be used as figure of merit for the characterization and optimization of a microcavity. Note that the figure of merit should really depend on the application. For example, if we are interested in the spontaneous emission rate for the dipole at a specific position $\mathbf{x}'$ with a specific polarization $\hat{\mathbf{e}}_j$, then LDOS$_j(\omega, \mathbf{x}')$ is the most relevant figure of merit. The Purcell factor or Q/V is actually an approximation to this LDOS$_j$, valid for the system with high Q [42, 60], as reviewed in Appendix B.1, assuming that the point $\mathbf{x}'$ of maximum $\varepsilon \mathbf{E}(\mathbf{x})^2$ is used to evaluate the LDOS. If the application is for a dipole at a specific point $\mathbf{x}'$ with a randomly distributed polarization, then the figure of merit would be mean$_j$ LDOS$_j(\omega, \mathbf{x}')$ or min$_j$ LDOS$_j(\omega, \mathbf{x}')$. Instead of at a single point $\mathbf{x}'$, if the dipoles of interest are distributed [with probability density function $s(\mathbf{x})$] in a region V with polarization $\hat{\mathbf{e}}_j$, the most relevant figure of merit in this case is $\int_V$ LDOS$_j(\omega, \mathbf{x})s(\mathbf{x})d\mathbf{x}$. Depending on the applications for enhancement or inhibition, we should maximize or minimize the figure of merit correspondingly.

For all the applications we mentioned, the LDOS$_j$ is really the basic building block. We are going to mainly focus on this case: maximize the spontaneous emission rate for a dipole at a point $\mathbf{x}'$ with polarization $\hat{\mathbf{e}}_j$. For simplicity, from now on, we shall omit the explicit j and $\mathbf{x}'$ dependence from LDOS$_j(\omega, \mathbf{x}')$, and simply write LDOS(ω) to denote this figure of merit, namely

$$\text{LDOS}(\omega) = -\frac{6}{\pi}\Re\left[\int \mathbf{J}^*(\mathbf{x}) \cdot \mathbf{E}(\mathbf{x})d\mathbf{x}\right]. \qquad (4.12)$$

In section 5.2, however, we will also demonstrate a case where the dipole polarization is randomly distributed.

4.4 Frequency-averaged LDOS

In previous section, we proposed that one way of framing the problem of microcavity design is to maximize the local density of states around some design frequency $\tilde{\omega}$.

As explained in section 4.2, we wish to impose only a lower bound $\tilde{Q}$ on the cavity lifetime. In terms of the LDOS, this is essentially equivalent to maximizing *average* LDOS over a finite bandwidth $\Gamma = \tilde{\omega}/2\tilde{Q}$. In particular, we will maximize an average L given by:

$$L = \int_{-\infty}^{\infty} \text{LDOS}(\omega)W(\omega)\text{d}\omega. \qquad (4.13)$$

Here, $W(\omega)$ is some weight function or window function we choose, which is peaked around the design frequency $\tilde{\omega}$ and decays rapidly (with a finite integral) outside of a bandwidth Γ around $\tilde{\omega}$. At first glance, it seems that computing the average L requires a numerical integration over all ω, which would involve solving scattering problems at many frequencies in the bandwidth. It turns out, however, that we only need to solve *one* scattering problem to obtain the mean LDOS with the technique of contour integration. This simplification, combined with the fact that we need not solve any eigenproblem, makes this formulation far more practical to implement than imposing an explicit bound on Q.

4.4.1 Causality and analyticity

Before we proceed, we first define a function $f(\omega)$, which is a complex version of $\text{LDOS}(\omega)$:

$$f(\omega, \mathbf{x}') = -\frac{6}{\pi} \int \mathbf{J}^*(\mathbf{x}) \cdot \mathbf{E}(\mathbf{x}, \omega)\text{d}\mathbf{x}. \qquad (4.14)$$

Comparing with (4.12), it is clear that $\text{LDOS}(\omega) = \Re[f(\omega)]$. [Here we omitted the $\mathbf{x}'$ dependency of $f(\omega, \mathbf{x}')$.] Note that the operator $\mathcal{M}(\varepsilon, \omega)$ is an linear operator relating the electric field $\mathbf{E}(\mathbf{x}, \omega)$ to the (time-harmonic) input electric current $\mathbf{J}(\mathbf{x})$ at a given frequency ω. Causality [the electric field $\mathbf{E}(\mathbf{x}, \omega)$ comes after (not before) the current $\mathbf{J}(\mathbf{x})$] implies that $\mathbf{E}(\mathbf{x}, \omega)$ is analytic in the upper-half complex-ω plane [64]. Therefore, $f(\omega)$ is also analytic in the upper-half complex-ω plane.
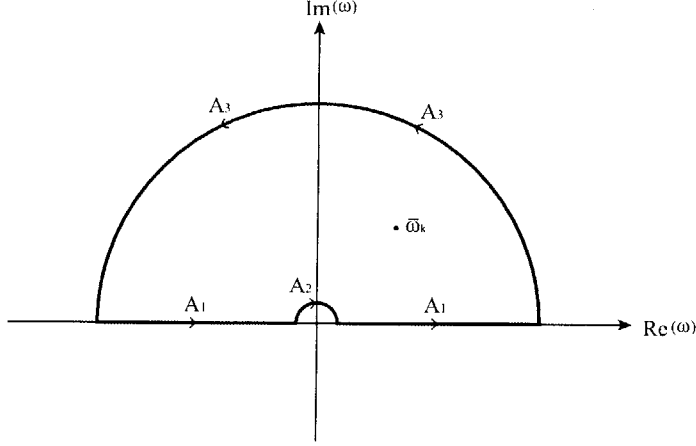
Figure 4-1: Contour integration path. The frequency-averaged LDOS is the path integral along arc A_1. By choosing the proper window/weight function $W(\omega)$, the contribution along arcs A_2 and A_3 can be negligible comparing to the one from A_1. Therefore, the residues at poles $\bar{\omega}_k$ enclosed by this contour can be used to approximate the averaged LDOS.

4.4.2 Contour integration

In this section, we are going to compute the mean L by exploiting the analyticity of $f(\omega)$

$$L = \int_{-\infty}^{\infty} \text{LDOS}(\omega) W(\omega) d\omega = \int_{-\infty}^{\infty} \Re[f(\omega)] W(\omega) d\omega = \Re\left[\text{p.v.} \int_{-\infty}^{\infty} f(\omega) W(\omega) d\omega\right].$$
(4.15)

Here p.v. denotes the Cauchy principle value, because the imaginary part of $f(\omega)$ may have singularity at $\omega = 0$, as in the case of $f(\omega)$ in free space [20, 52, 79, 85]. Now we want to complete our integration contour (Figure 4-1) in the upper-half plane and evaluate L by residue theorem [3]

$$\int_{A_1} + \int_{A_2} + \int_{A_3} f(\omega) W(\omega) d\omega = 2\pi i \sum_k \text{Res}\left[f(\omega) W(\omega), \bar{\omega}_k\right].$$
(4.16)

Here $\bar{\omega}_k$ denotes the poles of $W(\omega)$ in the upper-half plane and the residue can be calculated as

$$\text{Res}[g(w), \bar{\omega}_k] = \frac{1}{(s-1)!} \lim_{\omega \to \bar{\omega}_k} \frac{d^{s-1}}{dw^{s-1}} \left[(\omega - \bar{\omega}_k)^s g(\omega)\right]$$
(4.17)

97

given that $\bar{\omega}_k$ is a pole of order s.

For the weight function $W(\omega)$, if it decays faster than $1/|\omega|^3$ for large ω, the contribution from arc A_3 will be zero since $\text{LDOS}(\omega)$ is proportional to ω^2 in 3d (or ω in 2d) free space and $f(\omega)W(\omega)$ will decay faster than $1/|\omega|$ on arc A_3. We can obtain the contribution from arc A_2 by evaluating the residue due to the simple pole of $f(\omega)$ at $\omega = 0$

$$\int_{A_2} f(\omega)W(\omega)\mathrm{d}\omega = -\frac{1}{2}2\pi i W(0)\lim_{\omega\to 0}\omega f(\omega). \tag{4.18}$$

The factor $-1/2$ comes from the fact that the integration is along a clockwise semicircle. Since the weight function is peaked around design frequency $\tilde{\omega}$ with some narrow bandwidth Γ, we should expect that $W(0)$ is small, and the contribution from A_2 is negligible comparing to the residues at $\bar{\omega}_k$. From (4.15), L is just the path integral along the path A_1 [64]. Therefore, we have

$$\begin{aligned} L &= \Re\left[2\pi i\sum_k \text{Res}\left[f(\omega)W(\omega),\bar{\omega}_k\right] - \left(\int_{A_2} + \int_{A_3} f(\omega)W(\omega)\mathrm{d}\omega\right)\right] \\ &\approx \Re\left[2\pi i\sum_k \text{Res}\left[f(\omega)W(\omega),\bar{\omega}_k\right]\right]. \end{aligned} \tag{4.19}$$

4.4.3   Scattering problem at complex frequency

To compute the residue at the complex poles, we need to solve the scattering problem at complex frequencies. More precisely, the scattering problem (4.10) at complex frequency $\tilde{\omega} + i\Gamma$ can be written as

$$\begin{aligned} &\left(\nabla\times\frac{1}{\mu(\mathbf{x})}\nabla\times -\varepsilon(\mathbf{x})(\tilde{\omega}+i\Gamma)^2\right)\mathbf{E}(\mathbf{x},\tilde{\omega}+i\Gamma) = i(\tilde{\omega}+i\Gamma)\mathbf{J}(\mathbf{x}) \\ \Longleftrightarrow &\left(\nabla\times\frac{1}{\mu(\mathbf{x})(1+i\frac{\Gamma}{\tilde{\omega}})}\nabla\times -\varepsilon(\mathbf{x})\tilde{\omega}^2\left(1+i\frac{\Gamma}{\tilde{\omega}}\right)\right)\mathbf{E}(\mathbf{x},\tilde{\omega}+i\Gamma) = i\tilde{\omega}\mathbf{J}(\mathbf{x}) \\ \Longleftrightarrow &\left(\nabla\times\frac{1}{\mu(\mathbf{x})(1+\frac{i}{2Q})}\nabla\times -\varepsilon(\mathbf{x})\left(1+\frac{i}{2Q}\right)\tilde{\omega}^2\right)\mathbf{E}(\mathbf{x},\tilde{\omega}+i\Gamma) = i\tilde{\omega}\mathbf{J}(\mathbf{x}). \end{aligned} \tag{4.20}$$

We denote this complex scattering operator by $\tilde{\mathcal{M}}(\varepsilon, \tilde{\omega})$, namely

$$\tilde{\mathcal{M}}(\varepsilon, \tilde{\omega}) = \nabla \times \frac{1}{\mu(\mathbf{x})(1 + \frac{i}{2\tilde{Q}})} \nabla \times -\varepsilon(\mathbf{x}) \left(1 + \frac{i}{2\tilde{Q}}\right) \tilde{\omega}^2 = \nabla \times \frac{1}{\tilde{\mu}(\mathbf{x})} \nabla \times -\tilde{\varepsilon}(\mathbf{x}) \tilde{\omega}^2.$$

(4.21)

Clearly, this is equivalent to solving a scattering problem at real frequency $\tilde{\omega}$ with materials $\tilde{\varepsilon}(\mathbf{x}) = \varepsilon(\mathbf{x})(1 + i/2\tilde{Q})$ and $\tilde{\mu}(\mathbf{x}) = \mu(\mathbf{x})(1 + i/2\tilde{Q})$. (In fact, any change to the frequency can be converted into a change of materials.) In particular, adding a positive imaginary part to $\tilde{\omega}$ corresponds to a positive imaginary part in $\tilde{\varepsilon}(\mathbf{x})$ and $\tilde{\mu}(\mathbf{x})$, which corresponds (with our $e^{-i\omega t}$ convention) to an absorption loss.

Therefore, solving scattering problems at a frequency in the upper-half complex plane is equivalent to solving a real frequency scattering problem where absorption losses have been added everywhere in space. There is an intuitive physical explanation for why this corresponds to requesting a cavity with quality factors $\geq \tilde{Q}$ (which was the motivation in section 4.4 for computing the mean LDOS). If we add an absorption loss with quality factor $\tilde{Q}$ into the system, the LDOS optimization will not benefit from making $Q_{\mathrm{rad}} \gg Q_{\mathrm{absorption}} = \tilde{Q}$ (see eq. (4.5)). So Q_{rad} is effectively bounded, which is exactly we want.

In summary, with complex analysis, we convert the evaluation of frequency-averaged LDOS into a single scattering problem at a complex frequency. Moreover, we relate this complex-frequency scattering problem at a real frequency with transformed complex materials. Although such an application of complex analysis and contour integration to electromagnetic scattering problem is rather unusual, it is related to approaches more common in quantum field theory [96] and Casimir interactions in quantum field theory [56], and related ideas were recently applied to frequency averaged scattering cross-section in electromagnetism [47, 83].

4.5 Possible window functions

In this section, we discuss several window functions: a simple Lorentzian, the difference of two Lorenztians, the square of a Lorentzian.

4.5.1 A simple Lorentzian

A simple window function is a Lorentzian centered at $\tilde{\omega}$ with half-width Γ. The frequency-average LDOS against this weight is

$$L_1 = \int \text{LDOS}(\omega) \frac{\Gamma/\pi}{(\omega - \tilde{\omega})^2 + \Gamma^2} = \Re[f(\tilde{\omega} + i\Gamma)], \qquad (4.22)$$

which only requires solving the scattering problem (4.20) once. L_1 is a perfectly finite, well-defined quantity in a discretized simulation with a finite spatial resolution (finite grid). However, a careful examination reveals that this simple average does not converge as the resolution increases. There are two equivalent ways to understand this. First, in a continuous medium, the integral does not converge because the window function decays like $1/|\omega|^2$ while $\text{LDOS}(\omega)$ behaves like $|\omega|$ (in 2d free space) or $|\omega|^2$ (in 3d free space) for large $|\omega|$. (In a finite spatial resolution, there is an upper frequency cutoff that eliminates this divergence.) Second, from the relationship between the complex-frequency scattering and lossy material discussed in the previous section, we know that the residue $\Re[f(\tilde{\omega} + i\Gamma)]$ is actually the power emitted by a dipole in *lossy* material, which is the sum of the power radiating to the outside of the cavity and the power absorbed by the lossy material in the cavity [25]. It is known that this absorbed power is infinite because $\mathbf{E}(\mathbf{x})$ is divergent like $1/r^3$ in the neighborhood of the dipole (in 3d free space) [20, 79]. (In a lossless medium, only $\text{Im}[\mathbf{E}(\mathbf{x})]$ diverges as $1/r^3$, so $\text{LDOS} \sim \Re[\mathbf{E}(\mathbf{x})]$ is finite.) In discretized space, the Green's function is finite and diverges as (resolution)^3 in 3d.

To avoid this singularity, we need to choose window functions which decay faster than $|\omega|^3$ at large $|\omega|$. Two natural candidates are the difference of two Lorentzians and the square of a Lorentzian.

4.5.2 Difference of two Lorentzians

The divergence of L_1 can also be interpreted from the time domain analysis. With Fourier analysis, we can show that for a time domain real dipole current $\mathbf{J}(x,t) =$

$\mathbf{J}(\mathbf{x})s(t)$, the corresponding work done by this current is

$$\int_{-\infty}^{\infty} \int \mathbf{J}(x,t)\mathbf{E}(\mathbf{x},t)\mathrm{d}\mathbf{x}\mathrm{d}t = \int_{-\infty}^{\infty} \mathrm{LDOS}(\omega)|\hat{s}(\omega)|^2 \mathrm{d}\omega, \qquad (4.23)$$

where $\hat{s}(\omega)$ is the Fourier transform of $s(t)$. It is easy to see that L_1 is actually proportional to the work done by an oscillating decay current, $e^{-\Gamma t}\cos(\tilde{\omega}t)$, turned on at $t = 0$. The abrupt jump of this current at $t = 0$ causes this infinite amount of work. If the current is turned on at $t = 0$ in a continuous way, say $e^{-\Gamma t}\sin(\tilde{\omega}t)$, the work done by this current should be finite. Therefore, the new weight function

$$W_2(\omega) = \frac{|s(\tilde{\omega})|^2}{\int_{-\infty}^{\infty} |s(\tilde{\omega})|^2 \mathrm{d}\omega} = \frac{2\Gamma(\tilde{\omega}^2 + \Gamma^2)/\pi}{(\omega^2 - \tilde{\omega}^2 - \Gamma^2)^2 + 4\Gamma^2\omega^2} \qquad (4.24)$$

should produce the finite frequency-averaged LDOS. We check that this is indeed the case:

$$\begin{aligned}
L_2 &= \int \mathrm{LDOS}(\omega) \frac{2\Gamma(\tilde{\omega}^2 + \Gamma^2)/\pi}{(\omega^2 - \tilde{\omega}^2 - \Gamma^2)^2 + 4\Gamma^2\omega^2} \mathrm{d}\omega \\
&= \frac{\tilde{\omega}}{2}\left(\frac{\mathrm{LDOS}(\tilde{\omega} + i\Gamma)}{\tilde{\omega} + i\Gamma} + \frac{\mathrm{LDOS}(-\tilde{\omega} + i\Gamma)}{-\tilde{\omega} + i\Gamma}\right)\left(\frac{\tilde{\omega}^2 + \gamma^2}{\tilde{\omega}^2}\right). \quad (4.25)
\end{aligned}$$

Mathematically, the weight function $W_2(\omega)$ decays like $|\omega|^4$ for large $|\omega|$, therefore the contour integration technique works and the corresponding average is finite. Note that the weight function $W_2(\omega)$ can also be approximated by the difference of two Lorentzian functions with centers at $\tilde{\omega} + i\Gamma$ and $-\tilde{\omega} + i\Gamma$. As we discussed in the previous section, the average $\mathrm{LDOS}(\tilde{\omega} + i\Gamma)$ corresponds to add lossy material in the system, and the one $\mathrm{LDOS}(-\tilde{\omega} + i\Gamma)$ corresponds to add gain material to the system. Therefore, the singularities from the absorbed power in $\mathrm{LDOS}(\tilde{\omega} + i\Gamma)$ and from the gain power in $\mathrm{LDOS}(-\tilde{\omega} + i\Gamma)$ will cancel each other in the sum, and the average L_2 will be finite.

The only complication of this window function $W_2(\omega)$ is that computing the $\mathrm{LDOS}(-\tilde{\omega} + i\Gamma)$ requires solving scattering problem in systems with gain materials, which needs extra care to impose the radiating boundary condition [more precisely,

the perfect matched layer (PML) technique in truncating the computational domain needs to be modified correspondingly]. Instead, we propose an alternative, the square of a Lorentzian.

4.5.3 Square of a Lorentzian

The choice of the window function $W(\omega)$ is not unique, and any function that satisfies the criteria we discussed in section 4.4.2 is fine. To ensure that the $W(\omega)$ decays faster than $1/|\omega|^3$, we propose the window function,

$$W(\omega) = \frac{2\Gamma^3/\pi}{\left((\omega - \tilde{\omega})^2 + \Gamma^2\right)^2},\tag{4.26}$$

which is a normalized square of a Lorentzian function. This window function has a double-pole at $\omega = \tilde{\omega} + i\Gamma$ in the upper-half plane. With residue theorem (4.17), (4.19) and (4.26), we have

$$L = \int_{-\infty}^{\infty} \text{LDOS}(\omega)W(\omega)d\omega \approx \Re\left[f(\tilde{\omega} + i\Gamma) - i\Gamma f'(\tilde{\omega} + i\Gamma)\right],\tag{4.27}$$

where $f'(\cdot)$ denotes the differentiation with respect to ω. In appendix B.3, we showed that

$$f'(\omega, \mathbf{x}') = \frac{f(\omega, \mathbf{x}')}{\omega} + i\frac{12}{\pi}\int \varepsilon(\mathbf{x})\mathbf{E}^T(\mathbf{x}, \omega)\mathbf{E}(\mathbf{x}, \omega)d\mathbf{x}.\tag{4.28}$$

From (4.14) and (4.28), it is clear that both $f(\tilde{\omega} + i\Gamma)$ and $f'(\tilde{\omega} + i\Gamma)$ can be obtained from the scattering solution $\mathbf{E}(\mathbf{x}, \tilde{\omega} + i\Gamma)$ (see appendix B.4) and

$$f(\tilde{\omega} + i\Gamma) - i\Gamma f'(\tilde{\omega} + i\Gamma) = \frac{\tilde{\omega}}{\tilde{\omega} + i\Gamma}(-\frac{6}{\pi})\hat{\mathbf{e}}_j^* \cdot \mathbf{E}(\mathbf{x}', \tilde{\omega} + i\Gamma) + \frac{12}{\pi}\Gamma\int \varepsilon(\mathbf{x})\mathbf{E}^T(\mathbf{x}, \tilde{\omega} + i\Gamma)\mathbf{E}(\mathbf{x}, \tilde{\omega} + i\Gamma)d\mathbf{x}.\tag{4.29}$$

In summary, we can obtain the entire frequency-averaged LDOS by solving a single scattering problem (4.20) at a complex frequency $\tilde{\omega} + i\Gamma$.

We know that (4.26) gives a finite average LDOS because it decays fast enough with ω, but it is interesting to also consider how it fixes the divergence from the second viewpoint in section 4.5.1 (that of the infinite power absorption from a dipole in a lossy medium). The explanation is essentially that the second term in (4.29)

102

is roughly a subtraction of the divergent absorbed power from the first term: $\Gamma\varepsilon$ is $\omega\,\text{Im}(\tilde{\varepsilon})$ from section 4.5.1, and $\omega\,\text{Im}(\tilde{\varepsilon})|\mathbf{E}|^2$ is absorbed power [25]. (A subtlety arises from having $+\mathbf{E}^T\mathbf{E}$, rather than $-|\mathbf{E}|^2$, but the $1/r^3$ divergence at $r \to 0$ should be dominant in $\text{Im}(\mathbf{E})$ for small Γ so one should have $\mathbf{E}^T\mathbf{E} \approx -\text{Im}(\mathbf{E}^T)\,\text{Im}(\mathbf{E}) \approx -|\mathbf{E}|^2$ as $r \to 0$.)

Since the role of the second term in (4.29) is essentially to subtract off the divergent absorbed power in lossy $\tilde{\varepsilon}$ medium, and this divergence comes from the $1/r^3$ field divergence that is independent of geometries (the scattered field from the surrounding geometry is finite at $r = 0$), one might expect that the second term in (4.29) plays little role in geometry optimization at a fixed resolution. Indeed, we find in numerical experiments that the optimizations *with* and *without* the second terms in (4.29) for the 2d TE case (discussed in section 5.2) discover similar structures.

Therefore, in chapter 5 we optimize the simpler single Lorentzian objective of section 4.5.1, although eq. (4.29) is computationally feasible if it were needed.

4.6   A preliminary formulation

Now we have a preliminary formulation for our cavity optimization in terms of frequency averaged local density of states:

$$\max_{\{\text{designs}\}} L = \int_{-\infty}^{\infty} \text{LDOS}(\omega)W(\omega)\mathrm{d}\omega. \tag{4.30}$$

We can evaluate the objective L by contour integration, which only requires solving the complex scattering problem (4.20) once. If we choose the window function $W(\omega)$ from (4.26), then the problem can be reformulated as

$$\max_{\{\text{designs}\}} L = \Re\left[\ell = f(\tilde{\omega} + i\Gamma) - i\Gamma f'(\tilde{\omega} + i\Gamma)\right]. \tag{4.31}$$

Mathematically, to compute the objective in (4.31), we need

1. For given $\varepsilon(\mathbf{x})$, $\tilde{\omega}$ and Γ, solve the complex scattering problem (4.20) to obtain $\mathbf{E}(\mathbf{x}, \tilde{\omega} + i\Gamma)$.

103

2. Obtain ℓ from the solution $\mathbf{E}(\mathbf{x}, \tilde{\omega} + i\Gamma)$ through the formula (4.29).

3. take the real part of ℓ to get L.

To speed up the optimization, we had better have the gradient of the objective or the sensitivity of the objective to the design parameter ε_k, which is the dielectric constant at $\mathbf{x} = \mathbf{x}_k$. It turns out that with the standard technique of adjoint method [113], one more solving for the same operator $\tilde{\mathcal{M}}(\varepsilon, \tilde{\omega})$ with a different source term is sufficient to get all the gradient information. We put the detailed calculation in the appendix B.4 and summarize the procedure here:

1. Solve the complex scattering problem

$$\tilde{\mathcal{M}}(\varepsilon, \tilde{\omega})\mathbf{A}(\mathbf{x}, \tilde{\omega} + i\Gamma) = \varepsilon(\mathbf{x})\mathbf{E}(\mathbf{x}, \tilde{\omega} + i\Gamma) \tag{4.32}$$

to obtain $\mathbf{A}(\mathbf{x}, \tilde{\omega} + i\Gamma)$.

2. The sensitivity $\partial\ell/\partial\varepsilon_k$ is a combination of $\mathbf{E}(\mathbf{x}, \tilde{\omega} + i\Gamma)$ and $\mathbf{A}(\mathbf{x}, \tilde{\omega} + i\Gamma)$, and can be obtained from the formula (see appendix B.4 for details)

$$\begin{aligned}
\frac{\partial\ell}{\partial\varepsilon_k} = \left(i + \frac{1}{Q}\right)\frac{2}{\pi}\tilde{\omega}\mathbf{E}^T(\mathbf{x}_k, \tilde{\omega} + i\Gamma)\mathbf{E}(\mathbf{x}_k, \tilde{\omega} + i\Gamma) \\
+ \frac{12}{\pi}\frac{\tilde{\omega}^3}{\tilde{Q}}\left(1 + \frac{i}{2\tilde{Q}}\right)\mathbf{A}^T(\mathbf{x}_k, \tilde{\omega} + i\Gamma)\mathbf{E}(\mathbf{x}_k, \tilde{\omega} + i\Gamma). \tag{4.33}
\end{aligned}$$

3. Take the real part of $\partial\ell/\partial\varepsilon_k$ to have $\partial L/\partial\varepsilon_k$.

Note that the scattering operator (4.32) in the sensitivity analysis is the same as the operator in the objective evaluation. We can take advantage of this by reusing the information (e.g., preconditioner or LU factorization) from the solution of eq. (4.20). We will discuss this in detail in section 4.7.1.

4.7   Numerical scheme for cavity optimization

In this section, we discuss the numerical implementation for our frequency-averaged LDOS formulation given in section 4.6. In order to solve this PDE-constrained op-

timization problem computationally, we need fast and efficient implementations for objective evaluation, gradient evaluation, and optimization.

4.7.1   Objective and gradient evaluation

As we discussed in section 4.6, evaluating the objective LDOS is essentially equivalent to solving the scattering problem (4.20). We can apply any standard frequency-domain solver technique to this problem (e.g., finite difference, finite element, or boundary element method). Here we simply adopt the finite difference approach. If we impose mirror planes in the system, we can obtain an 8 times reduction (see figure 5-7).

For the finite difference frequency domain (FDFD) scattering, the most robust solver is a sparse-direct solver, which is excellent in 2d, but expensive (in both memory and time) in 3d. In contrast to direct solvers, the iterative solvers (e.g., GMRES and BiCGStab) work quite well if we have a good preconditioner. Unfortunately, it is hard to precondition for wave-propagation (Helmholtz-like) problem. But during the optimization, we resolve many times for slightly different structures. Therefore, we can use sparse-direct factorization from one step as a preconditioner for iterative solvers in following many steps. Here is an outline for our FDFD solver:

1. In the first 100 optimization steps, solve the scattering problem with sparse-direct solver.

2. After 100 steps, first try iterative solver with 15 iterations and with the preconditioner from the LU factorization in the previous sparse-direct solving.

   (a) If the iterative solver converges within 15 steps, then go to the next optimization step.

   (b) Otherwise, solve the problem with sparse direct solver and store the LU factorization information as a preconditioner for next step.

We implemented the FDFD scattering solver with fast parallel sparse-matrix library PETSc [8, 9, 10] and parallel sparse-direct solver PaStiX [48]. It turns out that

105

moderate resolution problems are solvable on workstations and large systems are solvable on parallel supercomputers. For example, for a computational cell $90 \times 90 \times 45$ (corresponding matrix size 2 million by 2 million, since real and imaginary part of $\mathbf{E}$ fields stored separately), it takes 1.5 minutes for symbolic factorization and 2.5 minutes for numerical factorization on supercomputer Kraken with 250 (2.6 GHz) processors. For the same problem, 15 iterations with iterative solver takes less than 25 seconds. From our experience, in the late optimization stages, it only needs to perform one sparse-direct factorization for every 30–100 steps.

For the gradient evaluation, it is equivalent to solving the same scattering problem with a different source term $\varepsilon(\mathbf{x})\mathbf{E}(\mathbf{x}, \tilde{\omega} + i\Gamma)$ instead of $\mathbf{J}(\mathbf{x})$, as described in appendix B.4. Therefore the preconditioner for the objective will work equally well for this gradient evaluation.

4.7.2 Optimization scheme

There are many gradient-based optimization algorithms we can use, for example, the quasi-Newton algorithm LBFGS [71] and conservative convex separable approximation (CCSA) methods [115]. However, if we apply these optimization methods directly, we typically observed slow or stalled convergence for $Q > 1000$.

Let's look at our objective LDOS more closely. From eq. (B.8), we have a rough estimate of the LDOS(ω) when ω is near the resonance ω_n

$$\text{LDOS}(\omega) \approx \frac{3}{\pi} |\mathbf{E}^n(\mathbf{x}') \cdot \hat{\mathbf{e}}_j|^2 \frac{\text{Im}[\omega_n]}{(\omega - \Re[\omega_n])^2 + (\text{Im}[\omega_n])^2}. \tag{4.34}$$

From this expression, LDOS(ω) behaves near resonance like a Lorentzian with bandwidth $1/Q$, since $\text{Im}[\omega_n]$ is proportional to $1/Q$. LDOS(ω) is therefore a narrow ridge along some manifold in the parameter space (see figure 4-2 for a simple two-parameter schematic illustration). Moving off of this ridge is equivalent to shifting the resonant frequency away from ω. For optimization, we wish to move *along* the ridge in order to find the highest point (the best LDOS within the manifold corresponding to a given resonant mode). Unfortunately, it is well known that optimizing

106
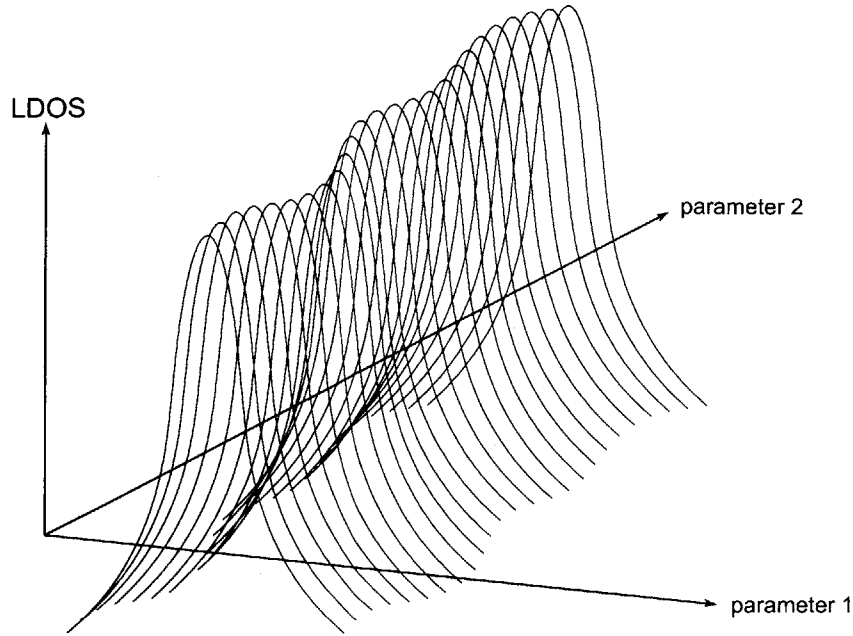
Figure 4-2: Illustration of LDOS(ω) in two parameter space. When ω is near resonance, LDOS(ω) looks like a narrow ridge (sharply peaked Lorentzian) along some curves with ups and downs.

an objective with a narrow ridge without exploiting second-derivative information tends to zigzag, moving back and forth perpendicular to the ridge [86]. Therefore, the convergence may be extremely slow. Quasi-Newton methods estimate the second derivatives precisely to deal with such problems, but for Q reaches 1000 or so, the standard quasi-Newton methods are not good enough, because of the huge Hessian, which is of order Q^3 (see appendix B.5 for the estimation). That is, the Hessian matrix is becoming ill-conditioned, which seems to cause numerical difficulties for Newton schemes. We could incorporate this asymptotic approximation for the Hessian into a special-purpose optimization algorithm. However, it turns out that there is an even simpler solution: a transformation from maximizing LDOS to minimizing 1/LDOS:

$$\max_{\{\text{designs}\}} L = \int_{-\infty}^{\infty} \text{LDOS}(\omega)W(\omega)d\omega \iff \min_{\{\text{designs}\}} \frac{1}{L} = \frac{1}{\int_{\infty}^{\infty} \text{LDOS}(\omega)W(\omega)d\omega} \quad (4.35)$$

Clearly, they are equivalent since LDOS is strictly positive. We know that LDOS is sharply peaked in a narrow region when Q is large (figure 4-3a). Once the transfor-
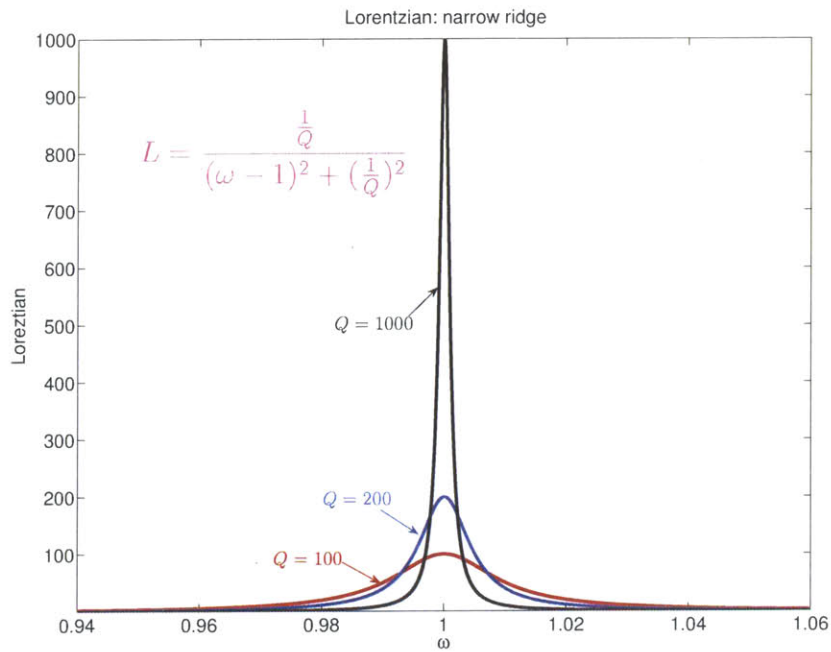
(a) Small-bandwidth Lorentzians (narrow ridges).
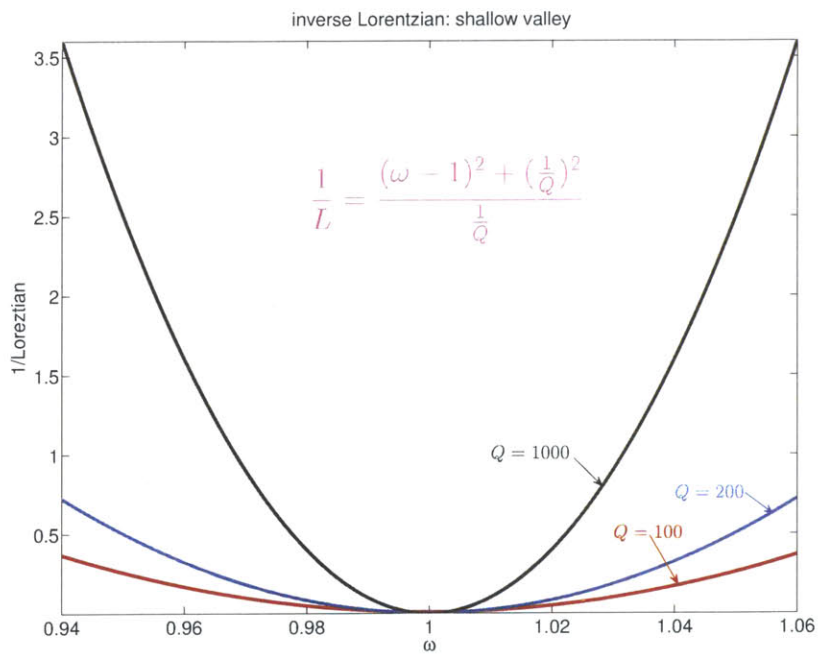
(b) Inverse of small-bandwidth Lorentzians (shallow valleys).

Figure 4-3: The illustration of Lorentzians with narrow bandwidth [figure (a)] and its inverse [figure (b)]. The transformation (taking the inverse) changes the objective from narrow ridges to shallow valleys.

mation is applied, the new objective becomes a shallow valley (figure 4-3b), which is easier to optimize. For example, in the 2d TM optimization to be discussed in section 5.1, because the quality factor Q of the initial guess (a photonic crystal cavity) is very high (order of 10^7), maximizing L does not make any improvement while minimizing $1/L$ does.

Chapter 5

Results for cavity optimization

In this chapter, we present some 2d and 3d results from the cavity optimization schemes developed in previous sections. We start with high-resolution 2d cases, and run simulations with different initial guess (vacuum, photonic crystal with a defect and random structures) and different dipole polarizations (TM, TE and random). In the region to be optimized, we allow each pixel to be one degree of freedom (figure 5-1a). For 2d TE case, the optimization discovers similar structures for maximizing the spontaneous emission rate of a *specific* dipole polarization and a *randomly* polarized dipole. In another scenario of 2d, to get the Q versus V trade off analogues to 3d, we limit the degrees of freedom in one direction and choose a thin strip, instead of a square, as the region for optimization (figure 5-1b). We also use this thin strip case to study the relationship between Q and the degrees of freedom. As the degrees of freedom increases, the radiation Q first increases and then becomes saturated, which may be limited by the numerical precision in the computation. Finally, we ran the 3d optimization on supercomputer and obtained a structure with quality factor $Q = 30000$ and extremely small mode volume $V = 0.06(\lambda/n)^3$.

5.1   2D TM case

In this section, we want to maximize the spontaneous emission rate of a dipole with TM polarization (out of plane) in a 2d setting (figure 5-1a). One popular candidate for

(a) A square region for degrees of free- (b) A thin strip region for degrees of
dom.   freedom.
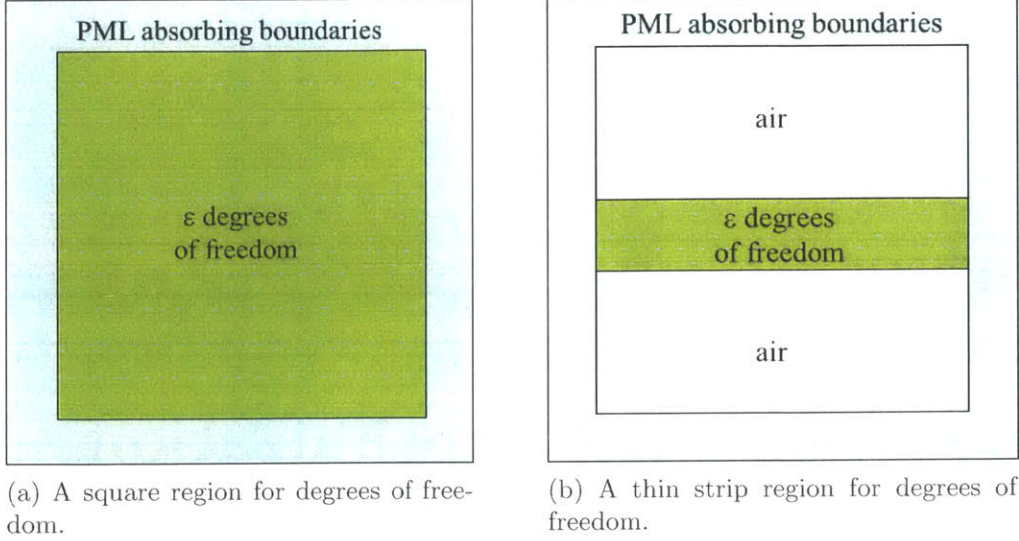
Figure 5-1: Sketch of regions for degrees of freedom.

such applications is a photonic crystal with a defect, like the one shown in figure 5-2a. It is a periodic arrangement (periodicity a) of dielectric silicon rods (radius $0.2a$ and permittivity $\varepsilon = 12.4$) with one defect rod at the center (radius $0.1a$). The defect TM mode is at frequency $0.32(2\pi/a)$, with quality factor Q=1.41e+8 and mode volume $V = 0.097(\lambda/n)^2$. With this structure as an initial guess, we run the optimization and obtain a nested ring structure (figure 5-2b) with quality factor Q=1.01e+10 and mode volume $V = 0.075(\lambda/n)^2$. Clearly, the optimization itself discovers a periodic structure with periodicity in radial direction, reminiscent of a Bragg onion [129] . We also run the optimization with vacuum as initial guess and obtain similar structure (figure 5-3) with Q=1.30e+9 and $V = 0.075(\lambda/n)^2$.

In these two optimizations, we gradually increase the absorption $\tilde{Q}$ (or decrease the bandwidth $1/\tilde{Q}$) from 1e+1 to 1e+5. The optimization at $\tilde{Q}$=1e+1 actually gives a high Q cavity (almost the same radiation Q) with the resonance at about $1.003\tilde{\omega}$. The optimizations at higher $\tilde{Q}$ simply tune this structure so that the resonant frequency becomes much closer to $\tilde{\omega}$.

Note that in the optimization scheme, we allow the dielectric permittivity of each pixel to vary continuously from $\varepsilon_{\min} = 1.0$ to $\varepsilon_{\max} = 12.4$, but almost all the pixels (except few ones in the interfaces) are at either $\varepsilon_{\min}$ or $\varepsilon_{\max}$ in the optimized struc-
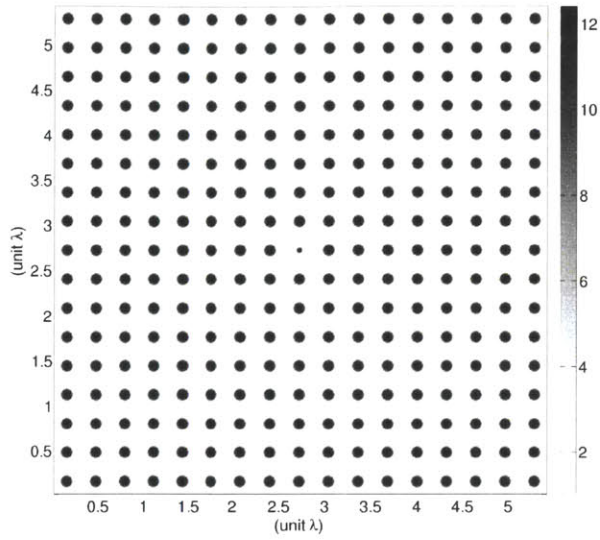
(a) PhC cavity initial guess for 2d TM optimization. It has quality factor $Q=1.41e+8$ and mode volume $V = 0.097(\lambda/n)^2$.
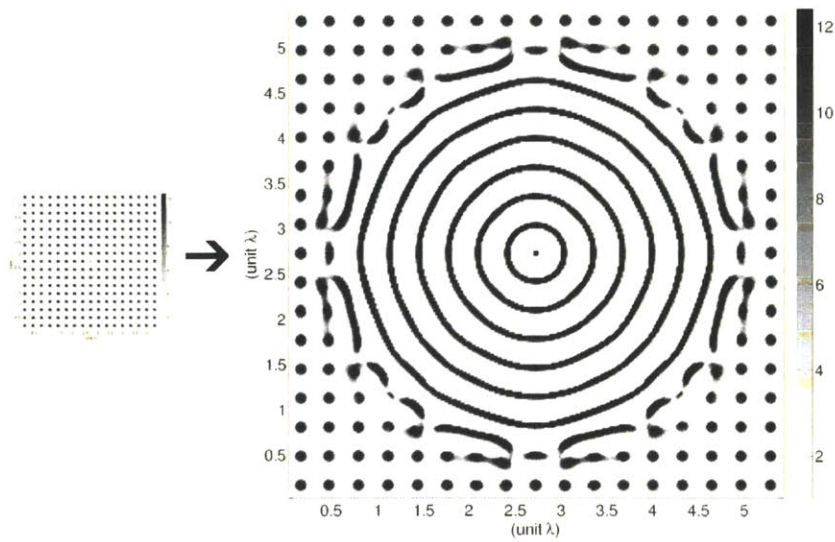
(b) 2d TM optimized structure: $Q=1.01e+10$ and $V = 0.075(\lambda/n)^2$.

Figure 5-2: 2d TM optimization from PhC cavity initial guess.
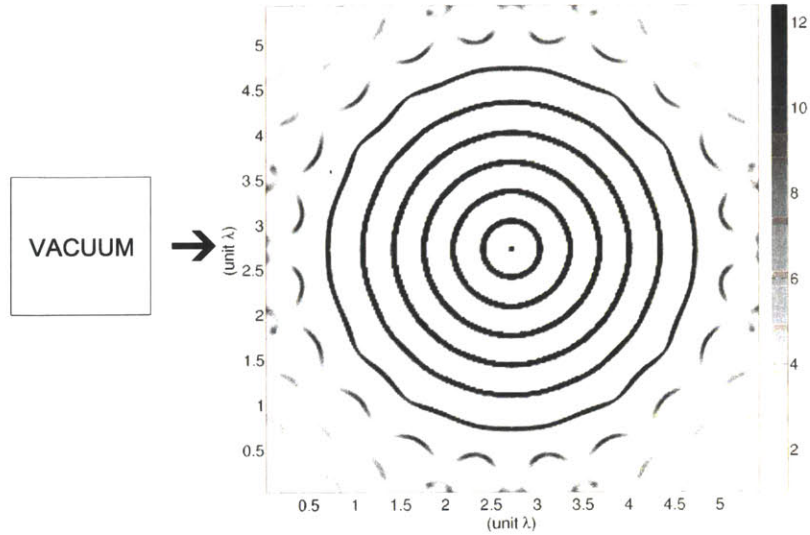
Figure 5-3: 2d TM optimization from vacuum initial guess. Q=1.30e+9 and $V = 0.075(\lambda/n)^2$.

ture. This phenomenon (reminiscent of "bang-bang" problems in control theory) had also been observed in other cavity-related optimization work. Not only has a similar phenomenon been observed empirically in topology optimization for electromagnetism [13, 74, 94], but there has been some recent progress in proving theoretically that this is the expected solution. In particular, Ref. [95] recently analyzed optimization problems for scalar waves, and showed that maximizing an energy confinement time over the permittivity at every point in space generally leads to a solution in which the permittivity is either the maximum or the minimum allowed value at every point, excepting a set of measure zero (at the interfaces between regions).

5.2   2D TE case

In this section, we consider the 2d TE polarization. Let us first look at the case where the dipole is polarized in the $\hat{e}_x$ direction. In other words, we want to maximize LDOS$(\omega; \hat{e}_x)$. From a vacuum initial guess, the optimization discovers the structure shown in figure 5-4a. This structure has quality factor Q=5.16e+8 and mode volume $V = 0.092(\lambda/n)^2$. [Again, the $\tilde{Q}$=1e+1 gives an equally high Q cavity with resonant

frequency at $1.0007\tilde{\omega}$. The optimizations at higher $\tilde{Q}=1e+2$ to $1e+5$ simply tune the resonant frequency to $\tilde{\omega}$.] Clearly, if we optimize the $\hat{e}_y$ polarization case, we get a structure like figure 5-4b, just a $90°$ rotation of the structure from $\hat{e}_x$-polarization optimization.

5.2.1 Optimization for a randomly polarized dipole

We just considered the dipole polarization in a specific direction $\hat{e}_x$ or $\hat{e}_y$. Now we want to study the case in which the dipole is randomly polarized in the plane. Naively, one might expect the optimization to find a symmetric structure in this case. It is easy to show [90, problem 8.6] that maximizing the LDOS for a random polarization by averaging all polarizations is equivalent to maximizing the sum of $\hat{e}_x$ and $\hat{e}_y$ polarizations, namely $\max[\text{LDOS}(\omega; \hat{e}_x) + \text{LDOS}(\omega; \hat{e}_y)]$. For this new objective, we ran 10 different simulations with different random initial guess (each pixel is randomly chosen between ε_{min} and ε_{max}). We found that 4 out of 10 give similar structure as $\hat{e}_x$ polarization (figure 5-4a), while 6 out of 10 give structures similar to $\hat{e}_y$ polarization (figure 5-4b). From these results, it seems that the optimization, instead of favoring both $\hat{e}_x$ and $\hat{e}_y$ polarization simultaneously, simply randomly picks one direction and optimizes it. That is, there is a *spontaneous symmetry breaking*: it is better to optimize one polarization at the expense of the other than to try to obtain a doubly degenerate cavity that resonates for both polarizations. Apparently, the LDOS of the best single-polarization (non-degenerate) cavity is more than twice as big as the LDOS of the best doubly degenerate cavity—an interesting result!

Another interesting case would be maximizing the minimum (instead of the sum) of LDOS at these two polarizations, namely, $\max\min(\text{LDOS}(\omega; \hat{e}_x), \text{LDOS}(\omega; \hat{e}_y))$ and we conjecture that this objective might give a symmetric (C_{4v}) structure. We will study this case in future work.
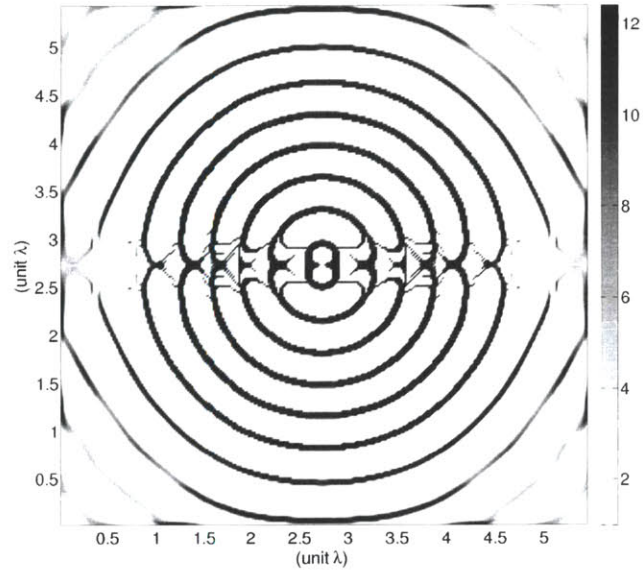
(a) Optimized structure for $\hat{e}_x$ polarization.
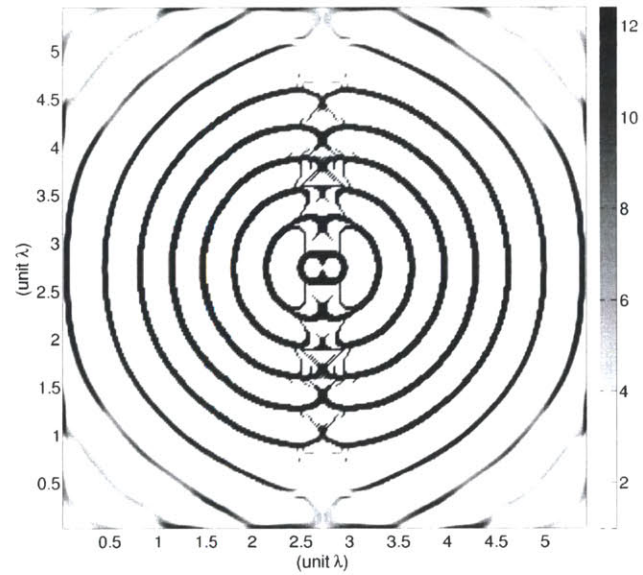
(b) Optimized structure for $\hat{e}_y$ polarization.

Figure 5-4: 2d TE optimization for $\hat{e}_x$ [figure (a)] and $\hat{e}_y$ [figure (b)] polarizations. The structures have Q=5.16e+8 and $V = 0.092(\lambda/n)^2$.

116

5.3   2D TE thin strip case

In previous 2d TM and TE polarization cases, we expect and obtain almost no Q versus V trade off since the cavity can be surrounded by complete photonic bandgap or a Bragg onion. In 2d setting, to get the Q versus V trade off analogues to 3d slabs, we need to limit the degrees of freedom in one direction in order to force the possibility of radiation loss. In this section, we choose the region for degrees of freedom as a thin strip (figure 5-1b). In a region with dimensions 5λ-by-1λ, we obtain a structure (figure 5-5) with quality factor Q=1.00e+7 and mode volume $V = 0.056(\lambda/n)^2$. [The absorption $\tilde{Q}$ used in the optimization is gradually increased from 1e+1 to 1e+6.]
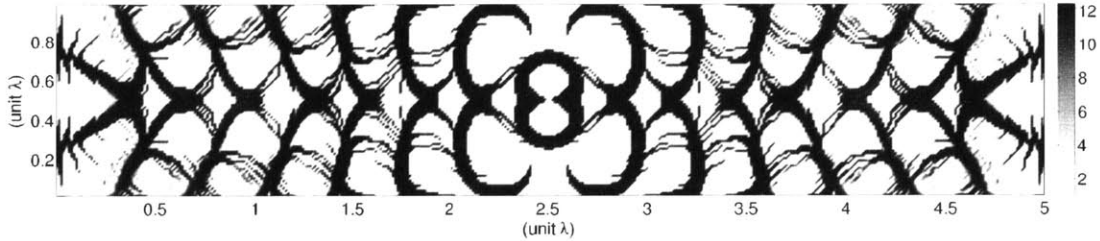
Figure 5-5: 2d TE thin strip optimization: Q=1.00e+7 and $V = 0.056(\lambda/n)^2$. Different from previous 2d TE optimization, here the degrees of freedom are limited in one dimension.

As we discussed in section 4.4.3, if we add absorption loss with quality factor $\tilde{Q}$ into the system, the optimization will not benefit from making $Q_{\mathrm{rad}} \gg \tilde{Q}$ and therefore Q_{rad} is effectively bounded. Therefore, if we increase $\tilde{Q}$ in the optimization, we expect higher and higher Q_{rad} until Q_{rad} is limited by the degrees of freedom (figure 5-6). Then another interesting question to ask is as we increase the degrees of freedom, will we get higher and higher Q_{rad}? In theory, it is possible as in the example of a slowly tapering structure [80, 81, 82]. In our numerical experiment, we found that as we increase the degrees of freedom, Q_{rad} first gets higher and higher, but becomes saturated at some level around 10^7 (figure 5-6). It may be due to the finite numerical precision in the computation, particularly in solving large linear system. [Note that the data in figure 5-6 are from the optimization result for the objective $\varepsilon(\mathbf{x}')\mathrm{LDOS}(\omega, \mathbf{x}')$, which is proportional to Q/V, since $\mathrm{LDOS}(\omega, \mathbf{x}')$ is proportional to $Q/\varepsilon(\mathbf{x}')V$ given in equation B.8.]
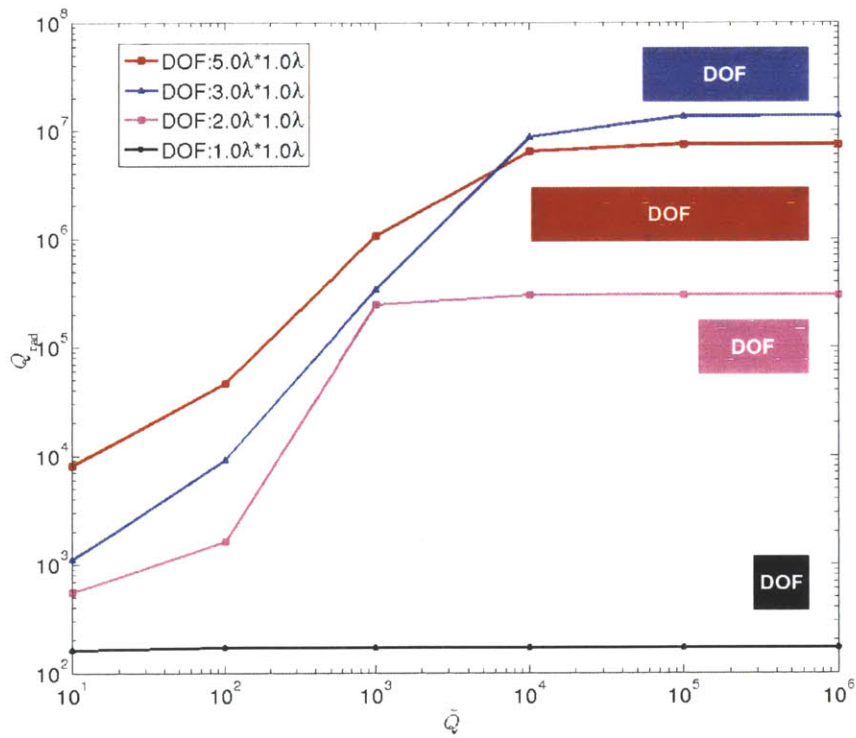
Figure 5-6: Q_{rad} vs $\tilde{Q}$ for different Degrees of Freedom (DOF). As we increase $\tilde{Q}$ in the optimization, higher Q_{rad} are obtained until Q_{rad} is limited by the degrees of freedom. As the degrees of freedom increase, Q_{rad} first gets higher, but becomes saturated at some level around 10^7 due to numerical precision.

5.4 3D case

(a) Sketch of the region for degrees of freedom in 3d slab.

(b) Sketch for 3d slab computational domain (with mirror-symmetry imposed).
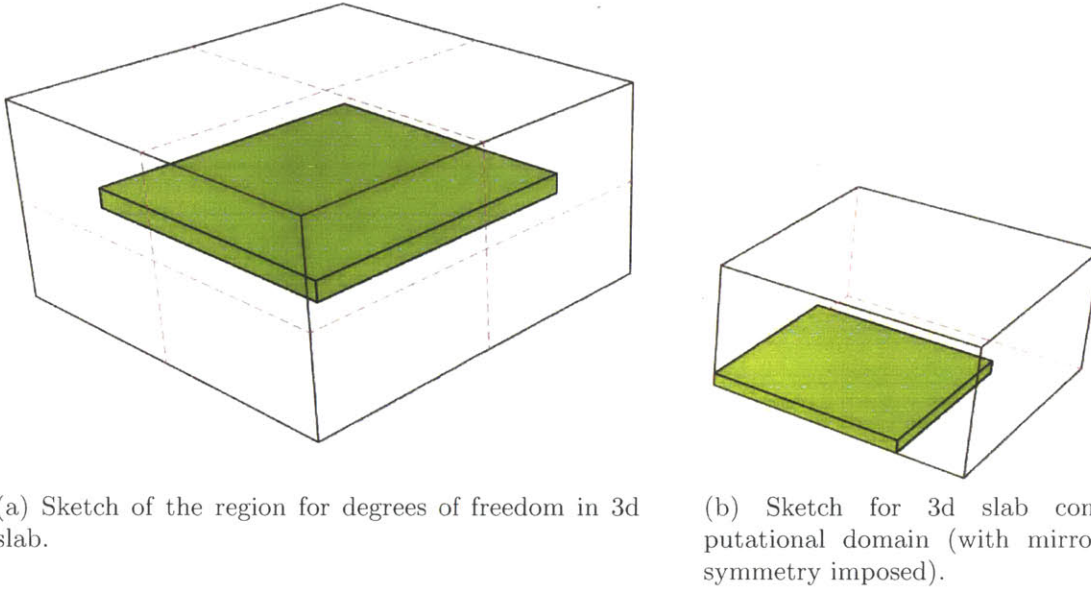
Figure 5-7: Sketch for 3d slab optimization: physical model and computational domain.

With the computation and optimization tools developed in previous sections, we run large-scale simulations on 3d slab case (with in-plane polarization). Here we choose the dimensions of the slab to be 3λ-3λ-0.19λ, where the thickness is 0.19λ. A sketch of the physical model is shown in figure 5-7a, and the real computation domain (with mirror symmetry reductions) is illustrated in figure 5-7b. The optimization discovers a structure (figure 5-8) with quality factor $Q=30000$ and extremely small mode volume $V = 0.06(\lambda/n)^3$. [This result is obtained from optimizations with absorption $\tilde{Q}$ gradually increasing from 1e+1 to 1e+4. The optimization discovers structures with radiation $Q=1.18e+4$ at $\tilde{Q}=1e+2$, with radiation $Q=2.55e+4$ at $\tilde{Q}=1e+3$, and with radiation $Q=2.98e+4$ at $\tilde{Q}=1e+4$.]

A comparison with other large- or small-scale optimization work, such as 2.5d optimization [74], L_3-type cavity [5] and H_0-type cavity [89] optimization are given in table 5.1. Clearly, the optimization was able to achieve four times smaller mode volume than the smallest mode volume (at the same order of Q) we found in the literature [89].

119
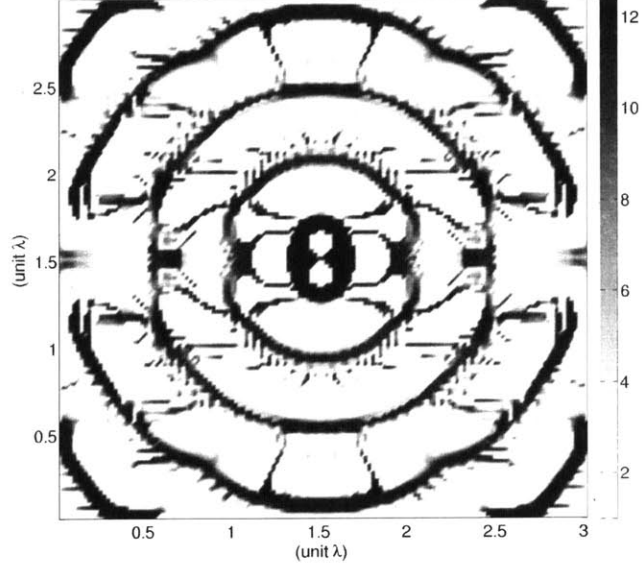
Figure 5-8: Optimized pattern for a 3d slab with dimensions 3λ-3λ-0.19λ: Q=30000 and $V = 0.06(\lambda/n)^3$.

Optimization	Quality Factor Q	Mode Volume V $(\lambda/n)^3$
2.5d optimization	8000	0.32
L_3-type cavity optimization	100000	0.70
H_0-type cavity optimization	280000	0.23
LDOS optimization	30000	0.06

Table 5.1: Comparison of Q and V for structures from various optimizations.

5.4.1 Post-processing to remove tiny features

Note that in the optimized structure, there are some tiny hair/fingers, which make the fabrication difficult. As a first try, we manually remove some small features by hand and have a structure (figure 5-9) with $Q = 10000$ and roughly same V. Comparing these two structures, it seems that we had removed some important connecting bridges, which affects the Q. Instead of post-processing the structure, we will consider suppress these tiny (one- or two- pixel) features by new algorithm (such as filters or global regularization [53]) in future work.
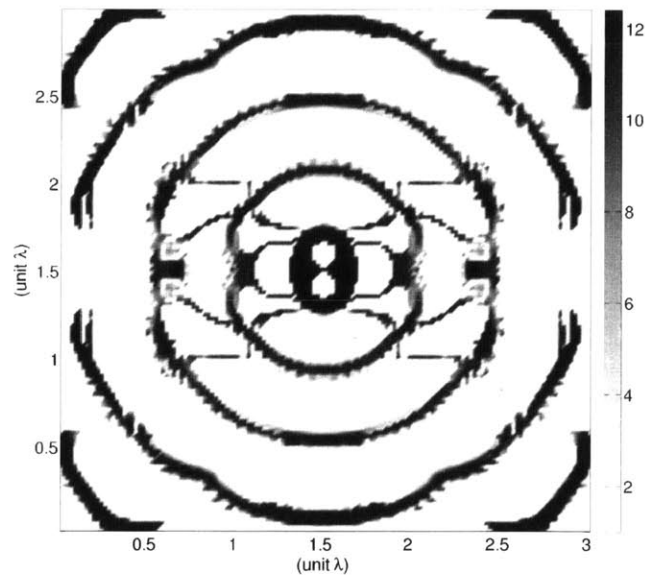
Figure 5-9: 3d slab structure after manually removing tiny features: $Q = 10000$ and $V = 0.06(\lambda/n)^3$.

5.4.2 Comparison with air-slot cavity

All these cavities listed in table 5.1 are dielectric cavities. In other words, the centers of these cavities are high-dielectric materials (Si and GaAs) and these cavities are useful for dipoles/emitters lying in these materials. It is also reflected in the unit of mode volume. For example, the mode volume of the cavity we obtain is $V = 0.06(\lambda/n)^3 = 0.06(\lambda/n_{Si})^3$.

It is known that air-slot cavities [59, 65, 88, 103] have extremely small volumes. For example, Ref. [88] reported an air-slot cavity with Q=4.8e+6 and $V = 0.015(\lambda/n_{\text{air}})^3$. Although 0.015 is smaller than 0.06, these two kinds of cavities are not comparable in two ways. First, the two mode volumes are in different units $(\lambda/n_{\text{air}})^3$ versus $(\lambda/n_{\text{Si}})^3$. Second, these two types of cavities are for different applications: air-slot cavities are useful for emitters lying in air, while the semiconductor-based cavities are designed for emitters lying in Si and GaAs.

If the application is for emitters lying in air, in theory, we can also introduce an infinitesimal air-slot, at the center oriented perpendicular to the electric field, into our structure. As discussed in Ref. [103], after the introduction of an air-slot, the unitless mode volume decreases by a factor of $(n_{\text{Si}}/n_{\text{air}})^5$. [In our case, this factor is about 541, and the new mode volume is $1.1\text{e-}4(\lambda/n_{\text{air}})^3$.] Because the resolution we used (46-pixel per wavelength in air) is not that high, the optimization discovers a dielectric cavity, instead of one with air-slot type. In future work, we will run the optimizations with high resolutions (at least in 2d cases) to investigate whether air-slot structures can be discovered.

In summary, we obtained promising results for heavily studied silicon slabs in infrared, for which various small-parameter hand optimizations had been performed for more than 20 years. If our large-scale optimization is applied to less studied material regimes, e.g. metal-coated dielectrics (surface plasmon modes), or lower-index materials for visible light (weak or no 2d photonic bandgaps [54] to build off of), the potential gains seem even greater.

Appendix A

Appendix for capillary instability

A.1 Computations of the curvature

Here we derive the curvature terms in (2.25). The level-set function $\phi^{(n)}(r, z, t) = 0$ corresponds to the n-th interface. The unit outward normal vector of this interface is

$$\boldsymbol{n}^{(n)} = (n_r^{(n)}, n_z^{(n)}) = \frac{\boldsymbol{\nabla}\phi^{(n)}}{|\boldsymbol{\nabla}\phi^{(n)}|} = \frac{\left(\frac{\partial\phi^{(n)}}{\partial r}, \frac{\partial\phi^{(n)}}{\partial z}\right)}{\sqrt{\left(\frac{\partial\phi^{(n)}}{\partial r}\right)^2 + \left(\frac{\partial\phi^{(n)}}{\partial z}\right)^2}} = \frac{(1, -\mathrm{i}k\delta R^{(n)}\mathrm{e}^{\mathrm{i}(kz-\omega t)})}{\sqrt{1 + O[(\delta R^{(n)})^2]}} \quad \text{(A.1)}$$

and the unit tangential vector is

$$\boldsymbol{t}^{(n)} = (n_z^{(n)}, -n_r^{(n)}) = \frac{(-\mathrm{i}k\delta R^{(n)}\mathrm{e}^{\mathrm{i}(kz-\omega t)}, -1)}{\sqrt{1 + O[(\delta R^{(n)})^2]}}. \quad \text{(A.2)}$$

The curvature $\kappa^{(n)}$ can now be computed as

$$\begin{aligned}
\kappa^{(n)} = \boldsymbol{\nabla} \cdot \boldsymbol{n}^{(n)} &= \frac{\partial n_r^{(n)}}{\partial r} + \frac{n_r^{(n)}}{r} + \frac{\partial n_z^{(n)}}{\partial z} \\
&= \frac{1}{\sqrt{1 + O[(\delta R^{(n)})^2]}} \frac{1}{R^{(n)} + \delta R^{(n)}\mathrm{e}^{\mathrm{i}(kz-\omega t)}} + \frac{\delta R^{(n)}k^2\mathrm{e}^{\mathrm{i}(kz-\omega t)}}{\sqrt{1 + O[(\delta R^{(n)})^2]}} + O\left[(\delta R^{(n)})^2\right] \\
&= \frac{1}{R^{(n)}} + \delta R^{(n)}\left(k^2 - \frac{1}{(R^{(n)})^2}\right)\mathrm{e}^{\mathrm{i}(kz-\omega t)} + O\left[(\delta R^{(n)})^2\right].
\end{aligned}$$

$$\text{(A.3)}$$

The normal velocity of the fluids on the interface must equal to the normal velocity of that interface, and thus $\frac{\partial \zeta^{(n)}}{\partial t} = \boldsymbol{u}^{(n)} \cdot \boldsymbol{n}^n$ on the interface $r = \zeta^{(n)}(z,t)$, where $\boldsymbol{u}^{(n)}$ is the velocity vector. For the at-rest steady state (2.8) and (2.9), to the lowest order in δR, this gives

$$-i\omega \delta R^{(n)} = \delta u_r^{(n)}(R^{(n)}).$$

(A.4)

Note that (A.4) establishes the relation between the displacement amplitude $\delta R^{(n)}$ and the interface velocity $\delta u_r^{(n)}(R^{(n)})$. Substituting (A.4) into (A.3), we obtain the lowest-order curvature $\kappa^{(n)}$ in terms of the interface velocity $\delta u_r^{(n)}(R^{(n)})$:

$$\kappa^{(n)} = \frac{1}{R^{(n)}} + \frac{\delta u_r^{(n)}(R^{(n)})}{-i\omega}\left(k^2 - \frac{1}{(R^{(n)})^2}\right) e^{i(kz-\omega t)}.$$

(A.5)

Appendix B

Appendix for cavity optimization

B.1   LDOS, Purcell factor and Q/V

In this section, we are going to review the relationship between $\text{LDOS}(\omega)$ given in eq. (4.12) and Purcell factor in eq. (4.4) [42, 60].

First, let us construct the scattering solution $\mathbf{E}(\mathbf{x})$ from the eigenfunctions. For a dielectric structure $\varepsilon(\mathbf{x})$, we assume that there is a complete orthonormal basis of eigenfunctions $\mathbf{E}^n(\mathbf{x})$:

$$\nabla \times \frac{1}{\mu(\mathbf{x})}\nabla \times \mathbf{E}^n(\mathbf{x}) = \omega_n^2 \varepsilon(\mathbf{x})\mathbf{E}^n(\mathbf{x}), \tag{B.1}$$

where $\int \varepsilon(\mathbf{x})\mathbf{E}^{n^*}(\mathbf{x})\mathbf{E}^m(\mathbf{x}) = \delta_{nm}$. Now we expand the scattering solution $\mathbf{E}(\mathbf{x})$ and dipole current $\mathbf{J}(\mathbf{x}) = \delta(\mathbf{x} - \mathbf{x}')\hat{\mathbf{e}}_j$ in terms of eigenfunctions

$$\mathbf{E}(\mathbf{x}) = \sum_{n=1}^{\infty} d_n \mathbf{E}^n(\mathbf{x}) \tag{B.2}$$

$$\delta(\mathbf{x} - \mathbf{x}')\hat{\mathbf{e}}_j = \sum_{m=1}^{\infty} (\mathbf{E}^{m^*}(\mathbf{x}') \cdot \hat{\mathbf{e}}_j)\varepsilon(\mathbf{x})\mathbf{E}^m(\mathbf{x}). \tag{B.3}$$

To determine the unknown coefficient d_n, we substitute (B.2) and (B.3) into the

125

scattering equation (4.10) and obtain

$$d_n = \frac{i\omega(\mathbf{E}^{n^*}(\mathbf{x}') \cdot \hat{\mathbf{e}}_j)}{\omega_n^2 - \omega^2}. \tag{B.4}$$

Therefore we have

$$\int \mathbf{J}^*(\mathbf{x}) \cdot \mathbf{E}(\mathbf{x})d\mathbf{x} = \hat{\mathbf{e}}_j^* \cdot \mathbf{E}(\mathbf{x}')$$

$$= \sum_{n=1}^{\infty} d_n \hat{\mathbf{e}}_j^* \cdot \mathbf{E}^n(\mathbf{x}') = \sum_{n=1}^{\infty} \frac{i\omega}{\omega_n^2 - \omega^2} |\mathbf{E}^n(\mathbf{x}') \cdot \hat{\mathbf{e}}_j|^2$$

$$= \sum_{n=1}^{\infty} \left(\frac{1}{\omega - \omega_n} + \frac{1}{\omega - (-\omega_n)} \right) \frac{-i|\mathbf{E}^n(\mathbf{x}') \cdot \hat{\mathbf{e}}_j|^2}{2} \tag{B.5}$$

$$= \sum_{n=-\infty, n \neq 0}^{\infty} \frac{1}{\omega - \omega_n} \frac{-i|\mathbf{E}^n(\mathbf{x}') \cdot \hat{\mathbf{e}}_j|^2}{2}.$$

Note that in the last step we just relabel the eigenfrequencies by $\omega_{-n} = -\omega_n$.

For a resonant mode $\mathbf{E}^n(\mathbf{x})$, the radiation boundary condition implies that the eigenfrequency ω_n is complex and the corresponding quality factor Q is

$$Q = \frac{\Re[\omega_n]}{-2\,\text{Im}[\omega_n]}. \tag{B.6}$$

In other words,

$$\omega_n = \Re[\omega_n] \left(1 - \frac{i}{2Q} \right). \tag{B.7}$$

Therefore, from (4.3), (4.12), (B.5) and (B.7), we have

$$\text{LDOS}(\omega, \mathbf{x}') = -\frac{6}{\pi}\Re[\int \mathbf{J}^*(\mathbf{x}) \cdot \mathbf{E}(\mathbf{x})d\mathbf{x}] = -\frac{6}{\pi}\Re[\hat{\mathbf{e}}_j^* \cdot \mathbf{E}(\mathbf{x}')]$$

$$= -\frac{6}{\pi}\Re \left[\sum_n \frac{1}{\omega - \omega_n} \frac{-i|\mathbf{E}^n(\mathbf{x}') \cdot \hat{\mathbf{e}}_j|^2}{2} \right]$$

$$= \frac{3}{\pi} \sum_n |\mathbf{E}^n(\mathbf{x}') \cdot \hat{\mathbf{e}}_j|^2 \frac{\Re[\omega_n]/2Q}{(\omega - \Re[\omega_n])^2 + (\Re[\omega_n]/2Q)^2} \tag{B.8}$$

$$\approx \frac{3}{\pi}|\mathbf{E}^n(\mathbf{x}') \cdot \hat{\mathbf{e}}_j|^2 \frac{2Q}{\omega} = \frac{6Q}{\pi\omega} \frac{|\mathbf{E}^n(\mathbf{x}') \cdot \hat{\mathbf{e}}_j|^2}{\int \varepsilon(\mathbf{x}')|\mathbf{E}^n(\mathbf{x}')|^2 d\mathbf{x}'}$$

$$= \frac{6}{\pi\omega\varepsilon(\mathbf{x}')} \frac{Q}{V},$$

126

where the approximation is valid when Q is large and ω is near the resonance (ω is close to $\Re[\omega_n]$). We also assume that the polarization of the dipole $\hat{\mathbf{e}}_j$ is aligned with the resonant mode field $\mathbf{E}^n(\mathbf{x}')$.

Note that the Purcell factor is defined as the enhancement of the spontaneous emission decay rate in the cavity comparing to the one in the bulk material with refraction index n. From (4.7), we know that

$$\text{LDOS}_{\text{free}}(\omega) = \frac{6\omega}{\pi} \, \text{Im}[\hat{\mathbf{e}}_j \cdot \mathbf{G}_{\text{free}}(\mathbf{x}', \mathbf{x}') \cdot \hat{\mathbf{e}}_j] = \frac{2\omega}{\pi} \frac{n\omega}{6\pi} = \frac{n\omega^2}{\pi^2}. \tag{B.9}$$

Combining (B.8) and (B.9), we have

$$\frac{\text{LDOS}(\omega)}{\text{LDOS}_{\text{free}}(\omega)} = \frac{6Q}{\pi\omega\varepsilon(\mathbf{x}')V} \frac{\pi^2}{n\omega^2} = \frac{3}{4\pi^2} \frac{Q}{V} \left(\frac{\lambda}{n}\right)^3, \tag{B.10}$$

which is exactly the Purcell factor given in (4.4).

B.2   LDOS and Density of States

In this section, we verified that the integration of LDOS_j over all the polarization and the space gives the density of states [90].

The radiation boundary condition for (4.10) implies that no incoming waves from infinity or $\mathbf{E}(\mathbf{x}) \to 0$ at infinity. Mathematically, it is equivalent to add infinitesimal dissipation everywhere by $\varepsilon \to \varepsilon + i0^+$ and $\omega_n \to \omega_n - i0^+$. From distribution theory, we have

$$\lim_{\gamma \to 0^+} \frac{1}{\omega - (\omega_n - i\gamma)} = \lim_{\gamma \to 0^+} \frac{\omega - \omega_n}{(\omega - \omega_n)^2 + \gamma^2} - \frac{i\gamma}{(\omega - \omega_n)^2 + \gamma^2}$$
$$= \text{p.v.} \left\{ \frac{1}{\omega - \omega_n} \right\} - i\pi\delta(\omega - \omega_n), \tag{B.11}$$

where p.v. denotes the Cauchy principle value in the distribution sense. Combining

(B.5) and (B.11), we obtain

$$\Re\left[\int \mathbf{J}^*(\mathbf{x}) \cdot \mathbf{E}(\mathbf{x})\mathrm{d}\mathbf{x}\right] = \Re\left[\sum_n \frac{1}{\omega - \omega_n + i0^+} \frac{-i|\mathbf{E}^n(\mathbf{x}') \cdot \hat{\mathbf{e}}_j|^2}{2}\right]$$

$$= -\frac{\pi}{2}\sum_n |\mathbf{E}^n(\mathbf{x}') \cdot \hat{\mathbf{e}}_j|^2 \delta(\omega - \omega_n).$$

(B.12)

If the polarization of the dipole $\hat{\mathbf{e}}_j$ is randomly distributed in space, then

$$\text{average}_j \; |\mathbf{E}^n(\mathbf{x}') \cdot \hat{\mathbf{e}}_j|^2 = \frac{1}{3}|\mathbf{E}^n(\mathbf{x}')|^2.$$

(B.13)

Therefore,

$$\int \varepsilon(\mathbf{x}') \; \text{average}_j \; \text{LDOS}_j(\omega, \mathbf{x}')\mathrm{d}\mathbf{x}' = \int \varepsilon(\mathbf{x}') \; \text{average}_j \; \left(-\frac{6}{\pi}\right) \Re\left[\int \mathbf{J}^*(\mathbf{x}) \cdot \mathbf{E}(\mathbf{x})\mathrm{d}\mathbf{x}\right]\mathrm{d}\mathbf{x}'$$

$$= \int \varepsilon(\mathbf{x}') \sum_n |\mathbf{E}^n(\mathbf{x}')|^2 \delta(\omega - \omega_n)\mathrm{d}\mathbf{x}'$$

$$= \sum_n \delta(\omega - \omega_n) \int \varepsilon(\mathbf{x}')|\mathbf{E}^n(\mathbf{x}')|^2 \mathrm{d}\mathbf{x}'$$

$$= \delta(\omega - \omega_n)$$

(B.14)

B.3 Computation of $f'(\omega, \mathbf{x}')$

In this section, we will compute $f'(\omega, \mathbf{x}')$, the differentiation of $f(\omega, \mathbf{x}')$ given in equation (4.14) with respect to ω. Differentiating on both sides of (4.10), we have

$$\mathcal{M}(\varepsilon, \omega)\frac{\partial \mathbf{E}(\mathbf{x}, \omega)}{\partial \omega} + \frac{\partial \mathcal{M}(\varepsilon, \omega)}{\partial \omega}\mathbf{E}(\mathbf{x}, \omega) = i\mathbf{J}(\mathbf{x})$$

$$\Longrightarrow \frac{\partial \mathbf{E}(\mathbf{x}, \omega)}{\partial \omega} = \mathcal{M}^{-1}\left(i\mathbf{J}(\mathbf{x}) - \frac{\partial \mathcal{M}(\varepsilon, \omega)}{\partial \omega}\mathbf{E}(\mathbf{x}, \omega)\right) = \mathcal{M}^{-1}\left(i\mathbf{J}(\mathbf{x}) + 2\omega\varepsilon(\mathbf{x})\mathbf{E}(\mathbf{x}, \omega)\right).$$

(B.15)

128

Now differentiating on (4.14), we have

$$
\begin{aligned}
f'(\omega, \mathbf{x}') &= -\frac{6}{\pi} \int \mathbf{J}^*(\mathbf{x}) \frac{\partial \mathbf{E}(\mathbf{x}, \omega)}{\partial \omega} d\mathbf{x} \\
&= -\frac{6}{\pi} \left[\int \frac{1}{\omega} \mathbf{J}^*(\mathbf{x}) \mathcal{M}^{-1}(i\omega \mathbf{J}(\mathbf{x})) d\mathbf{x} + 2\omega \int \mathbf{J}^*(\mathbf{x}) \mathcal{M}^{-1} \varepsilon(\mathbf{x}) \mathbf{E}(\mathbf{x}, \omega) d\mathbf{x} \right] \\
&= -\frac{6}{\pi} \int \frac{1}{\omega} \mathbf{J}^*(\mathbf{x}) \mathbf{E}(\mathbf{x}, \omega) d\mathbf{x} + i\frac{12}{\pi} \int \left(\mathcal{M}^{-1}(i\omega \mathbf{J}(\mathbf{x})) \right)^T \varepsilon(\mathbf{x}) \mathbf{E}(\mathbf{x}, \omega) d\mathbf{x} \\
&= \frac{f(\omega, \mathbf{x}')}{\omega} + i\frac{12}{\pi} \int \varepsilon(\mathbf{x}) \mathbf{E}^T(\mathbf{x}, \omega) \mathbf{E}(\mathbf{x}, \omega) d\mathbf{x}.
\end{aligned}
$$

$$\text{(B.16)}$$

Note that we use the properties that $\mathcal{M}(\varepsilon, \omega)$ is complex symmetric ($\mathcal{M} = \mathcal{M}^T$) for both real and complex ω and $\mathbf{J}(\mathbf{x})$ is real ($\mathbf{J}^*(\mathbf{x}) = \mathbf{J}^T(\mathbf{x})$).

B.4 Computation of the objective and its gradient

In this section, we compute the objective $L = \Re\left[f(\tilde{\omega} + i\Gamma) - i\Gamma f'(\tilde{\omega} + i\Gamma) \right]$ defined in section 4.5.3 as well as its gradient. The gradient of the objective or the sensitivity of the objective to the design parameters are calculated with standard adjoint methods [113].

Let us denote its complex version by $\ell = f(\tilde{\omega} + i\Gamma) - i\Gamma f'(\tilde{\omega} + i\Gamma)$. From (4.14) and (4.28), we can simplify it as

$$
\begin{aligned}
\ell &= f(\tilde{\omega} + i\Gamma) - i\Gamma f'(\tilde{\omega} + i\Gamma) \\
&= f(\tilde{\omega} + i\Gamma) - i\Gamma \left(\frac{f(\tilde{\omega} + i\Gamma, \mathbf{x}')}{\tilde{\omega} + i\Gamma} + i\frac{12}{\pi} \int \varepsilon(\mathbf{x}) \mathbf{E}^T(\mathbf{x}, \tilde{\omega} + i\Gamma) \mathbf{E}(\mathbf{x}, \tilde{\omega} + i\Gamma) d\mathbf{x} \right) \\
&= \frac{\tilde{\omega}}{\tilde{\omega} + i\Gamma} f(\tilde{\omega} + i\Gamma) + \frac{12}{\pi} \Gamma \int \varepsilon(\mathbf{x}) \mathbf{E}^T(\mathbf{x}, \tilde{\omega} + i\Gamma) \mathbf{E}(\mathbf{x}, \tilde{\omega} + i\Gamma) d\mathbf{x}. \\
&= \frac{\tilde{\omega}}{\tilde{\omega} + i\Gamma} (-\frac{6}{\pi}) \hat{\mathbf{e}}_j^* \cdot \mathbf{E}(\mathbf{x}', \tilde{\omega} + i\Gamma) + \frac{12}{\pi} \Gamma \int \varepsilon(\mathbf{x}) \mathbf{E}^T(\mathbf{x}, \tilde{\omega} + i\Gamma) \mathbf{E}(\mathbf{x}, \tilde{\omega} + i\Gamma) d\mathbf{x}.
\end{aligned}
$$

$$\text{(B.17)}$$

In the rest of this section, we are going to compute the gradient of ℓ with respect to the design parameter ε_k, which is the dielectric constant at $\mathbf{x} = \mathbf{x}_k$. To obtain the

sensitivity of $\mathbf{E}(\mathbf{x}, \tilde{\omega} + i\Gamma)$ to ε_k, we differentiate (4.20) with respect to ε_k

$$
\tilde{\mathcal{M}}(\varepsilon, \tilde{\omega}) \frac{\partial \mathbf{E}(\mathbf{x}, \tilde{\omega} + i\Gamma)}{\partial \varepsilon_k} + \frac{\partial \tilde{\mathcal{M}}(\varepsilon, \tilde{\omega})}{\partial \varepsilon_k} \mathbf{E}(\mathbf{x}, \tilde{\omega} + i\Gamma) = 0
$$

$$
\implies \frac{\partial \mathbf{E}(\mathbf{x}, \tilde{\omega} + i\Gamma)}{\partial \varepsilon_k} = \tilde{\mathcal{M}}^{-1} \left[\tilde{\omega}^2 \left(1 + \frac{i}{2\tilde{Q}} \right) \delta(\mathbf{x} - \mathbf{x}_k) \mathbf{E}(\mathbf{x}, \tilde{\omega} + i\Gamma) \right].
$$

(B.18)

Therefore, from (4.14), (4.28) and (B.18), we have

$$
\begin{aligned}
\frac{\partial \int \mathbf{J}^*(\mathbf{x}) \mathbf{E}(\mathbf{x}, \tilde{\omega} + i\Gamma) d\mathbf{x}}{\partial \varepsilon_k} &= \int \mathbf{J}^*(\mathbf{x}) \frac{\partial \mathbf{E}(\mathbf{x}, \tilde{\omega} + i\Gamma)}{\partial \varepsilon_k} d\mathbf{x} \\
&= \tilde{\omega}^2 \left(1 + \frac{i}{2\tilde{Q}} \right) \int (\tilde{\mathcal{M}}^{-1} \mathbf{J}(\mathbf{x}))^T \delta(\mathbf{x} - \mathbf{x}_k) \mathbf{E}(\mathbf{x}, \tilde{\omega} + i\Gamma) d\mathbf{x} \\
&= -i\tilde{\omega} \left(1 + \frac{i}{2\tilde{Q}} \right) \int \mathbf{E}^T(\mathbf{x}, \tilde{\omega} + i\Gamma) \delta(\mathbf{x} - \mathbf{x}_k) \mathbf{E}(\mathbf{x}, \tilde{\omega} + i\Gamma) d\mathbf{x} \\
&= -i\tilde{\omega} \left(1 + \frac{i}{2\tilde{Q}} \right) \mathbf{E}^T(\mathbf{x}_k, \tilde{\omega} + i\Gamma) \mathbf{E}(\mathbf{x}_k, \tilde{\omega} + i\Gamma),
\end{aligned}
$$

(B.19)

and

$$
\begin{aligned}
\frac{\partial \int \varepsilon(\mathbf{x}) \mathbf{E}^T \mathbf{E} d\mathbf{x}}{\partial \varepsilon_k} &= 2 \int \varepsilon(\mathbf{x}) \mathbf{E}^T \frac{\partial \mathbf{E}(\mathbf{x}, \tilde{\omega} + i\Gamma)}{\partial \varepsilon_k} d\mathbf{x} + \int \delta(\mathbf{x} - \mathbf{x}_k) \mathbf{E}^T(\mathbf{x}, \tilde{\omega} + i\Gamma) \mathbf{E}(\mathbf{x}, \tilde{\omega} + i\Gamma) d\mathbf{x} \\
&= 2 \int \varepsilon(\mathbf{x}) \mathbf{E}^T \tilde{\mathcal{M}}^{-1} \left[\tilde{\omega}^2 \left(1 + \frac{i}{2\tilde{Q}} \right) \delta(\mathbf{x} - \mathbf{x}_k) \mathbf{E}(\mathbf{x}, \tilde{\omega} + i\Gamma) \right] \\
&\qquad\qquad\qquad\qquad\qquad + \mathbf{E}^T(\mathbf{x}_k, \tilde{\omega} + i\Gamma) \mathbf{E}(\mathbf{x}_k, \tilde{\omega} + i\Gamma) \\
&= 2\tilde{\omega}^2 \left(1 + \frac{i}{2\tilde{Q}} \right) \int \left(\tilde{\mathcal{M}}^{-1} [\varepsilon(\mathbf{x}) \mathbf{E}(\mathbf{x}, \tilde{\omega} + i\Gamma)] \right)^T \delta(\mathbf{x} - \mathbf{x}_k) \mathbf{E}(\mathbf{x}, \tilde{\omega} + i\Gamma) d\mathbf{x} \\
&\qquad\qquad\qquad\qquad\qquad + \mathbf{E}^T(\mathbf{x}_k, \tilde{\omega} + i\Gamma) \mathbf{E}(\mathbf{x}_k, \tilde{\omega} + i\Gamma).
\end{aligned}
$$

(B.20)

Combining (B.17), (B.19) and (B.20), we have

$$
\begin{aligned}
\frac{\partial \ell}{\partial \varepsilon_k} = \left(i + \frac{1}{\tilde{Q}} \right) \frac{6}{\pi} \tilde{\omega} \mathbf{E}^T(\mathbf{x}_k, \tilde{\omega} + i\Gamma) \mathbf{E}(\mathbf{x}_k, \tilde{\omega} + i\Gamma) \\
+ \frac{12}{\pi} \frac{\tilde{\omega}^3}{\tilde{Q}} \left(1 + \frac{i}{2\tilde{Q}} \right) \mathbf{A}^T(\mathbf{x}_k, \tilde{\omega} + i\Gamma) \mathbf{E}(\mathbf{x}_k, \tilde{\omega} + i\Gamma),
\end{aligned}
$$
(B.21)

where $\mathbf{A}(\mathbf{x}, \tilde{\omega} + i\Gamma)$ satisfies the scattering equation

$$\tilde{\mathcal{M}}(\varepsilon, \tilde{\omega})\mathbf{A}(\mathbf{x}, \tilde{\omega} + i\Gamma) = \varepsilon(\mathbf{x})\mathbf{E}(\mathbf{x}, \tilde{\omega} + i\Gamma). \tag{B.22}$$

B.5   Hessian of the LDOS

In this section, we show that when near resonance [ω is close to $\Re(\omega_n)$], the Hessian of the LDOS with respect to $\varepsilon(\mathbf{x})$ is of order Q^3, namely $\frac{\partial^2 \text{LDOS}}{\partial \varepsilon_{k_1} \partial \varepsilon_{k_2}} = O(Q^3)$. We are not aware of any previous work that remarks on this fact.

Before we proceed, let us establish the relationship between the small changes in the system's dielectric constant $\varepsilon(\mathbf{x})$ and the corresponding changes in the eigenvalue ω_n (up to first order). From first order perturbation theory or variational theorem [54], it is easy to show that

$$\frac{\Delta\omega_n^2}{\omega_n^2} = -\frac{\int \Delta\varepsilon(\mathbf{x})|\mathbf{E}^n(\mathbf{x})|^2 d\mathbf{x}}{\int \varepsilon(\mathbf{x})|\mathbf{E}^n(\mathbf{x})|^2 d\mathbf{x}}. \tag{B.23}$$

Therefore, the sensitivity of eigenvalue ω_n to the dielectric constant at $\mathbf{x} = \mathbf{x}_k$ is

$$\frac{\partial \omega_n}{\partial \varepsilon_k} = -\frac{\omega_n}{2}|\mathbf{E}^n(\mathbf{x}_k)|^2 \tag{B.24}$$

From (B.8), we know that when near resonance, the LDOS can be approximated by

$$\text{LDOS}(\omega, \mathbf{x}') \approx -\frac{3}{\pi}|\mathbf{E}^n(\mathbf{x}') \cdot \hat{\mathbf{e}}_j|^2 \text{Im}[\frac{1}{\omega - \omega_n}]. \tag{B.25}$$

131

Therefore, the Hessian of the LDOS can be approximated by

$$
\begin{aligned}
\frac{\partial^2 \mathrm{LDOS}}{\partial \varepsilon_{k_1} \partial \varepsilon_{k_2}} &\approx -\frac{3}{\pi} |\mathbf{E}^n(\mathbf{x}') \cdot \hat{\mathbf{e}}_j|^2 \,\mathrm{Im} \left[\frac{2 \frac{\partial \omega_n}{\partial \varepsilon_{k_1}} \frac{\partial \omega_n}{\partial \varepsilon_{k_2}} - (\omega - \omega_n) \frac{\partial^2 \omega_n}{\partial \varepsilon_{k_1} \partial \varepsilon_{k_2}}}{(\omega - \omega_n)^3} \right] \\
&\approx -\frac{3}{\pi} |\mathbf{E}^n(\mathbf{x}') \cdot \hat{\mathbf{e}}_j|^2 \,\mathrm{Im} \left[\frac{2 \frac{\partial \omega_n}{\partial \varepsilon_{k_1}} \frac{\partial \omega_n}{\partial \varepsilon_{k_2}}}{(\omega - \omega_n)^3} \right] \\
&\approx -\frac{3}{\pi} |\mathbf{E}^n(\mathbf{x}') \cdot \hat{\mathbf{e}}_j|^2 \frac{\frac{\omega^2}{2} |\mathbf{E}^n(\mathbf{x}_{k_1})|^2 |\mathbf{E}^n(\mathbf{x}_{k_2})|^2}{(\mathrm{Im}[\omega_n])^3} \\
&\approx -\frac{12 Q^3}{\pi \omega V^3 \varepsilon(\mathbf{x}')^3} \frac{|\mathbf{E}^n(\mathbf{x}_{k_1})|^2 |\mathbf{E}^n(\mathbf{x}_{k_2})|^2}{|\mathbf{E}^n(\mathbf{x}') \cdot \hat{\mathbf{e}}_j|^4} \\
&= O\!\left(\left(\frac{Q}{V}\right)^3\right).
\end{aligned}
\tag{B.26}
$$

Bibliography

[1] A.F. Abouraddy, M. Bayindir, G. Benoit, S.D. Hart, K. Kuriki, N. Orf, O. Shapira, F. Sorin, B. Temelkuran, and Y. Fink. Towards multimaterial multifunctional fibres that see, hear, sense and communicate. *Nature Materials*, 6(5):336 347, 2007.

[2] M. Abramowitz and I. A. Stegun. *Handbook of Mathematical Functions With Formulas, Graphs and Mathematical Tables*. Dover, 1992.

[3] Lars V. Ahlfors. *Complex analysis*. McGraw-Hill Book Co., New York, third edition, 1978.

[4] Yoshihiro Akahane, Takashi Asano, Bong-Shik Song, and Susumu Noda. High-Q photonic nanocavity in a two-dimensional photonic crystal. *Nature*, 425(6961):944–947, October 2003.

[5] Yoshihiro Akahane, Takashi Asano, Bong-Shik Song, and Susumu Noda. Fine-tuned high-Q photonic-crystal nanocavity. *Optics Express*, 13(4):1202–1214, February 2005.

[6] E. Anderson, Z. Bai, C. Bischof, J. Demmel, J. Dongarra, J. D. Croz, A. Greenbaum, S. Hammarling, A. McKenney, S. Ostrouchov, and D. Sorensen. *LAPACK's User's Guide*. SIAM, third edition, 1999.

[7] A. L. Andrew, K. E. Chu, and P. Lancaster. On the numerical solution of nonlinear eigenvalue problems. *Computing*, 55(2):91–111, 1995.

[8] Satish Balay, Jed Brown, Kris Buschelman, Victor Eijkhout, William D. Gropp, Dinesh Kaushik, Matthew G. Knepley, Lois C. McInnes, Barry F. Smith, and Hong Zhang. PETSc users manual. Technical Report ANL-95/11 - Revision 3.3, Argonne National Laboratory, 2012.

[9] Satish Balay, Jed Brown, Kris Buschelman, William D. Gropp, Dinesh Kaushik, Matthew G. Knepley, Lois C. McInnes, Barry F. Smith, and Hong Zhang. PETSc Web page, 2012.

[10] Satish Balay, William D. Gropp, Lois C. McInnes, and Barry F. Smith. Efficient Management of Parallelism in Object Oriented Numerical Software Libraries. In E. Arge, A. M. Bruaset, and H. P. Langtangen, editors, *Modern Software Tools in Scientific Computing*. Birkhäuser Press, 1997.

[11] R. Barrett, M. Berry, T. F. Chan, J. Demmel, J. Donato, J. Dongarra, V. Ei-jkhout, R. Pozo, C. Romine, and H. Van der Vorst. *Templates for the Solution of Linear Systems: Building Blocks for Iterative Methods*. SIAM, Philadelphia, PA, 2nd edition, 1994.

[12] G. K. Batchelor. *An Introduction to Fluid Dynamics*. Cambridge University Press, 1973.

[13] M. P. Bendsoe and O. Sigmund. *Topology Optimization: Theory, Methods and Applications*. Springer, second edition, 2003.

[14] Daniel Bonn, Jens Eggers, Joseph Indekeu, Jacques Meunier, and Etienne Rolley. Wetting and spreading. *Reviews of Modern Physics*, 81(2):739-805, May 2009.

[15] Peter Buchak, 2010. Private Communication.

[16] H. B. G. Casimir and D. Polder. The Influence of Retardation on the London-van der Waals Forces. *Physical Review Online Archive (Prola)*, 73(4):360-372, February 1948.

[17] S. Chandrasekhar. *Hydrodynamic and Hydromagnetic Stability*. Oxford University Press, 1961.

[18] Y. C. Chang, T. Y. Hou, B. Merriman, and S. Osher. A level set formulation of eulerian interface capturing methods for incompressible fluid flows. *Journal of Computational Physics*, 124(2):449-464, 1996.

[19] A. Chauhan, C. Maldarelli, D. T. Papageorgiou, and D. S. Rumschitzki. Temporal instability of compound threads and jets. *J. Fluid Mech.*, 420(1):1-25, 2000.

[20] Weng C. Chew. *Waves and Fields in Inhomogeneous Media*. IEEE Press, 1995.

[21] R. Coccioli, M. Boroditsky, K. W. Kim, Y. Rahmat-Samii, and E. Yablonovitch. Smallest possible electromagnetic mode volume in a dielectric cavity. *IEE Proceedings - Optoelectronics*, 145(6):391+, 1998.

[22] Itai Cohen, Michael P. Brenner, Jens Eggers, and Sidney R. Nagel. Two fluid drop snap-off problem: Experiments and theory. *Phys. Rev. Lett.*, 83(6):1147-1150, Aug 1999.

[23] Darren Crowdy. On a class of geometry-driven free boundary problems. *SIAM Journal on Applied Mathematics*, 62:945-964, 2002.

[24] Darren G. Crowdy. Compressible bubbles in Stokes flow. *J. Fluid Mech.*, 476:345-356, 2003.

[25] Giuseppe D'Aguanno, Nadia Mattiucci, Marco Centini, Michael Scalora, and Mark J. Bloemer. Electromagnetic density of modes for a finite-size three-dimensional structure. *Physical Review E*, 69(5):057601+, May 2004.

[26] P. G. de Gennes. Wetting: statics and dynamics. *Reviews of Modern Physics*, 57(3):827–863, July 1985.

[27] J. W. Demmel and Bo Kagstrom. Computing stable eigendecompositions of matrix pencils. *Linear Algebra and its Applications*, 88-89:139–186, 1987.

[28] D. S. Deng, J. C. Nave, X. Liang, S. G. Johnson, and Y. Fink. Exploration of in-fiber nanostructures from capillary instability. *Optics Express*, 19(17):16273+, August 2011.

[29] D. S. Deng, N. D. Orf, A. F. Abouraddy, A. M. Stolyarov, J. D. Joannopoulos, H. A. Stone, and Y. Fink. In-fiber semiconductor filament arrays. *Nano Lett.*, 8(12):4265–4269, 2008.

[30] D. S. Deng, N. D. Orf, S. Danto, A. F. Abouraddy, J. D. Joannopoulo, and Y. Fink. Processing and properties of centimeter-long, in-fiber, crystalline-selenium filaments. *Appl. Phys. Lett.*, 96:023102, 2010.

[31] B. V. Derjaguin, I. I. Abrikosova, and E. M. Lifshitz. Direct measurement of molecular attraction between solids separated by a narrow gap. *Q. Rev. Chem. Soc.*, 10:295–329, 1956.

[32] David C. Dobson and Fadil Santosa. Optimal Localization of Eigenfunctions in an Inhomogeneous Medium. *SIAM Journal on Applied Mathematics*, 64(3):762–774, January 2004.

[33] P. G. Drazin and W. H. Reid. *Hydrodynamic Stability*. Cambridge University Press, second edition, 2004.

[34] E. B. Dussan. On the Spreading of Liquids on Solid Surfaces: Static and Dynamic Contact Lines. *Annual Review of Fluid Mechanics*, 11(1):371–400, 1979.

[35] I. E. Dzyaloshinskii, E. M. Lifshitz, and Lev P. Pitaevskii. General theory of van der waals' forces. *Soviet Physics Uspekhi*, 4(2):153–176, February 1961.

[36] J. Eggers. Nonlinear dynamics and breakup of free-surface flows. *Rev. Mod. Phys.*, 69(3):865–930, 1997.

[37] J. Eggers and E. Villermaux. Physics of liquid jets. *Reports on Progress in Physics*, 71:036601, 2008.

[38] Jens Eggers. Universal pinching of 3d axisymmetric free-surface flow. *Phys. Rev. Lett.*, 71(21):34583460, Nov. 1993.

[39] Jens Eggers. A brief history of drop formation. In Pierre Alart, Olivier Maison-neuve, and R. Tyrrell Rockafellar, editors, *Nonsmooth Mechanics and Analysis*, volume 12 of *Advances in Mechanics and Mathematics*, chapter 14, pages 163–172. Springer, 2006.

[40] S. Egusa, Z. Wang, N. Chocat, Z. M. Ruff, A. M. Stolyarov, D. Shemuly, F. Sorin, P. T. Rakich, J. D. Joannopoulos, and Y. Fink. Multimaterial piezo-electric fibres. *Nature Materials*, 9:643 648, 2010.

[41] Walter R. Frei, H. T. Johnson, and Kent D. Choquette. Optimization of a single defect photonic crystal laser cavity. *Journal of Applied Physics*, 103(3):033102+, 2008.

[42] Jean-Michel Gerard and Bruno Gayral. Strong Purcell Effect for InAs Quantum Boxes in Three-Dimensional Solid-State Microcavities. *J. Lightwave Technol.*, 17(11):2089+, November 1999.

[43] P Guillaume. Nonlinear eigenproblems. *SIAM J. Matrix Anal. Appl.*, 20:575–595, 1999.

[44] A. Y. Gunawan, J. Molenaar, and A. A. F. van de Ven. In-phase and out-of-phase break-up of two immersed liquid threads under influence of surface tension. *Eur. J. Mech. B Fluids*, 21(4):399–412, 2002.

[45] A. Y. Gunawan, J. Molenaar, and A. A. F. van de Ven. Break-up of a set of liquid threads under influence of surface tension. *J. Engineering Math.*, 50(1):25–49, 2004.

[46] S. D. Hart, G. R. Maskaly, B. Temelkuran, P. H. Prideaux, J. D. Joannopoulos, and Y. Fink. External reflection from omnidirectional dielectric mirror fibers. *Science*, 296:511–513, 2002.

[47] Hila Hashemi, Cheng W. Qiu, Alexander P. McCauley, J. D. Joannopoulos, and Steven G. Johnson. Diameter-bandwidth product limitation of isolated-object cloaking. *Physical Review A*, 86:013804+, July 2012.

[48] P. Hénon, P. Ramet, and J. Roman. PaStiX: a high-performance parallel di-rect solver for sparse symmetric positive definite systems. *Parallel Computing*, 28(2):301–321, February 2002.

[49] Robert W. Hopper. Plane Stokes flow driven by capillarity on a free surface. II. Further developments. *J. Fluid Mech.*, 230:355–364, 1991.

[50] K. Inoue and K. Ohtaka. *Photonic Crystals: Physics, Fabrication and Applica-tions*. Springer Series in Optical Sciences. Springer, 2010.

[51] Jacob N. Israelachvili. *Intermolecular and Surface Forces*. Academic Press, London, second edition, January 1991.

[52] John D. Jackson. *Classical Electrodynamics*. John Wiley & Sons Inc, second edition, October 1975.

[53] J. S. Jensen and O. Sigmund. Topology optimization for nano-photonics. *Laser & Photonics Reviews*, 5(2):308–321, March 2011.

[54] John D. Joannopoulos, Steven G. Johnson, Joshua N. Winn, and Robert D. Meade. *Photonic Crystals: Molding the Flow of Light*. Princeton University Press, 2 edition, February 2008.

[55] Steven G. Johnson. The NLopt nonlinear-optimization package, http://ab-initio.mit.edu/nlopt.

[56] Steven G. Johnson. Numerical methods for computing Casimir interactions. In Diego Dalvit, Peter Milonni, David Roberts, and Felipe da Rosa, editors, *Casimir Physics*, volume 834 of *Lecture Notes in Physics*, chapter 6. Springer, Berlin, June 2011.

[57] Chiu-Yen Kao and Fadil Santosa. Maximization of the quality factor of an optical resonator. *Wave Motion*, 45(4):412–427, March 2008.

[58] Joshua J. Kaufman, Guangming Tao, Soroush Shabahang, Esmaeil-Hooman Banaei, Daosheng S. Deng, Xiangdong Liang, Steven G. Johnson, Yoel Fink, and Ayman F. Abouraddy. Structured spheres generated by an in-fibre fluid instability. *Nature*, 487(7408):463–467, July 2012.

[59] Shota Kita, Kengo Nozaki, Shoji Hachuda, Hideki Watanabe, Yuji Saito, Shota Otsuka, Takeharu Nakada, Yoshiki Arita, and Toshihiko Baba. Photonic Crystal Point-Shift Nanolasers With and Without Nanoslots Design, Fabrication, Lasing, and Sensing Characteristics. *IEEE Journal of Selected Topics in Quantum Electronics*, 17(6):1632–1647, November 2011.

[60] A. F. Koenderink. On the use of Purcell factors for plasmon antennas. *Optics Letters*, 35(24):4208–4210, December 2010.

[61] H. K. Kuiken. Viscous sintering: the surface-tension-driven flow of a liquid form under the influence of curvature gradients at its surface. *J. Fluid Mech.*, 214:503–515, 1990.

[62] P. K. Kundu and I. M. Cohen. *Fluid Mechanics*. Academic Press, 2007.

[63] K. Kuriki, O. Shapira, S. D. Hart, B. Benoit, Y. Kuriki, J. F. Viens, M. Bayindir, J. D. Joannopoulos, and Y. Fink. Hollow multilayer photonic bandgap fibers for NIR applications. *Optics Express*, 12:1510–1517, 2004.

[64] L. D. Landau, L. P. Pitaevskii, and E. M. Lifshitz. *Electrodynamics of Continuous Media*. Butterworth-Heinemann, 2 edition, January 1984.

137

[65] Ying Li, Jiangjun Zheng, Jie Gao, Jing Shu, Mehmet S. Aras, and Chee W. Wong. Design of dispersive optomechanical coupling and cooling in ultrahigh-Q/V slot-type photonic crystal cavities. *Optics Express*, 18(23):23844+, October 2010.

[66] X. Liang, D. S. Deng, J. C. Nave, and Steven G. Johnson. Linear stability analysis of capillary instabilities for concentric cylindrical shells. *Journal of Fluid Mechanics*, 683:235–262, 2011.

[67] B. S. Liao, Z. J. Bai, L. Q. Lee, and K Ko. Nonlinear Rayleigh-Ritz iterative method for solving large scale nonlinear eigenvalue problems. *Taiwanese J. Math.*, 14(3A):869–883, 2010.

[68] S. P. Lin. *Breakup of Liquid Sheets and Jets*. Cambridge University Press, 2003.

[69] Shiyun Lin, Ethan Schonbrun, and Kenneth Crozier. Optical Manipulation with Planar Silicon Microring Resonators. *Nano Lett.*, 10(7):2408–2411, June 2010.

[70] John R. Lister and Howard A. Stone. Capillary breakup of a viscous thread surrounded by another viscous fluid. *Phys. Fluids*, 10(11):2758–2764, 1998.

[71] DongC Liu and Jorge Nocedal. On the limited memory BFGS method for large scale optimization. *Mathematical Programming*, 45(1-3):503–528, August 1989.

[72] X-D. Liu, S Osher, and T. Chan. Weighted essentially non-oscillatory schemes. *J. Comput. Phys.*, 115(1):200–212, 1994.

[73] J. Lourtioz, H. Benisty, V. Berger, J. Gerard, D. Maystre, and A. Tchelnokov. *Photonic Crystals: Towards Nanoscale Photonic Devices*. Springer, 2005.

[74] Jesse Lu, Stephen Boyd, and Jelena Vuckovic. Inverse design of a three-dimensional nanophotonic resonator. *Opt. Express*, 19(11):10563–10570, May 2011.

[75] Jesse Lu and Jelena Vuckovic. Inverse design of nanophotonic structures using complementary convex optimization. *Optics Express*, 18(4):3793+, February 2010.

[76] J. Lucassen, M. van den Tempel, A. Vrij, and F. Th Hesselink. Waves in thin liquid films I: The different modes of vibration. *Proc. K. Ned. Akad. Wet.*, B73:109–123, 1970.

[77] Charles Maldarelli, Rakesh K. Jain, Ivan B. Ivanov, and Eli Ruckenstein. Stability of symmetric and unsymmetric thin liquid films to short and long wavelength perturbations. *Journal of Colloid and Interface Science*, 78(1):118–143, November 1980.

[78] E. A. J. Marcatili. Bends in Optical Dielectric Guides. *Bell Syst. Tech. J.*, 48:2103–2132, 1969.

[79] Olivier J. F. Martin and Nicolas B. Piller. Electromagnetic scattering in polarizable backgrounds. *Physical Review E*, 58:3909–3915, September 1998.

[80] Murray W. McCutcheon and Marko Loncar. Design of a silicon nitride photonic crystal nanocavity with a Quality factor of one million for coupling to a diamond nanocrystal. *Optics Express*, 16(23):19136+, November 2008.

[81] Ahmad R. Md Zain, Nigel P. Johnson, Marc Sorel, and Richard M. De La Rue. Ultra high quality factor one dimensional photonic crystal/photonic wire microcavities in silicon-on-insulator (SOI). *Optics Express*, 16(16):12084–12089, July 2008.

[82] Zi M. Meng, Fei Qin, Ye Liu, and Zhi Y. Li. High-Q microcavities in low-index one-dimensional photonic crystal slabs based on modal gap confinement. *Journal of Applied Physics*, 109(4):043107+, 2011.

[83] Owen D. Miller, Chia W. Hsu, M. T. Homer Reid, Wenjun Qiu, Brendan G. DeLacy, John D. Joannopoulos, Marin Soljacic, and Steven G. Johnson. Computational Design of Non-Spherical Super-Scattering Particles at Visible Wavelengths, 2013.

[84] Kimball A. Milton, Jef Wagner, Prachi Parashar, and Iver Brevik. Casimir energy, dispersion, and the Lifshitz formula. *Physical Review D*, 81:065007+, March 2010.

[85] N. A. P. Nicorovici, R. C. McPhedran, and L. C. Botten. Relative local density of states for homogeneous lossy materials. *Physica B: Condensed Matter*, 405(14):2915–2919, July 2010.

[86] Jorge Nocedal and Stephen J. Wright. *Numerical Optimization*. Springer, August 2000.

[87] S. Noda and T. Baba. *Roadmap on photonic crystals*, volume 1. Springer, 2003.

[88] Masahiro Nomura. GaAs-based air-slot photonic crystal nanocavity for optomechanical oscillators. *Optics Express*, 20(5):5204+, February 2012.

[89] Masahiro Nomura, Katsuaki Tanabe, Satoshi Iwamoto, and Yasuhiko Arakawa. High-Q design of semiconductor-based ultrasmall photonic crystal nanocavity. *Optics Express*, 18(8):8144+, April 2010.

[90] Lukas Novotny and Bert Hecht. *Principles of Nano-Optics*. Cambridge University Press, June 2006.

[91] H. Ockendon and J. R. Ockendon. *Viscous Flow*. Cambridge University Press, 1995.

[92] Alexander Oron, Stephen H. Davis, and S. George Bankoff. Long-scale evolution of thin liquid films. *Reviews of Modern Physics*, 69(3):931–980, July 1997.

[93] S. Osher and R. Fedkiw. *Level Set Methods and Dynamic Implicit Surfaces.* Springer, 2002.

[94] Ardavan F. Oskooi. *Computation & design for nanophotonics.* PhD thesis, Massachusetts Institute of Technology, 2010.

[95] B. Osting and M. I. Weinstein. Long-lived scattering resonances and Bragg structures. *submitted*, 2011.

[96] Michael E. Peskin and Dan V. Schroeder. *An Introduction To Quantum Field Theory (Frontiers in Physics).* Westview Press, October 1995.

[97] J. A. F. Plateau. *Statique Experimentale et Theorique des Liquides Soumis aux Seules Forces Moleculaires*, volume 2. Paris: Gauthier Villars, 1873.

[98] E. Pone, C. Dubois, N. Gu, Y. Gao, A. Dupuis, F. Boismenu, S. Lacroix, and M. Skorobogatiy. Drawing of the hollow all-polymer Bragg fibers. *Optics Express*, 14(13):5838–5852, 2006.

[99] E. M. Purcell. Spontaneous Emission Probabilities at Radio Frequencies. *Physics Review*, 69(11-12):674, June 1946.

[100] Dominik G. Rabus. *Integrated Ring Resonators*, volume 127 of *Springer Series in Optical Sciences*. Springer, Berlin, Heidelberg, 2007.

[101] Lord Rayleigh. On the capillary phenomena of jets. *Proceedings of the Royal Society of London*, 29:71–97, 1879.

[102] Lord Rayleigh. On the instability of a cylinder of viscous liquid under capillary force. *Phil. Mag.*, 34(207):145–154, Aug 1892.

[103] Jacob T. Robinson, Christina Manolatou, Long Chen, and Michal Lipson. Ultrasmall Mode Volumes in Dielectric Optical Microcavities. *Physical Review Letters*, 95(14):143901+, September 2005.

[104] Eli Ruckenstein and Rakesh K. Jain. Spontaneous rupture of thin liquid films. *J. Chem. Soc., Faraday Trans. 2*, 70(0):132–147, 1974.

[105] A Ruhe. Rational Krylov for large nonlinear eigenproblems. In *Applied Parallel Computing*, number 3732 in Lecture Notes in Computer Science, pages 357–363. Springer, 2006.

[106] D. F. Rutland and G. J. Jameson. A non-linear effect in the capillary instability of liquid jets. *Journal of Fluid Mechanics*, 46:267–271, February 1971.

[107] R. K. Shah, H. C. Shum, A. C. Rowat, D. Lee, J. J. Agresti, A. S. Utada, L.-Y. Chu, J.-W. Kim, A. Fernandez-Nieves, C. J. Martinez, and D. A. Weitz. Designer emulsions using microfluidics. *Materials Today*, 11(4):18–27, 2008.

[108] C. W. Shu and S. Osher. Efficient implementation of essentially non-oscillatory shock-capturing schemes, ii. *Journal of Computational Physics*, 83:32–78, 1989.

[109] Kurt Smith, Francisco Solis, and David Chopp. A projection method for motion of triple junctions by level sets. *Interfaces and Free Boundaries*, pages 263–276, 2002.

[110] F. Sorin, A.F. Abouraddy, N. Orf, O. Shapira, J. Viens, J. Arnold, J.D. Joannopoulos, and Y. Fink. Multimaterial photodetecting fibers: a geometric and structural study. *Advanced Materials*, 19:3872–3877, 2007.

[111] Arthur M. Sterling and C. A. Sleicher. The instability of capillary jets. *J. Fluid Mech.*, 68:477–495, 1975.

[112] H. A. Stone and M. P. Brenner. Note on the capillary thread instability for fluids of equal viscosities. *J. Fluid Mech.*, 318:373–374, 1996.

[113] G. Strang. *Computational Science and Engineering*. Wellesley-Cambridge Press, 2007.

[114] M. Sussman, P. Smereka, and S. Osher. A level set approach for computing solutions to incompressible two-phase flow. *Journal of Computational Physics*, 114:146–159, 1994.

[115] Krister Svanberg. A Class of Globally Convergent Optimization Methods Based on Conservative Convex Separable Approximations. *SIAM Journal on Optimization*, 12(2):555–573, January 2002.

[116] Saleh Tanveer and Giovani L. Vasconcelos. Time-evolving bubbles in two-dimensional Stokes flow. *J. Fluid Mech.*, 301:325–344, 1995.

[117] S. Tomotika. On the instability of a cylindrical thread of a viscous liquid surrounded by another viscous fluid. *Proceedings of the Royal Society of London. Series A, Mathematical and Physical Sciences*, 150(870):322–337, Jun. 1935.

[118] L. N. Trefethen and D. Bau. *Numerical Linear Algebra*. SIAM, 1997.

[119] A. S. Utada, E. Lorenceau, D. R. Link, P. D. Kaplan, H. A. Stone, and D. A. Weitz. Monodisperse double emulsions generated from a microcapillary device. *Science*, 308(5721):537–541, 2005.

[120] Milton Van Dyke. *An Album of Fluid Motion*. Parabolic Press, Inc., 12th edition, June 1982.

[121] H. Voss. A Jacobi-Davidson method for nonlinear and nonsymmetric eigenproblems. *Comput. & Structures*, 85(17-18):1284–1292, 2007.

[122] A. Vrij. Possible mechanism for the spontaneous rupture of thin, free liquid films. *Discuss. Faraday Soc.*, 42(0):23–33, 1966.

[123] A. Vrij, Hesselink, J. Lucassen, and M. van den Tempel. Waves in thin liquid films II: Symmetrical modes in very thin films and film rupture. *Proc. K. Ned. Akad. Wet.*, B73:124–135, 1970.

[124] A. Vrij and Overbeek. Rupture of thin liquid films due to spontaneous fluctuations in thickness. *J. Am. Chem. Soc.*, 90(12):3074–3078, June 1968.

[125] J. Vuckovic, M. Loncar, H. Mabuchi, and A. Scherer. Optimization of the Q factor in photonic crystal microcavities. *IEEE Journal of Quantum Electronics*, 38(7):850–856, July 2002.

[126] Jelena Vučković, Marko Lončar, Hideo Mabuchi, and Axel Scherer. Design of photonic crystal microcavities for cavity QED. *Physical Review E*, 65:016608+, December 2001.

[127] M. R. Watts, S. G. Johnson, H. A. Haus, and J. D. Joannopoulos. Electromagnetic cavity with arbitrary Q and small modal volume without a complete photonic bandgap. *Optics Letters*, 27(20):1785+, October 2002.

[128] Chee W. Wong, Peter T. Rakich, Steven G. Johnson, Minghao Qi, Henry I. Smith, Erich P. Ippen, Lionel C. Kimerling, Yongbae Jeon, George Barbastathis, and Sang G. Kim. Strain-tunable silicon photonic band gap microcavities in optical waveguides. *Applied Physics Letters*, 84(8):1242–1244, 2004.

[129] Yong Xu, Wei Liang, Amnon Yariv, J. G. Fleming, and Shawn-Yu Lin. High-quality-factor Bragg onion resonators with omnidirectional reflector cladding. *Optics Letters*, 28(22):2144+, November 2003.